https://lib.uliege.be https://matheo.uliege.be

Archaeological and paleoenvironmental interpretation through tomographic model classification and geophysical mapping;Ostia Antica (Rome, Italy) case study

Auteur : Devillers, Camille
Promoteur(s) : Nguyen, Frédéric
Faculté : Faculté des Sciences appliquées
Diplôme : Master en ingénieur civil des mines et géologue, à finalité spécialisée en géologie de l'ingénieur et de l'environnement
Année académique : 2024-2025
URI/URL : http://hdl.handle.net/2268.2/24642

Avertissement à l'attention des usagers :

Tous les documents placés en accès ouvert sur le site le site MatheO sont protégés par le droit d'auteur. Conformément aux principes énoncés par la "Budapest Open Access Initiative"(BOAI, 2002), l'utilisateur du site peut lire, télécharger, copier, transmettre, imprimer, chercher ou faire un lien vers le texte intégral de ces documents, les disséquer pour les indexer, s'en servir de données pour un logiciel, ou s'en servir à toute autre fin légale (ou prévue par la réglementation relative au droit d'auteur). Toute utilisation du document à des fins commerciales est strictement interdite.

Par ailleurs, l'utilisateur s'engage à respecter les droits moraux de l'auteur, principalement le droit à l'intégrité de l'oeuvre et le droit de paternité et ce dans toute utilisation que l'utilisateur entreprend. Ainsi, à titre d'exemple, lorsqu'il reproduira un document par extrait ou dans son intégralité, l'utilisateur citera de manière complète les sources telles que mentionnées ci-dessus. Toute utilisation non explicitement autorisée ci-avant (telle que par exemple, la modification du document ou son résumé) nécessite l'autorisation préalable et expresse des auteurs ou de leurs ayants droit.

Archaeological and paleoenvironmental interpretation through tomographic model classification and geophysical mapping; Ostia Antica (Rome, Italy) case study

---

Author: DEVILLERS Camille

Master thesis presented to obtain the degree of: Master of Science in Geological and Mining Engineering professional specialising in environmental and geological engineering

Academic Supervisor: NGUYEN Frédéric

Academic Year: **2024 – 2025**

ACKNOWLEDGEMENT

I am deeply grateful to the many people whose participation and support made the completion of this master thesis possible.

First and foremost, I would like to express my sincere gratitude to my master thesis supervisor, Prof. Frédéric Nguyen, for his time, guidance and excellent supervision throughout this year. My heartfelt thanks also go to the entire geophysics team and especially to Tom Debouny and David Caterina, for their invaluable help and support during the fieldwork campaigns and in the subsequent data processing. I am particularly thankful to Tom for his constructive comments and corrections during the writing of this report.

I am equally grateful to Prof. Ferréol Salomon, Joé Juncker and Matthias Delmetz for warmly welcoming me into the Department of Geography at the University of Strasbourg and for their assistance in interpreting my data. My thanks also go to Grégory Mainet for his involvement in the field campaign. I am truly glad to have been able to integrate my Master's work into a broader, collaborative study.

Although not directly part of my thesis, I would also like to thank Guillaume Blanchy, my internship supervisor, for his warm welcome and for the valuable technical skills I gained during my six-week placement.

On a more personal note, I am grateful to my friendly Geological Engineering Master's classmates for these two years filled with laughter, learning and friendship. Finally, I wish to express my deepest thanks to my family and Hugo for their daily support and for always enabling me to pursue what matters most to me.

ABSTRACT

The Ostia Antica site, the ancient port of Rome remarkably well preserved, constitutes a privileged study area to trace the geomorphological and environmental evolution of the region. It also offers an ideal framework to test and develop non-destructive investigation methods, in an interdisciplinary approach combining archaeology, geophysics, hydrogeology and geotechnics. Numerous geophysical campaigns have already been conducted there by different research groups to better understand the area.

This master thesis is therefore part of the continuation of these investigations and aims to contribute to the interpretation of the geoarchaeology and paleoenvironment of the Ostia Antica region. To this end, two geophysical methods were implemented in the field: electrical resistivity tomography (ERT) and seismics. In addition, part of the magnetic induction survey carried out by Ghent University was also processed.

The interpretation of the geophysical data was divided into two parts. Indeed, some profiles, carried out near the Tiber, were processed and interpreted separately from the rest of the profiles. The analysis of the second group of profiles raised several challenges, notably the presence of deep anomalies in some of them, for which it was necessary to determine whether they were related to the inversion process or not. Indeed, a certain ambiguity persists in the inversion, as multiple models can equivalently reproduce the observed data. To address this issue, constrained inversions, based on geostatistical or geotechnical data, were performed in addition to classical isotropic inversions. Finally, part of the inverted profiles was analysed using a probabilistic approach applying Bayes' rule to classify the inversion results to assign a lithology or a type of deposits to each area. This study relies on data collected by other researchers, which are used to establish the a priori information for the classification.

The overall data processing allowed the delimitation of the archaeosphere, characterised by higher resistivities, as well as the interface between freshwater-saturated deposits (more resistive) and saltwater-saturated deposits (more conductive). The different inversions suggest that the anomalies observed at depth are probably real, but their interpretation remains difficult to date.

It would therefore be relevant to carry out additional profiles with high vertical resolution to study these anomalies. Deep boreholes could also provide complementary information.

RESUME

Le site d'Ostia Antica, ancien port de la Rome antique remarquablement bien conservé, constitue un terrain d'étude privilégié pour retracer l'évolution géomorphologique et environnementale de la région. Il offre également un cadre idéal pour tester et développer des méthodes d'investigation non destructives, dans une approche interdisciplinaire mêlant archéologie, géophysique, hydrogéologie et géotechnique. De nombreuses campagnes géophysiques y ont déjà été menées par différents groupes de recherche afin de mieux comprendre la zone.

Ce travail de master s'inscrit donc dans la continuité de ces investigations et vise à contribuer à l'interprétation de la géoarchéologie et du paléoenvironnement de la région d'Ostia Antica. Pour cela, deux méthodes géophysiques ont été mises en œuvre sur le terrain : la tomographie de résistivité électrique (ERT) et la sismique. En plus, une partie de la campagne d'induction magnétique menée par l'université de Gand a également été traitée.

L'interprétation des données géophysiques a été scindée en deux parties. En effet, certains profils réalisés à proximité du Tibre ont été traités et interprétés séparément du reste des profils. L'analyse du second groupe de profils a soulevé plusieurs défis, notamment la présence d'anomalies en profondeur sur certains d'entre eux, dont il a fallu déterminer si elles étaient liées ou non au processus d'inversion. En effet, une certaine ambiguïté persiste dans l'inversion, car plusieurs modèles peuvent reproduire de manière équivalente les données observées. Pour répondre à cette problématique, des inversions contraintes, basées sur des données géostatistiques ou géotechniques, ont été effectuées en complément des inversions isotropes classiques. Enfin, une partie des profils inversés a été analysée grâce à une approche probabiliste utilisant la règle de Bayes pour classifier les résultats de l'inversion afin d'attribuer à chaque zone une lithologie ou un type de dépôts. Cette étude s'appuie sur des données recueillies par d'autres chercheurs, servant à établir les informations a priori pour la classification.

L'ensemble du traitement des données a permis de délimiter l'archéosphère, caractérisée par des résistivités plus élevées, ainsi que l'interface entre les dépôts saturées en eau douce (plus résistifs) et ceux saturés en eau salée (plus conducteurs). Les différentes inversions suggèrent que les anomalies observées en profondeur sont probablement réelles, mais leur interprétation reste difficile à ce jour.

Il serait donc pertinent de réaliser d'autres profils à haute résolution verticale afin d'étudier ces anomalies. Des forages profonds pourraient également fournir des informations complémentaires.

Table of Content

List of Figures

List of Tables

1. Introduction

1.1. Context

Archaeogeophysics is a branch of geophysics developed to adapt geophysical methods to archaeological studies. The most used techniques are electrical, magnetic and radar methods. This study focuses primarily on electrical resistivity tomography (ERT), although electromagnetic induction (EMI) and seismic methods are also discussed.

Ostia Antica, the ancient port of Roman antiquity located about thirty kilometres from Rome, is an archaeological site of exceptional richness. Thanks to its remarkable state of preservation and its strategic position along the Tyrrhenian Sea and near the important Tiber River, it offers a unique window into urban, economic and environmental life in Antiquity. This site not only fascinates historians and archaeologists but also serves as a privileged study area for geophysicists and geologists seeking to better understand the geomorphological and hydrogeological evolution of the region.

This work is part of a series of geophysical studies conducted in recent years, with the aim of providing new datasets that can be compared and combined with those already collected at the site. Since our geophysical campaign, additional campaigns have already been conducted.

In electrical resistivity tomography, field data must be inverted to enable interpretation. However, the inversion process is inherently ambiguous: the same set of field measurements can lead to different inversion models depending on the parameters selected. To reduce this ambiguity and increase the reliability of the results, the data acquired in this study will be integrated with two other independent datasets: core samples collected by the University of Strasbourg and Direct Push-Electrical Conductivity (DP-EC) analysed in the article written by Hadler et al., 2020.

The integration of these data is accomplished through joint inversions, including both geostatistical and constrained approaches. Additionally, a probabilistic method is employed to classify the inversion results, thereby supporting and guiding the interpretation. This method is based on the article written by Isunza Manrique et al., 2023. In this study, only the ERT data were incorporated into the classification. In future studies, it would also be valuable to integrate seismic and electromagnetic induction data to improve the understanding of the site and the reliability of the classification.

The objective is then to compare isotropic inversions of individual datasets with the joint and constrained inversions. Some profiles showed more resistive anomalies at depth that were difficult to interpret. According to the classification results, these anomalies are unlikely to have an anthropogenic origin. This study also made it possible to delineate the area containing anthropogenic deposits from the natural environment and to determine the location of the freshwater and marine aquifers.

1.2. Objective of master thesis

This work aims to improve the geophysical interpretation of the Ostia Antica site by integrating several investigative methods, notably, electrical resistivity tomography (ERT) will be discussed in more detail, while electromagnetic induction (EMI) and seismic techniques will also be addressed. Faced with the inherent ambiguity in the inversion processes of geophysical data, this project seeks to reduce uncertainty by combining classical inversions with constrained inversions that incorporate information from boreholes and direct-push electrical conductivity measurements. A probabilistic approach is also employed to classify the inversion results to guide lithological and archaeological interpretation.

1.3. Organisation of the document

This master thesis is divided into several parts. The first part (Chapters 2 and 3) constitutes the state of the art. Chapter 2 provides a review of geophysical methods used in archaeology, while Chapter 3 presents the archaeological, geological and hydrogeological context of Ostia Antica, along with a review of archaeogeophysical methods already applied in the site. The second part (Chapter 4) focuses on the various methods employed, as well as on the datasets collected by other researchers and used in this work. The third part (Chapters 5), which is the most substantial, presents the processing of the electrical resistivity tomography and the results obtained, integrating different inversion approaches such as isotropic inversions and constraint inversions. The probabilistic approach used to classify the inversion results is also explained in this Chapter. In Chapter 6 presents a complementary analysis of electromagnetic induction (EMI) and surface wave seismic. This chapter also presents perspectives on the integration of these methods into the classification. Finally, Chapter 7 is devoted to the conclusions and perspectives regarding the use of archaeogeophysics at Ostia.

2. A review of archaeogeophysics

Archaeogeophysics is a branch of geophysics that has developed over the last sixty years, adapting geophysical methods to archaeological challenges. Initially, the approach was predictive and aimed at identifying potential sites (Dabas, 2024). It can help to predict upcoming surveys and excavations.

The developments of archaeogeophysics have helped archaeologists in their field research. Archaeogeophysics differs from traditional geophysics in that it is most often applied at shallow depth. Moreover, it does not conform to the simplifying assumptions usually employed (*e.g.* objects significantly larger than their burial depth). Geophysical prospection in archaeology aims to detect and map buried features. However, traditional methods often require adaptation due to limited subsurface access and the sensitivity of archaeological sites. Shallow structures and modern infrastructure can hinder equipment deployment or affect measurements. Additionally, legal restrictions may apply in protected areas. Geophysical tools can also disturb fragile layers through pressure or vibration (Dabas, 2018).

In general, geophysics has some limitations, such as providing indirect results. Indeed, it measures physical properties of the subsurface but does not directly identify objects or materials. Environmental conditions and ambient noise can also affect the results for certain methods. There is a limitation in depth resolution. Regarding data inversion, it is important to know that the solution is not unique (non-uniqueness of the solution).

Often, geophysics must be combined with other methods such as coring, mechanical prospection through destructive drilling, aerial surveys, pedestrian surveys or even oral testimonies. Mechanical surveys are essential for dating and assessing the preservation of remains. These traditional methods can identify small subsurface structures at depth and can overcome the limitations associated with geophysical techniques in geologically complex terrains. It is important to note that surveys are not always feasible, geophysics can provide valuable information even if it is not always direct (Dabas, 2018).

What is also interesting is that the maps produced through geophysics can also be used by other professionals involved in land-use planning. Prospection also enables precise data collection across the entire surface with multiple possible detection depths. It also enables the identification of more sensitive areas such as zones of erosion or sediment accumulation. It also helps to determine the best locations for drilling and aids in estimating the associated costs. In the best cases, geophysics can provide detailed maps of structures before the excavation phase and guide excavations towards more strategic areas (Dabas, 2018).

However, the efficiency of geophysical methods must be evaluated carefully according to several criteria. The aim of the geophysical and environmental analysis is to examine the study area in depth within the framework of predetermined constraints. The efficiency of the application of geophysical methods depends on three main factors: cost, time and information, which is based on 3 components: the quantitative evaluation of the information, the evaluation of the reliability of the information and the evaluation of the usefulness of the information according to practical criteria, *i.e.* judging whether the data is really relevant and exploitable in relation to the objectives of the study (Eppelbaum et al., 2024).

Geophysical methods can also provide information that can be integrated with remote sensing methods, such as the analysis of data obtained from satellite images and LIDAR (Light Detection and Ranging). This integration enhances archaeological research by providing complementary datasets for accurate mapping, visualisation and interpretation of landscape features associated with archaeological sites (Dabas, 2018).

Remote sensing is recognised for its low cost and its efficiency for the initial identification of archaeological sites. It is also the form of analysis least constrained by various methodological limitations. The integration of geophysical methods and remote sensing using an informational and probabilistic theoretical framework strengthens the reliability of archaeological detection and makes it possible to achieve new archaeological discoveries, even in areas considered as already studied because there is an automatic study approach carried out thanks to data already collected, analysed and verified (Eppelbaum et al., 2024).

Thanks to geophysical and aerial prospection, it is now possible to cover the entire surface of the areas to be explored, regardless of their size (Dabas, 2018). The archaeogeophysics methods are non-destructive, therefore, these techniques can help conserve human and financial resources in archaeology by precisely identifying and delineating locations that necessitate excavation (Eppelbaum et al., 2024). They also have a very low environmental impact.

Aerial prospection remains the method of choice for studying areas of several thousand hectares. Depending on weather conditions, it can provide an initial assessment of settlement density across a territory. However, this technique is highly dependent on the type of crop present on the studied area.

Finally, airborne LIDAR has recently made it possible to discover many sites in environments where other methods are largely ineffective. This method can highlight a site based on its topography. This new method requires micro-relief at the surface to function. It is particularly useful for detecting sites under forest cover. In agricultural plains, levelling due to mechanisation makes the LIDAR method less useful except for detecting ancient field systems (Dabas, 2018).

The appearance of GPS and its more precise variants such as RTK (Real-Time Kinematic) data with centimetre accuracy have made it possible to automatically associate each measurement with a position. However, it should be noted that GPS reception is not satisfactory in undergrowth or in cities (Dabas, 2018).

There are several classes of methods. One of them is the **electric methods** based on the electrical properties of the subsurface. These methods rely on the resistivity of the ground to the passage of an electric current. Depending on the properties of the soil, the resistivity will be more or less significant.

The study of resistivity at depth (electrical imaging, tomography) has become more common, often using long lines of multiplexed electrodes. These methods are used for specific problems such as investigating burial mounds, steep slopes (requiring topographical corrections) or historic sites (Gaffney, 2008).

The **Electrical Resistivity Tomography (ERT)** is an active geophysical method that can provide 2D or 3D images of the distribution of the electrical resistivity in the subsoil. The relationship between the electrical resistivity, current and the electrical potential is governed by Ohm's Law.

A direct current is injected into the ground by two current electrodes (C1 and C2) and the resulting potential is measured by the potential electrodes (P1 and P2). Horizontal and vertical resolutions are determined by changing the inter-electrode spacing according to the survey objectives. Values of apparent resistivity are obtained towards many sets of four electrodes by shifting each time by one electrode the electrode spacing.

Since the 1950s, a variety of electrode arrays have been developed and applied in electrical exploration methods, including Pole-Pole (PP), Pole-Dipole (PD), Dipole-Dipole (DD), Schlumberger (SC), Wenner (WN) and the multi-gradient array (GD) (Zhou et al., 2020).

The suitability of an array depends on many factors; among which are its sensitivity to the target of interest, signal-to-noise ratio, depth of investigation and lateral data coverage (Loke et al., 2013). To interpret effectively the electrical data, the field measurements must be inverted after acquisition.

Resistivity depends on several factors such as water saturation, porosity, salinity and the type of geological deposits. The two extreme values are cavities, which are empty and characterised by extremely high, "infinite" resistivity values and metals, which have resistivity values close to zero. It should be noted that a negative resistivity does not exist from a scientific point of view. However, negative apparent resistivities are frequently encountered during field data acquisition. They are often considered the result of measurement errors or noise. However, it is possible that negative apparent resistivity may be caused by a geological structure or a deposit. This can occur in cases of extremely high resistivity contrasts, due to the positioning of the potential dipole (*e.g.*, dipole–dipole configuration) or in situations of near contact. It happens when the current source is located very close to one side of the conductive body (Lee & Cho, 2020).

Variations in resistivity in the subsurface make it possible to distinguish different zones that can be associated with geological layers or anthropogenic deposits. If the variations are weak, it is difficult to distinguish anything. Anthropogenic deposits are characterised by relatively high resistivity values and therefore often have a resistivity contrast with their geological environment. Moreover, if the salinity is high, the electrical resistivity drops and becomes quite low. Hollow structures like pits can also be detected. If they are filled with coarse, unsaturated deposits, the resistivity will be high, whereas if the fill material is clay or saturated sediments, the resistivity will be lower; from a physical point of view, this means that the electric current propagates easily through them (Dabas, 2018).

Figure 1 shows an example of ERT data processing. The first image displays the apparent resistivity pseudo-section, which corresponds to the raw data collected in the field using multi-electrode configurations. These values do not directly reflect the true resistivity of the subsurface. The second image shows the inversion result, which transforms the measured apparent resistivities at the surface into true resistivities that can be associated with certain types of deposits or lithologies. The goal here was to characterise the subsurface of the Neuss-Norf archaeological site and to detect buried remains (Ibraheem et al., 2021).

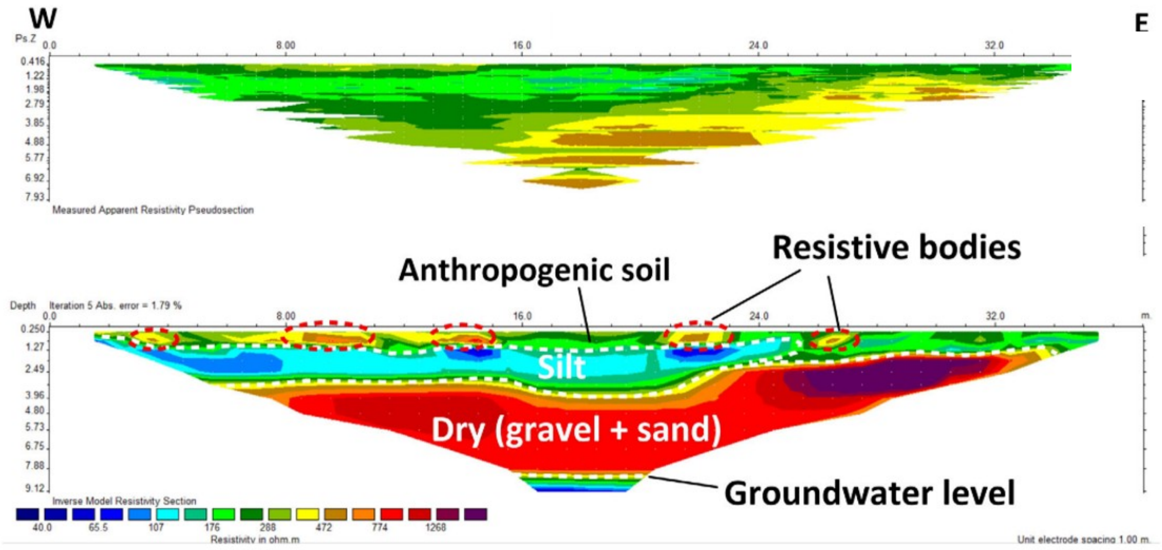

Figure 1: Example of measured apparent resistivity pseudo-section of a profile and the result of robust inversion (absolute error = 1.79) (Ibraheem et al., 2021).

In 2001, a system capable of taking continuous measurements was developed: the electrodes are replaced by spike wheels on an isolated axle (ARP® system), which is pulled by a quad or an all-terrain vehicle. Each wheel is an electrode. The electronics allow for rapid measurements with a fixed step and for positioning the measurements in real time with a GPS. With a quad, it is thus possible to survey several hectares per day depending on the terrain conditions. In archaeology, the step should not be too large, for example 10 cm and the data are generally taken by carrying out parallel profiles spaced one meter apart. It should still be noted that it is difficult to detect small-volume structures if the burial depth is significant compared to the size of the object (Dabas, 2018).

The **Induced polarisation (IP)** could be used currently to search buried roads or the investigation of industrial sites (Gaffney, 2008) although this is not the most used method. It uses the same electrode configuration as ERT but applies a pulsed current and records the transient voltage decay (or phase shift) to assess the material's polarisation.

The second class of methods is **magnetic methods**. The aim here is to measure variations in the Earth's magnetic field. The parameter is magnetic susceptibility, which reflects the ability of a body to become magnetised. The carriers of susceptibility are iron oxide particles present in all soils and subsoils. They partly come from the weathering of the parent rock and are therefore an indicator of the evolution of the soil and subsoil, but human activity can also favour or hinder the creation of these iron oxides. A well-known mechanism is fire, which promotes the transformation of certain iron oxides into more magnetic forms that can then be detected. It is easy to distinguish fired clays or magnetic objects such as "slags" (Dabas, 2018). This method is valuable for mapping ancient settlements, identifying buried kilns or hearths and tracing ancient roads or pathways based on magnetic anomalies caused by burned materials or metal artefacts (Eppelbaum et al., 2024). It is also possible to detect ditches, which are characterised by low magnetic susceptibility. Nevertheless, the link between a geophysical anomaly and a buried archaeological structure is often unclear, as the material causing the anomaly usually cannot be identified without excavation. Interpretation depends on whether the magnetisation is induced by the present Earth's magnetic field or is remanent, reflecting an ancient magnetic field (Fassbinder, 2017).

The magnetic methods are faster than the electrical method because it is possible to use several sensors simultaneously and thus reduce the distance to be covered. The problem with this method is magnetic pollution, as the presence of pylons and power lines or buried pipelines creates very strong signals that then interfere with weaker signals from buried archaeological structures. This method is also sensitive to weather conditions. This method is a bit less universal than the electrical method because the existence of a magnetic signal due to archaeological structures is not systematic: some structures are not magnetic or have lost their magnetism. Magnetism favours more superficial anomalies and it is more difficult to determine the depth of a detected structure (Dabas, 2018).

Magnetometry (MAG) is the most common geophysical method in archaeology. It now employs fluxgate or optically pumped (caesium system) sensors, which outperform the older proton systems. Fluxgate instruments measure the vertical component of the Earth’s magnetic field, while optically pumped systems record the total field. Their rapid data acquisition and effectiveness in shallow investigations make them a preferred tool (Gaffney, 2008).

Another class consists of **radar methods** (radio detection and ranging). Radar prospecting depends on the dielectric constant, which represents the ability of a material to polarise under the effect of an electric field and is closely related to the presence of water in the soil. The aim of this method is to emit a high-frequency electromagnetic wave using an antenna. The echoes produced by the different materials encountered by the wave are received by a receiving antenna. Then, knowing the propagation speed of the wave in the medium, it is possible to deduce the distance and thus the depth of the object that reflected the wave. This method therefore allows a fine estimation of the depth of structures (Dabas, 2018).

The radar used in archaeogeophysics is Ground-Penetrating Radar (GPR). In the last decades, GPR has become a frequently used technique for the non-invasive investigation of Roman urban sites. For the investigation of Roman urban settlements, waves with frequencies between 200 and 800 MHz are used (Mainet & Graziano, 2022). Higher frequencies provide better resolution but shallower penetration, while lower frequencies allow greater depth at the cost of detail. GPR must be in contact with the ground, so if the soil is ploughed or there are stones on the surface, the coupling with the antenna is poorer. Therefore the measurements taken are of lower quality. GPR can help to locate structural remains, can identify changes in soil stratigraphy, detect buried artifacts and characterised ancient landscapes, such as human-made channels or buried geological formations (Eppelbaum et al., 2024). This method is more expensive but more robust than the others.

The GPR technique is based on the reflection of radio waves at transitions between materials with different moisture content (Figure 2a). GPR surveys are done by making parallel lines spaced 5-10 cm apart in archaeology, using continuous data acquisition. During the survey, the instrument measures the amplitudes of the reflected waves and the two-way travel time, which is the time it takes for a wave to travel from the GPR transmitter antenna to a subsurface reflector and back to the receiver antenna (Figure 2b). Results are shown in a vertical profile or radargram. The radargram shows the amplitude as a function of the two-way travel time, which after processing is converted to depth (on the vertical axis) and, as a function of the position of the GPR instrument when the measurement was taken on the horizontal axis (Figure 2c). By combining several parallel profiles, horizontal slices can be extracted at different depths (Figure 2d-e) (Mainet & Graziano, 2022).

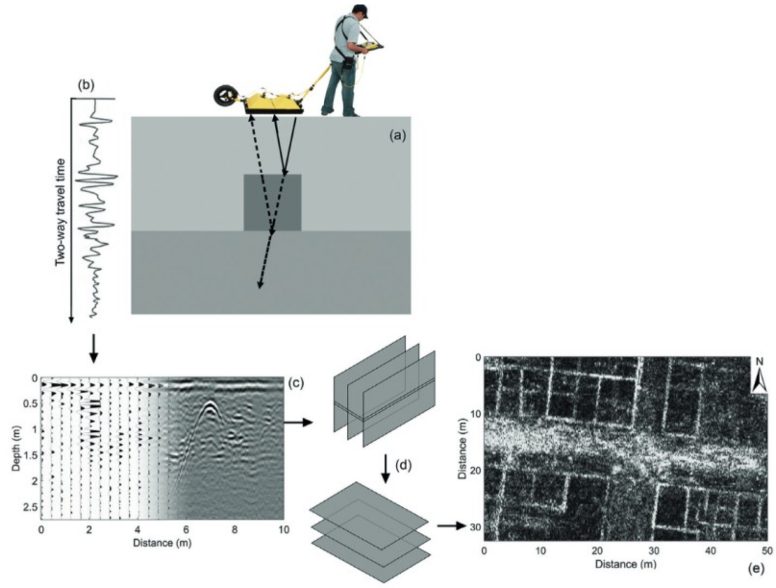

Figure 2: Diagram of the operation of the GPR method (Mainet & Graziano, 2022).

It is possible to multiply the number of antennas (up to 32 antennas), which allows a field to be prospected much faster, but it is also much more expensive (Dabas, 2018). This multi-antenna system is tracked by motorised vehicles with GPS.

There is also the **electromagnetic survey** (EM).

Electromagnetism induction is an active method that does not require direct ground contact. In this method, a transmitter coil (Tx) emits a primary electromagnetic field (H_p) oscillating at a specific operating frequency. This primary field includes a magnetic component that varies in both time and space. When it penetrates the subsurface, it induces Eddy currents, whose intensity is directly proportional to the electrical conductivity of the underground materials. As these currents circulate, they produce a secondary electromagnetic field (H_s). Both the primary and secondary fields are then detected by a receiving coil (Rx) (Figure 3a). The measurement of the imaginary component of the ratio between the secondary and primary fields (H_s/H_p) is used to derive the apparent electrical conductivity of the subsurface (Figure 3b). It is also possible to measure the apparent magnetic susceptibility related to the phase part of the ratio, which is linked to soil texture (De Smedt et al., 2013); (Blanchy et al., 2024).

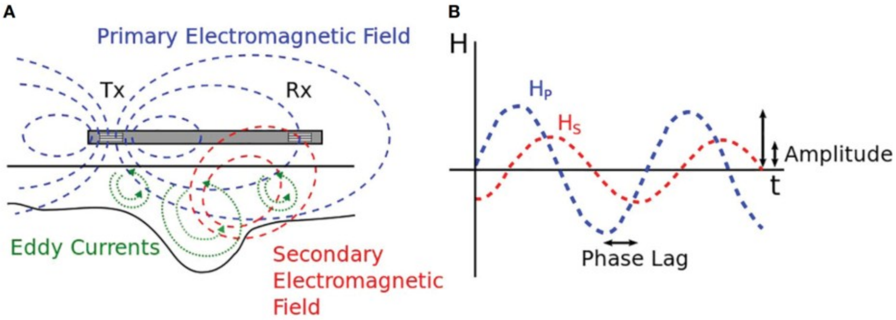

Figure 3: Internal working of an FDEM instrument. (a) Schema of transmitter coil (Tx) and receiver coil (Rx) and electromagnetic fields (H_s and H_p), (b) graph given the amplitude ratio (H_s/H_p) and the phase shift between primary and secondary fields (McLachlan et al., 2021).

Most commonly, a single-frequency device with multiple receiver coils is used. shows an example of such a multi-receiver coils instrument for geophysical surveying called 'Dualem-21S'. It is composed of one transmitter (T) and four receivers with two orientations: perpendicular coplanar (PRP) and horizontal coplanar (HCP) (Figure 4a). This setup allows simultaneous investigation at different depths: the larger the distance between the transmitter and receiver, the deeper the depth of investigation Figure 4b).

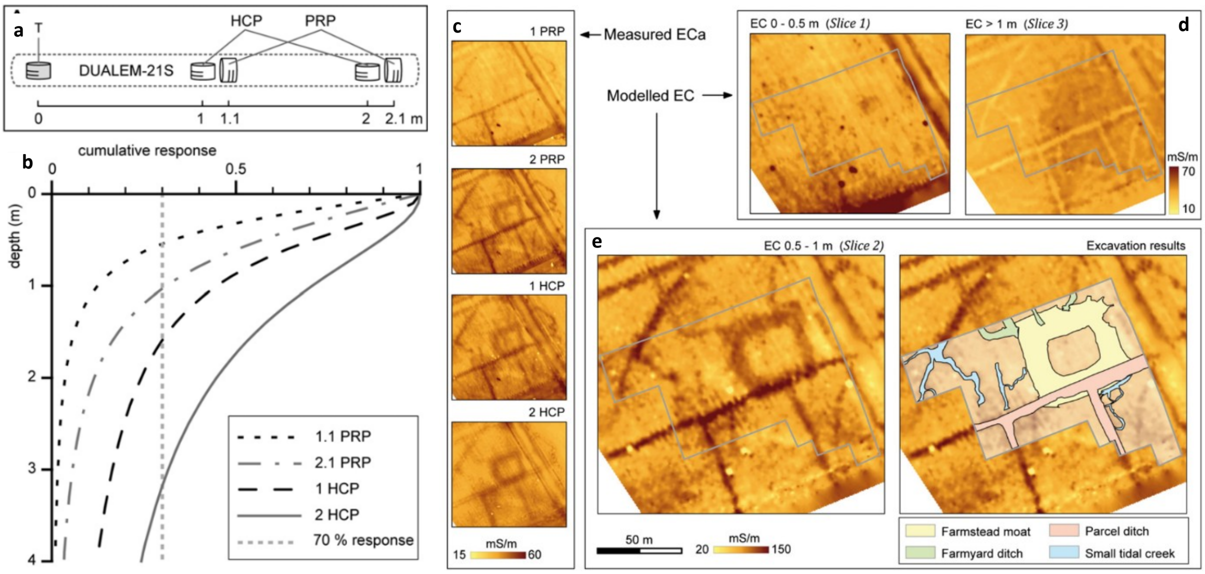

Figure 4: (a) Schematic representation of the Dualem-21S EMI, (b) depth response functions, (c) ECa measurements for each coil, (d) modelled EC of the soil volume, (e) sensor with and without excavation results (De Smedt et al., 2013)

Figure 4b shows the measured apparent electrical conductivity obtained with the instrument for each receiver. In this representation, the distinction of archaeological features may be obscured by near-surface soil noise and debris. d illustrates the modelled electrical conductivity using an inversion method called "EC-slicing" for three predefined soil volumes beneath the ground surface. Finally, Figure 4e presents slice 2 with the archaeological excavation results overlaid to assess whether EMI can detect archaeological features (De Smedt et al., 2013).

It is also possible to use a multi-frequency instrument composed of a single transmitter–receiver pair operating at different frequencies. Lower frequencies allow for greater investigation depths.

This method is considered more effective at archaeologically significant depths than single-sensor instruments, offering improved efficiency and depth penetration (Gaffney, 2008).

The **gravimetry** is used episodically to identify voids under buildings or on open sites (Gaffney, 2008).

The **seismic refraction surveys**, less used in archaeogeophyics, can assist in outlining subsurface stratigraphy and identifying buried geological features that may impact human settlements patterns (Eppelbaum et al., 2024). Seismic methods are based on the propagation of seismic waves through the ground and subsurface. Refraction seismics relies on the study of refracted waves between two subsurface layers with different physical properties. It works by analysing the propagation of P-waves (compression waves that travel longitudinally) and S-waves (shear waves that propagate perpendicularly through the subsurface). P-waves are the fastest and are the focus of refraction seismics, as the method aims to determine the travel time of the first-arrival waves at the geophones. The primary assumption of this method is that wave velocity increases with depth; thus, the deepest layers must have the highest propagation speeds.

The surface waves surveys can also be used. Surface wave methods, on the other hand study seismic waves that travel along the ground surface. These waves are generally slower but have a greater amplitude. Two main types are distinguished: Rayleigh waves, which propagate mainly in a vertical elliptical motion and Love waves, which move horizontally.

Table 1 is a summary of the different geophysical methods used in archaeology with their advantages and disadvantages.

Table 1: Archaeogeophysics methods summary

Methods	Advantages	Disadvantages	Applied examples
Magnetometry	+ Rapid to deploy + High spatial resolution	- Magnetic pollution - Sensitive to weather conditions	▪ (Argote-Espino et al., 2022)
EM	+ Rapid and simple to deploy + Quick interpretation + Measurements at multiple depth simultaneously + Capable of surveying very large areas	- Disturbed by external electric and magnetic field - Difficult to implement in urban zones - Conductivity influenced by multiple factors	▪ (De Smedt et al., 2024) ▪ (Mohamed et al., 2023) ▪ (De Smedt et al., 2013)
GPR	+ High vertical and horizontal resolution + High spatial resolution + 2D and 3D visualisation + Sensitivity to non-metallic objects	- Costly - Clutter and multiple reflections - Requires a flat, unobstructed surface - Limited penetration depth	▪ (Mainet & Graziano, 2022) ▪ (Forte et al., 2021) ▪ (Capozzoli et al., 2022)
ERT	+ Applicable at various scales + Simple to implement + 2D and 3D visualisation + Resolution at depth	- Non unicity for the inversion - Water and clay sensitivity - Sensitive to surface conditions - Sensitive to surface conditions	▪ (Wunderlich et al., 2018a) ▪ (Wunderlich et al., 2018b) ▪ (Cardarelli et al., 2016) ▪ (Ibraheem et al., 2021)
Seismics	+ Deep penetration + Quantitative data + Versatile acquisition	- Costly - Ambient noise issues - Non-unique interpretation - Sensitive to surface condition	▪ (Wunderlich et al., 2018b) ▪ (Guan et al., 2022)
Gravimetry	+ Very precise measurement + Applicable at various scales	- Costly - Require numerous corrections - Complex interpretation	▪ (Pašteka et al., 2020)

Combining data from several geophysical methods is essential to improve the interpretation of results and mathematical and statistical integration methods can be useful for rigorous and systematic interpretation (Gaffney, 2008).

There are different approaches to **combining data**. The first is joint interpretation, where the different datasets are processed or inverted separately and then interpreted together. With this approach, ambiguities inherent to the model parameters may remain (Hellman et al., 2017).

Another approach to data integration is **joint inversion**, which combines different datasets to solve an inversion problem and produce a more accurate, less ambiguous subsurface model. In some cases, this takes the form of a common-parameter inversion, where distinct datasets are inverted for a shared parameter. A related technique is constrained inversion, often applied to geoelectrical data such as electrical resistivity tomography (ERT) or seismic refraction tomography, which are inherently ambiguous since several subsurface models can fit the data equally well. Here, complementary datasets or ‘a priori’ information from other geophysical methods or core analysis are used to guide the inversion and improve the reliability and accuracy of resistivity tomographic images. For example, ERT may fail to detect a boundary with low resistivity contrast, whereas seismic methods could reveal it through a high velocity contrast (Hellman et al., 2017).

Finally, in **coupled inversion**, separate datasets constrain each other; for instance, in structurally coupled inversion, the structural model of one property guides the inversion of another and vice versa (Hellman et al., 2017).

More recently, Isunza Manrique et al. (2023) proposed a probabilistic approach for the quantitative interpretation of inverted geophysical data, aiming to integrate information from multiple sources. This method involves classifying inversion results by combining several datasets. It is based on Bayes theorem and the principle of ratio permanence to compute the joint conditional probabilities of each lithological category, while simultaneously accounting for all sources of information within the inverted domain.

A major strength of this approach lies in its ability to be extended to a wide range of geophysical methods. Furthermore, it incorporates uncertainties related to measurement noise and inversion artifacts, leading to more robust classifications, particularly in contexts where field data are limited. This method will be employed in the master thesis and will be discussed in greater detail in Section 5.5.

3. Ostia Antica

3.1. Context

The archaeological site covers an area of approximately 1.5 km^2 and has an average elevation of about 2.5 m above the sea level (Mastrorillo et al., 2016). Ostia, located about 30 km southwest of Rome in the Latium, lies at the mouth of the Tiber River, on the western coast of Italy, facing the Tyrrhenian Sea (Figure 5).

Figure 5: Localisation of Ostia Antica

3.1.1. Archaeological context

Ostia is one of the most extensively excavated cities of the Roman period. The Roman city of Ostia, as visible today, is a palimpsest of buildings mainly dating to the Imperial period, particularly the 2nd century BCE (Before the Current Era) (Salomon et al., 2018).

According to ancient authors, Ostia is said to have been founded by Ancus Martius, who was the fourth of the seven kings of Rome and reigned between 646 and 616 BCE while archaeological evidence dates its foundation to the IVe/IIIe century BCE. This date is associated with Ostia's primitive fortress called the “Castrum”. So, there is a discrepancy between literary tradition and archaeological fact. Geoarchaeology offers additional insights for reflection to know if there is a Paleo-Ostia before Ostia Antica (Salomon, 2020).

According to Le Gall, 1953; Segre, 1986; Giraudi et al., 2019 and Salomon, 2020, it is essential to link the development of the city of Ostia with that of the mouth of the Tiber. In fact, the etymology of the name Ostia is derived from the Latin term *ostium*, which signifies “mouth”. A river mouth is an extremely mobile point in space and time, depending as much on the position of the coastline as on the river channel. Recent work shows that the mouth of the Tiber has affected Ostia Antica. Palaeo-Ostia may also have been affected by the dynamics of the river mouth (Salomon, 2020).

The city walls were built between 63 and 58 BCE, enclosing an area of approximately 70 hectares. Significant urban transformations took place toward the end of the 1st century and during the 2nd century BCE, especially during the Hadrianic period. The warehouses of Ostia date back to the 1st century BCE, highlighting the city’s crucial role as a port supplying Rome (Salomon et al., 2018; Salomon et al., 2020).

The main function of Ostia was to protect the river mouth of the Tiber and to supply Rome with goods using the Tiber water way. It is assumed that the urban layout of Ostia reflects both natural and anthropic factors that shaped the city over time, such as the location of the coastline and river channel, planning strategies, land division and socio-economic processes (Salomon et al., 2018). Ostia’s harbour capacity grew due to increasing imports from all over the Mediterranean. After a period of major economic prosperity in the II^{e} century BCE, the city entered a significant economic crisis so that large parts of the storage facilities were abandoned and the population considerably decreased. However, the reasons for both the boom and the subsequent economic decline are still not well-understood (Hadler et al., 2020).

Recent geophysical surveys have shown that the city of Ostia also extended to the northern bank of the Tiber (Isola Sacra), suggesting that the entire Tiber channel at Ostia was used as a linear port. A geo-referenced digital map of Ostia has been created based on streets, walls and roads uncovered by archaeological excavations, visible structures identified through aerial photography and results from geophysical surveys (Figure 6) (Salomon et al., 2018).

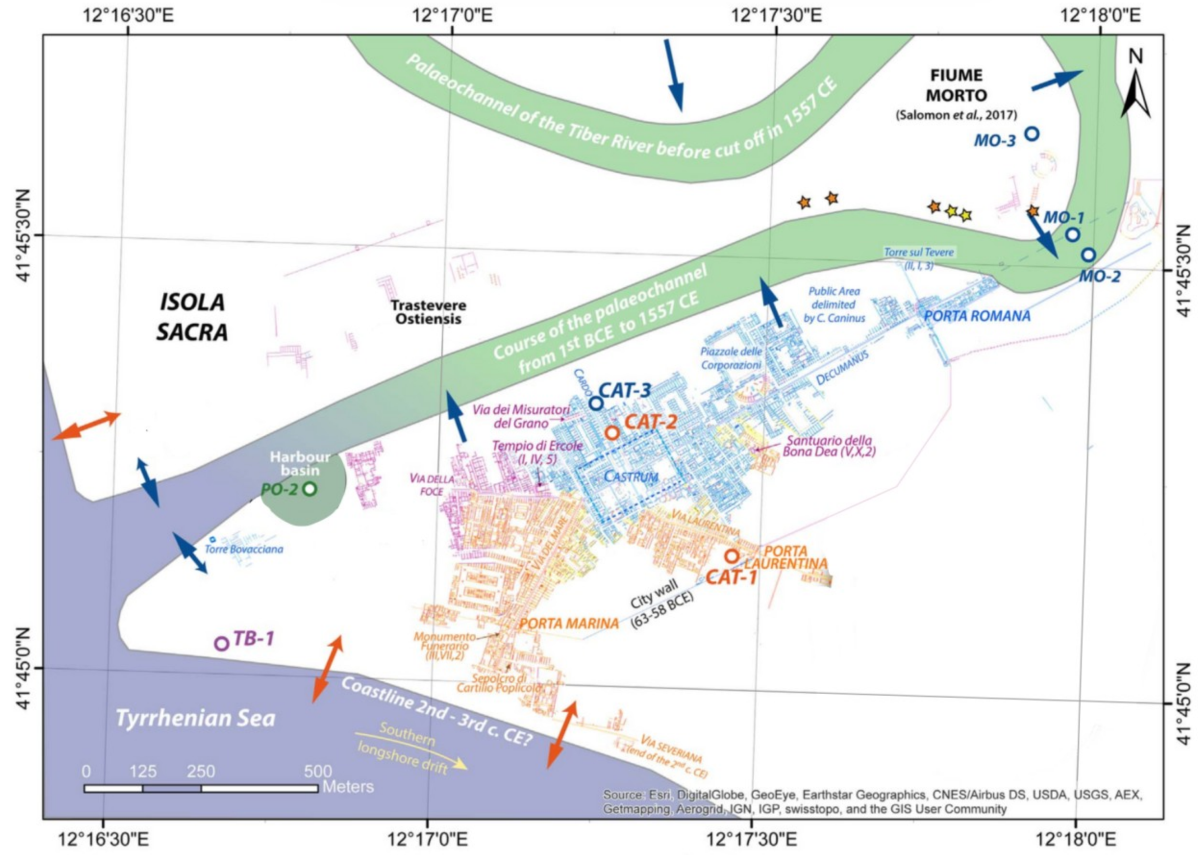

Figure 6: Archaeological features in Ostia (modified after Salomon et al., 2018).

Anthropic features, such as pavements and foundations of Roman buildings, are associated with relatively high resistivity values, allowing these structures to be distinguished from the surrounding geological formations. This is also true for ancient masonry structures such as city walls, which often exhibit even higher resistivity values due to their compact and dry construction materials (Cardarelli et al., 2016; Hadler et al., 2020). These contrasts are particularly useful for identifying buried archaeological remains through ERT and EMI surveys.

Riverbanks are typically characterised by heterogeneous sedimentary structures composed of interbedded sands, silts and clays deposited by fluvial processes. They often show moderate to low resistivity due to high moisture content and fine-grained sediments, although gravelly deposits may exhibit higher resistivity.

3.1.2. Archaeogeological and geomorphological context

General geomorphological context:

Both Ostia's position and history are directly linked to the late Holocene development of the Tiber River channel and delta. The latter has only developed since the mid-Holocene when post-glacial sea-level rise decelerated, allowing sediment transport and deposition by larger rivers to outweigh the impact of sea-level rise (Hadler et al., 2020).

The Tiber delta sequence (TDS) records environmental and coastal changes in the region and has been intensely studied (Di Bella et al., 2013; Milli et al., 2013). During glacial sea-level low stand the Tiber was characterised by an incised valley that first turned into an estuary environment during the transgressive system phase (TST) and subsequently into a coastal-shelf sedimentary environment during the high stand system phase (HST; Milli et al., 2013) (Hadler et al., 2020).

The Tiber delta plain is composed of three distinct geomorphological units (Salomon et al., 2020):

- The **internal deltaic plain** consists of paleo-lagoons.
- The **external deltaic plain** corresponds to the progradation zone of the Tiber delta since the mid-Holocene. It is characterised by a series of coastal ridges.
- The **Tiber mobility corridor** crosses the internal and external plains from East to West. It includes several ancient fluvial features, the most significant of which is the Ostia paleo-meander, a key indicator of the river's former paths. (Salomon et al., 2020).

Dynamics during the 1st millennium BCE ():

The 1st millennium BCE can be divided in 3 phases: The fluvial dynamics, the littoral dynamics and the Paleo-ostia and Tiber River mouth dynamics (Figure 7).

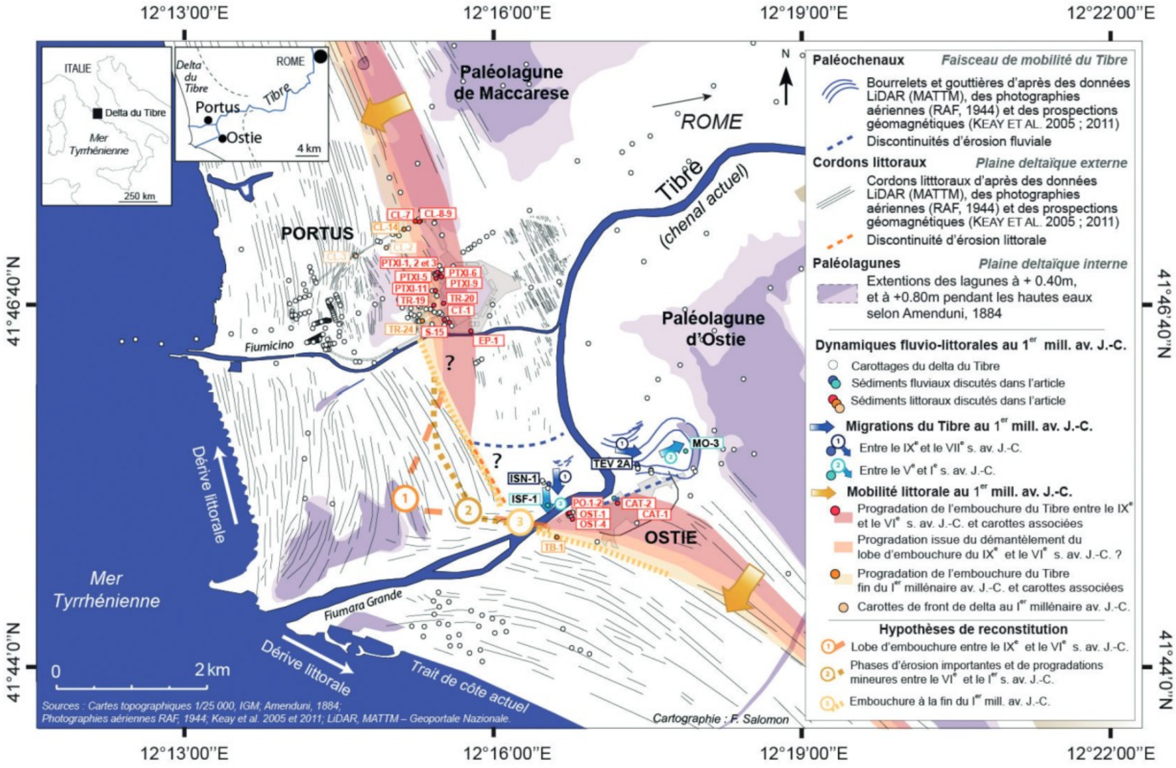

Figure 7: Synthetic map of the available data for reconstructing the dynamics of the Tiber River mouth in the mid-1st millennium BCE (Salomon, 2020).

A) Fluvial dynamics: a southward migration

Near the river mouth, the Tiber's paleochannels exhibit a fine interplay of layers of fine to coarse sands and small gravels. The first millennium BCE is marked by a southward migration of the Tiber's mouth paleochannel and by the formation of the Ostia paleo-meander toward the east. It is also possible that the mouth paleochannel contracted during this period. By the end of the Holocene, the Tiber's mobility corridor was located in the southern part of the Isola Sacra (it's the area north of the Tiber River mouth). It is bounded to the north by coastal ridge deposits and to the south by coastal sedimentation for the first millennium BCE (Salomon, 2020).

B) Littoral dynamics: formation of a significant mouth lobe followed by its erosion

The littoral stratigraphy from Portus to Ostia all show a similar stratigraphy. These consist of very well-sorted sandy deposits with fine horizontal laminations of silty-sandy to sandy-silty types. This regularity in the deposits is interrupted at depths ranging from 9 to 6 m below the current sea level. Between these depths, oblique and cross-laminations, poor particle sorting and interstratification of sandy, silty and organic layers are observed. These organic layers were often sampled for dating as soon as the core was extracted. Deposits between 9 and 6 m have been interpreted as associated with submerged bars along the coast.

Below these submerged bar levels, the mean grain size is less than 200 µm corresponding to fine to very fine sands, while it exceeds 200 µm above these levels corresponding to medium to coarse sands. These depositional characteristics demonstrate the progradation of the coastline in the first part of the 1st millennium BCE (Salomon, 2020).

Sands deposited between 6 and 10 m below the current sea level correspond to the formation of the delta front (submerged littoral domain). The prominent curvature of the coastal ridges observed south of Ostia suggests the formation of an emerged mouth lobe, extending far into the marine domain between the IX^{e} and VI^{e} centuries BCE. Early 17th century maps show the dismantling of this mouth lobe due to erosion. The sediments deposited at the mouth were subsequently redistributed along the coast by littoral drifts both northward and southward. It is likely that this erosion began shortly after the establishment of the mouth lobe and continued throughout the 1st millennium BCE. It is assumed that part of the progradation recorded to the south and north of the mouth is linked to the dismantling of this lobe (Salomon, 2020).

Littoral dynamics during the V^{e} and IV^{e} centuries BCE remain difficult to characterise, as no clear dating exist for the formation of a coastal ridge during this period. At the end of the 1st millennium BCE, a new phase of progradation is associated with the arrival of new littoral areas. During this time, the mouth of the Tiber is located to the west of the operational port of Ostia (Salomon, 2020).

C) Paleo-Ostia and Tiber River mouth dynamics

Figure 7 presents a reconstruction of the evolution of the Tiber's mouth lobe during the 1st millennium BCE. While the presence of a significant mouth lobe formed between the IX^{e} and VI^{e} centuries BCE is well established, its precise position and morphology remain uncertain. Similarly, the exact processes and duration of its erosion are still unknown (Salomon, 2020).

Based on these geomorphological and chronostratigraphic reconstructions, the possible founding of Palaeo-Ostia by Ancus Martius would have between the IX^{e} and VI^{e} centuries BCE, at the end of a period of progradation and the beginning of a long phase of deltaic erosion. (Salomon, 2020).

From Late Antiquity to the Modern Period:

From the end of Antiquity to the Middle Ages, a fluvial environment seems to have been re-established in the region, although stratigraphic evidence remains limited. During this time, the

Tiber meander known as *Fiume Morto* was gradually disconnected from the main distributary channel, a process culminating in a major river flood in 1557 AD. This event definitively separated the meander from the Tiber, leading to lagoon-like conditions and transforming the *Fiume Morto* into a sediment trap for the river's load (Hadler et al., 2020).

3.1.3. Hydrological and hydrogeological context

The course of the Tiber is rather unusual: it follows a general east-west course, penetrating the deltaic plain, but instead of flowing directly into the sea, it abruptly changes direction about 5 km from the current coastline, heading south. The ancient site of Ostia lies within this great bend. This suggests that a major change occurred at some point to the south (Salomon, 2020).

The roman coastal aquifer is a freshwater multilayer aquifer made mostly of Pleistocene and Holocene sandy sediments constituting the Tiber River delta plain. The left bank of the plain coincides with the contact between the Pleistocene transitional deposits and the Holocene coastal and alluvial deposits. In the inner sector of the plain, the stratigraphic composition is made of silty sands, clay and gravel deposited during several Pleistocene transgressive cycles. The outer part is characterised by Holocene deposits, mainly coastal and aeolian sands, passing laterally to the alluvial sediments of the Tiber River (Figure 8) (Mastrorillo et al., 2016).

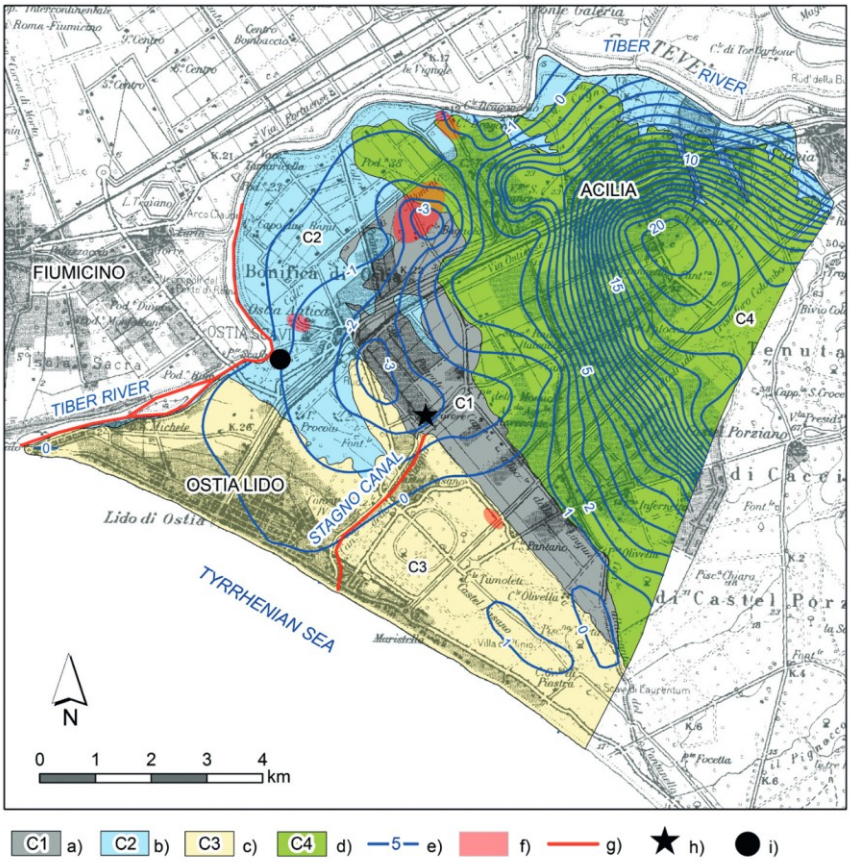

Figure 8: Left bank of the Tiber River delta: hydrogeological settings. (a) Heterogeneous deposits – Holocene, (b) Sandy, silty and clayey alluvial deposits – Holocene, (c) Sandy beach deposits – Holocene, (d) Sandy, silt and clay deposits interbedded with gravels – Pleistocene, (e) Piezometric surface, (f) High salinity area, (g) The seawater's rise in the Tiber River, (h) Ostia reclamation's water pumping station and (i) archaeological site of Ostia Antica (Mastrorillo et al., 2016).

Groundwater flow is limited at the bottom by the low permeability aquiclude (Plio-Pleistocene clay bedrock) and the recharge, exclusively from rainfalls, is ensured by the presence of permeable sands with a higher effective infiltration (Mastrorillo et al., 2016).

The hydraulic connection of the groundwater is ensured by the spatial continuity of the gravel horizons interbedded with the sand and silty layers. In the coastal area, groundwater laterally flows to the Holocene sands, and the aquifer becomes unconfined (Mastrorillo et al., 2016).

The water with higher salinity was found in the inner portion of the area and not by the coastline where it would normally be expected it to rise due to the saltwater intrusion effects. Some of the groundwater high salinity areas are present near the Tiber Riverbank and in the Ostia Antica area. These spots of saltwater contamination could be probably caused by river-groundwater flux exchange processes, because of the rise of the seawater in the Tiber River up to 8 km from the mouth. The observed freshwater-saltwater mixing could also reflect the lasting influence of historical salt production, which spanned approximately 2,500 years and may have left persistent traces in the soil affecting the shallow groundwater (Mastrorillo et al., 2016).

According to the hydrogeological setting, the alluvial sands of Ostia Antica host an aquifer at a depth of 2 or 3 m below ground level, with seasonal water table fluctuations of approximately one meter, recharged mainly through vertical infiltration. Due to the shallow groundwater depth, intense and prolonged rainfall events can trigger groundwater outflow in the archaeological lowlands. After rainfall ceases the residence time of the flooding conditions depends on decreasing velocity of groundwater level.

Near the river mouth, the Tiber flows within artificial embankments, at higher elevation than the local groundwater table. This difference in water levels across the alluvial plain may lead to lateral inflow Tiber water, potentially saline, into the coastal aquifer, a process likely intensified by the drainage pumping system. the Tiber River mouth and this lateral inflow could lead to groundwater salinisation. This hypothesis has been confirmed by the chemical evolution of the groundwater (Mastrorillo et al., 2016).

Hydrogeology and geophysics are closely linked. In the fluvio-deltaic environment, geophysical interpretations must account for variations in subsurface fluid salinity. In the case of Ostia, the salinity of interstitial fluids has a major influence on electrical conductivity. Typically, conductivity is correlated with grain-size distribution, being higher in fine sediments than in coarse sediments saturated with freshwater. However, this relationship can be reversed or obscured by the presence of brackish or saline water, which is common in coastal deltaic settings. As a result, geophysical anomalies must be carefully interpreted considering both sedimentology and fluid chemistry (Wunderlich et al., 2018b).

Electrical and electromagnetic methods are therefore especially well-suited for investigating saltwater intrusion, as they are sensitive to pore-water saturation and salinity. In porous sediments, the overall electrical resistivity primarily depends on the resistivity of the pore fluid, the degree of saturation and the presence of clay minerals. Conductive clays can also reduce overall resistivity, making it difficult to clearly distinguish between clay-rich zones and brackish water. However, at high salinity levels, the influence of clay on conductivity becomes less dominant, so very low resistivity values can generally be attributed to the presence of saline water. Resistivity values below 12 Ω·m are typically considered indicative of brackish or saline water, while values above 15–20 Ω·m are more characteristic of freshwater. A conservative threshold of 7 Ω·m has been chosen to delineate the saline limit. An uncertainty range between 7 and 20 Ω·m is therefore defined to account for measurement uncertainty and the potential presence of clays. Consequently, interpretation should be supported by sedimentological and fluid chemistry data (Cong-Thi et al., 2021).

Today in Ostia Antica, the water table lies only 1–2 m below ground and often outflows into low-lying areas during rainy seasons, causing recurrent flooding of the archaeological site (Mastrorillo et al., 2016). Understanding these present-day hydrogeological dynamics is essential, as they provide analogues for interpreting past environmental conditions that influenced the development and decline of ancient harbour structures (Hadler et al., 2020).

3.2. Summary of previous geophysical studies

Several geophysical methods previously described, such as Electrical Resistivity Tomography (ERT), Ground Penetrating Radar (GPR), seismic surveys, magnetometer surveys and Electromagnetic Induction (EMI), have already been applied at Ostia Antica. The map in Figure 9 illustrates the locations of these surveys conducted both within and around the archaeological site. Various zones have been the focus of study by different researchers. For example, ERT transect 1 has been examined in two studies: Wunderlich et al., 2018a and Hadler et al. (2020), highlighting the continued interest and efforts to investigate the subsurface features of this historically significant area.

Figure 9: Previous studies location (modified after Google Satellite)

3.2.1. ERT

ERT has played a role in the geophysical investigation of the Ostia Antica archaeological and geomorphological context. Several studies applied ERT to characterise subsurface sedimentary architecture, identify buried harbour basins, detect palaeochannels and evaluate the interactions between the soil and the structures.

The study by **Wunderlich, Wilken, et al. (2018)** aimed to delineate the extent of the ancient river harbour of Ostia and reconstruct the infill sequence of the basin. Through a combination of ERT, GPR and seismic methods. They developed both 2D and 3D resistivity models. The ERT profiles were calibrated using vibracore data, allowing interpolation of the sedimentary units across the harbour area. The results of inversion are shown in Figure 10. The principal objective was to distinguish between lagoonal and fluvial depositional phases and assess the potential impact of catastrophic events such as tsunami.

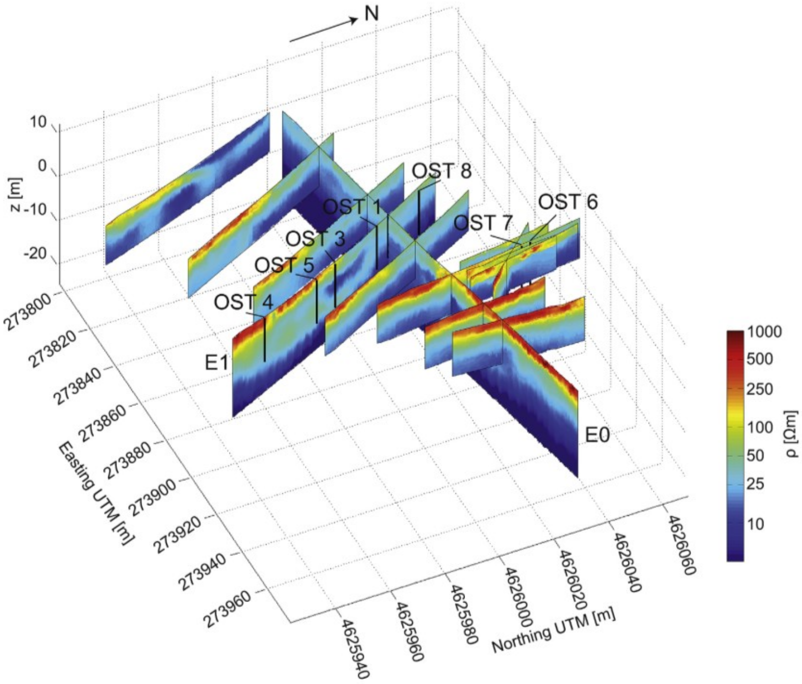

Figure 10: Compilation of 2D ERT profiles into a 3D view of the electric resistivity distribution of the ancient harbour basin of Ostia Antica. Vibracoring locations are indicated by black lines (Wunderlich et al., 2018b).

This study has provided new insights into the structure and evolution of the ancient river port of Ostia (Figure 11).

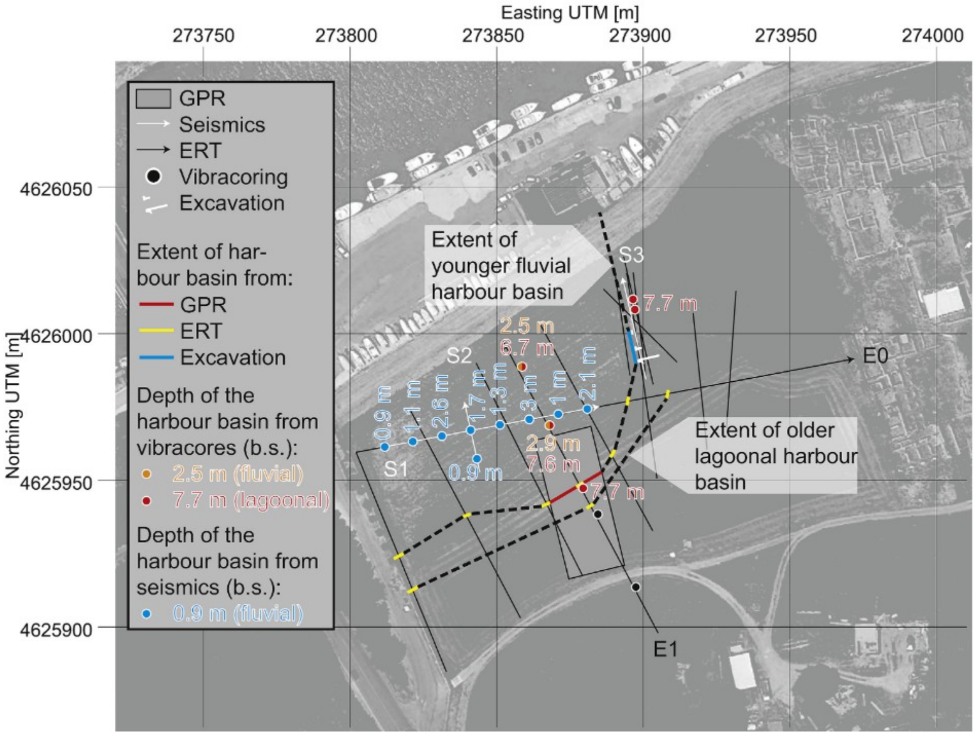

Figure 11: Extent and depth of the two harbour basins derived from various methods. The black dashed lines show the extent of the basins as an interpolation between constraining data basin (Wunderlich et al., 2018b).

The results indicate the presence of two distinct phases of port development. The earlier phase, interpreted as a lagoonal environment, has a basal depth of approximately 7.6 m below the surface. The more recent phase corresponds to a fluvial sedimentary environment, with its base located around 2.7 m below the surface. These two phases are separated by a thin, high-energy, coarse-grained layer, which the authors interpret as a possible tsunami deposit.

Separately, **Hadler et al. (2020)** and **Wunderlich, Fischer, et al. (2018)** used ERT on the Fiume Morto paleochannel to identify successive generations of river channels, to interpret paleogeomorphological evolution. As shown in Figure 12, a total of eleven electrical resistivity tomography transects were conducted using a multi-electrode system (Syscal R1 + Switch 48), employing the Wenner-Schlumberger configuration to optimise both lateral and vertical resolution. Electrode spacing was set at either 1 m or 2 m, depending on the transect.

They also realised DP-EC (Direct Push–Electrical Conductivity) and vibracoring to provide robust stratigraphic control.

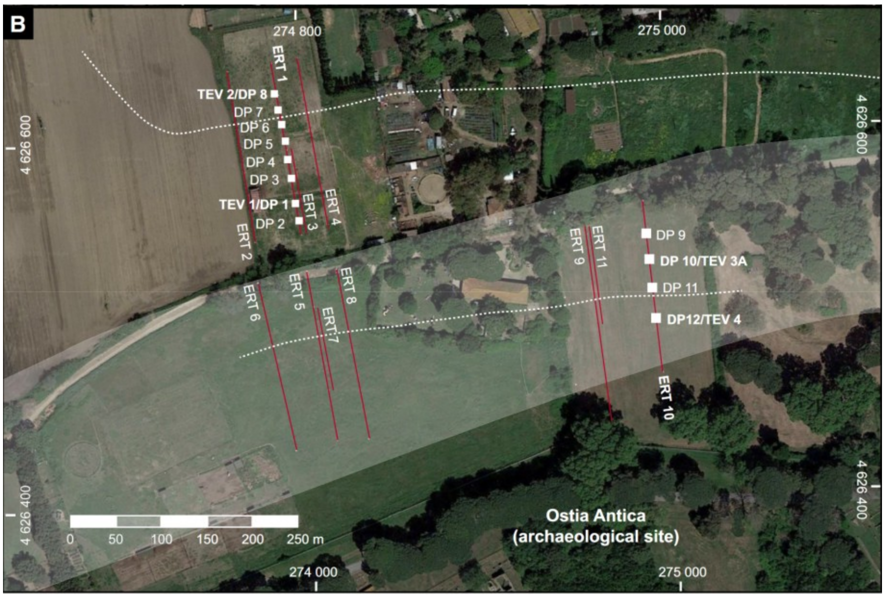

Figure 12: Vibracoring sites (TEV 1A to TEV 4A) and direct push–electrical conductivity (DP-EC; TEV DP1 to TEV DP 12) sites arranged along the Fiume Morto vibracore transect modified after Google Earth (Hadler et al., 2020).

The DP-EC consist of performing in situ soundings to measure the electrical conductivity of the subsurface along a vertical profile. This probe, pushed into the ground, is equipped with four electrodes arranged in a linear Wenner configuration. It continuously measures current and voltage with depth to calculate electrical conductivity. These DP-EC soundings offer high 1D vertical resolution at specific locations along the studied profiles and the maximum depth reached by the probes is approximately 12 m (Hadler et al., 2020).

These two articles share and develop fundamental hypotheses concerning Electrical Resistivity Tomography (ERT) and its application in geoarchaeology, particularly at the site of Ostia Antica. As already mentioned, one of the key challenges is the non-uniqueness of the inversion process and its ambiguity; several models can fit the data equally well.

To reduce this ambiguity, they applied constraints incorporating ‘a priori’ information in addition to the usual smoothness constraints. This prior information was introduced into the inversion by integrating data from vibracores and DP-EC logs. (Wunderlich et al., 2018a).

Because resistivity variations are not solely linked to lithological changes, lithological boundaries and electrical resistivity interfaces may not coincide, particularly at greater depths (Wunderlich et al., 2018a; Hadler et al., 2020).

Consequently, analysing DP-EC logs alone is insufficient for a comprehensive sedimentological interpretation. It is therefore essential to combine geophysical results (ERT and DP-EC) with vibracore analyses and sedimentological and micropalaeontological analyses and radiocarbon dating to produce the most reliable and accurate reconstruction of the subsurface (Wunderlich et al., 2018a; Hadler et al., 2020).

In their methodological study, Wunderlich, Fischer et al. (2018) showed that ERT inversion accuracy improves significantly when geological constraints derived from stratigraphic and DP-EC logs are incorporated. These logs were used to define lateral and vertical regions with preassigned resistivity ranges and tolerances. The inversion space was structurally constrained (by limiting smoothing across interfaces) and electrically constrained (by reducing variability within zones), with resistivity values allowed to deviate up to 50% from DP-EC-derived benchmarks. The goal of this method is to obtain the best possible agreement with the 'ground truth' data.

This approach yielded the lowest relative root mean square error (RRMS) and the strongest correlation with known stratigraphy, especially when using at least five DP-EC logs, as opposed to three.

However, the study also cautioned that imposing continuous structural boundaries across entire profiles may introduce artefacts in laterally heterogeneous environments (Caterina et al., 2014). This can also occur when the a priori information is improperly applied. Such artefacts may also arise if a priori information is improperly applied, producing solutions that fit the measured data but are geologically unrealistic (Caterina et al., 2014). While structural constraints derived from blocked DP-EC data are electrically reliable, applying continuous interfaces over the full extent of the profile can lead to misrepresentations if subsurface structures are not laterally continuous (Wunderlich et al., 2018a).

In conclusion, the most effective approach combines structural and resistivity constraints. It is also essential to ensure a sufficient density and appropriate spacing of DP-EC logs to capture as much of the lateral heterogeneity along the ERT profile as possible.

The Figure 13 shows the results of the inversion of the profile ERT 1.

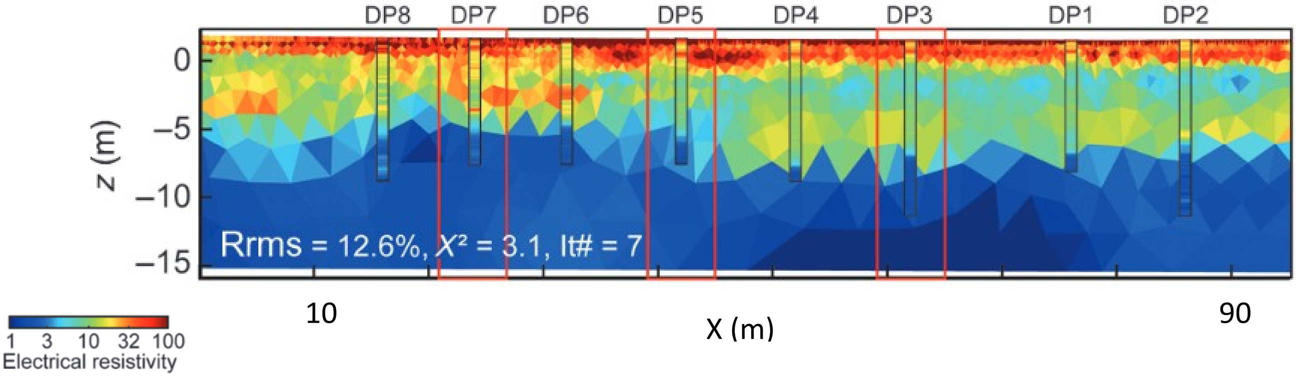

Figure 13: Inversion result with a starting model from five interpolated DP-EC logs (Wunderlich et al., 2018a).[1]

Turci et al. also used ERT, covering the southern area of Ostia Antica (green dotted rectangle in Figure 9). In this case, the ABEM LUND imaging system was employed with a reciprocal Schlumberger-Wenner array protocol, using 1-meter electrode spacing.

Despite the influence of the groundwater table, they were able to detect resistive subsurface structures. These structures range in thickness from 0.8 to 2 m. A general trend indicates that the resistive structures are thicker in the eastern part of the site than in the western part, which may suggest paleontographical features or different phases of occupation (Turci et al., 2020).

Cardarelli et al. has also used ERT in Ostia Antica, they did 2D and 3D profiles to study a specific building called ‘Casa di Diana’ (orange dotted rectangle in Figure 9) (Cardarelli et al., 2016). The results of its inversion are shown in Figure 14.

---

[1] The RRMS of the inversion is maybe a little high

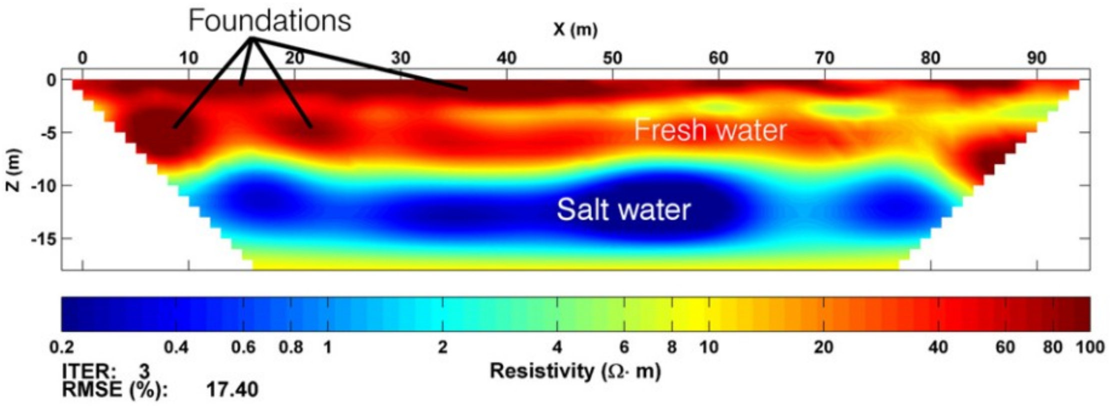

Figure 14: Example of inversion done by (Cardarelli et al., 2016).[2]

All studies using ERT show a more resistive zone near the surface corresponding to the anthropogenic (human-impacted) layer and a much less resistive zone at depth, corresponding to an area saturated with saltwater.

3.2.2. GPR

A GPR (Ground Penetrating Radar) survey was conducted by Mainet & Graziano (2022) in the south-eastern area of Ostia Antica, focusing on the zone near the building known as the Schola del Traiano (located in the north-west of the Figure 15). A 500 MHz antenna was mounted on a wooden cart towed by an all-terrain vehicle. High-resolution positioning was achieved using Real-Time Kinematic (RTK) GPS with 2 cm accuracy. The lines were oriented diagonally (~45°) to known structural alignments to reduce noise (Mainet & Graziano, 2022).

Figure 15 shows the slice which contains all the strongest anomalies from an estimated depth between 30 and 155 cm. On the slices, the white areas are those where the radio waves are reflected more strongly, because of the presence of structures such as stone walls, foundations or paved areas. In the dark areas, radar waves were not reflected, or the reflection was weak (Mainet & Graziano, 2022).

Although most anomalies are of weak intensity, some seem to correspond to buried structures. The most visible anomaly extends the north-eastern limit of the existing building. Two other parallel structures, oriented towards the south-west, could correspond to the delimitation of a new building to the south-east of the Schola, but the second line could be a modern conduit. It is necessary to remain critical and further investigations should be necessary. The GPR made it possible to highlight a large reflective zone that could correspond to a street (light blue area in Figure 16) (Mainet & Graziano, 2022).

---

[2] The RMSE of this inversion is relatively high, in general, it had to be lower.

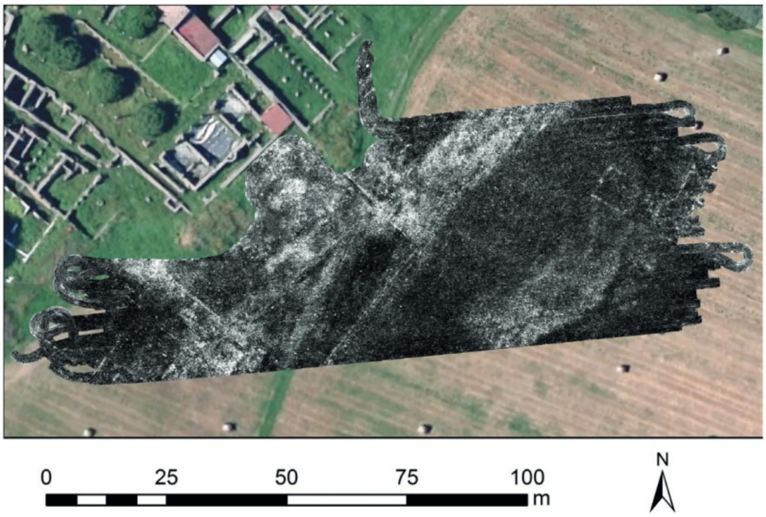

Figure 15: GPR slice containing the strongest anomalies from an estimated depth between 30 and 155 cm (Mainet & Graziano, 2022)

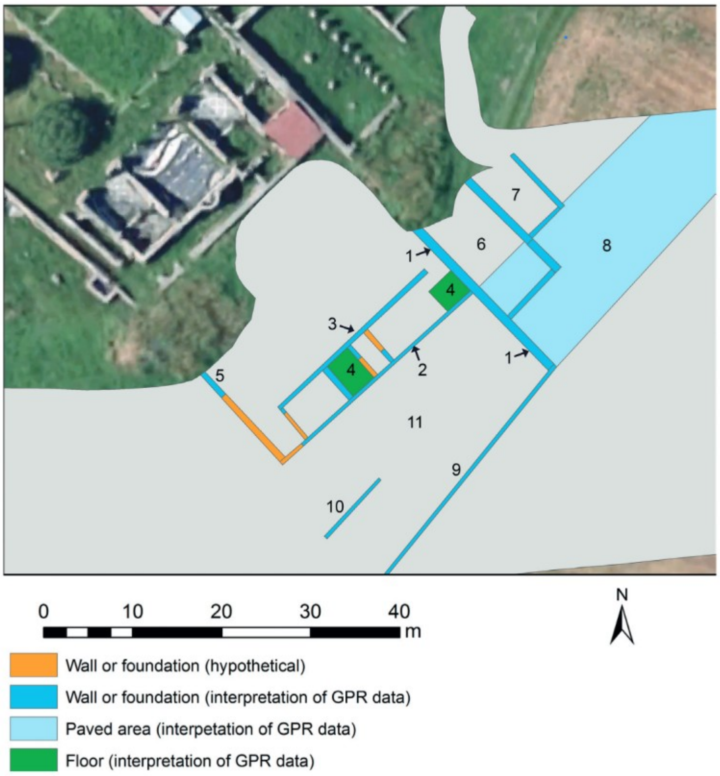

Figure 16: Simplified interpretation of the GPR results from the area adjacent to Schola Traiano (Mainet & Graziano, 2022)

The GPR prospection is only one source of information. Some of the anomalies detected are not clear enough to reach an unambiguous interpretation. Therefore, the confrontation of the GPR data and the aerial photographs with the results of other non-invasive work is necessary to achieve a more comprehensive understanding of the areas subsurface (Mainet & Graziano, 2022).

3.2.3. *EMI and MAG*

The Multi-receiver FDEM instrument was conducted manually. This instrument combines one transmitting coil with six receiver coils alternately paired in perpendicular (PRP) and horizontal coplanar (HCP) geometry with the transmitter. These receiving coils are placed at 0.5 m (HCPH), 0.6 m (PRPH), 1 m (HCP1), 1.1 m (PRP1), 2 m (HCP2) and 2.1 m (PRP2) from the transmitter coil (De Smedt et al., 2024).

EMI measurements were carried out in several areas of Ostia (light blue dotted line in Figure 9). In areas A, C, H and I in Figure 17, linear anomalies potentially indicating buried walls were observed (low ECa). These anomalies sometimes have orientations that differ from surface structures. In A and C area, an ERT profile has been done, their analysis can be therefore compared with the EMI analysis.

Zone J will be also studied again, as three of our ERT profiles cross this area and Ghent University has carried out a new EMI survey, which will be analysed further. In this area, it is already possible to identify the rampart, which appears more resistive. Outside this wall, in the south, lower ECa values suggests the presence of coarser and drier sediments outside the ancient city limits (De Smedt et al., 2024).

Figure 17: Overview electromagnetic induction survey (ECa) (De Smedt et al., 2024)

Magnetic susceptibility is related to the content of clinopyroxenes and magnetite. High values are often associated with the sandy fraction of facies derived from fluvial bedload or with coastal sand placers formed along the shoreline. In the archaeological context of Ostia, remains from the Imperial period (shallow and visible at the surface) are often built with ceramic materials exhibiting high magnetic susceptibility. These can mask deeper Republican structures, mainly built of tuff with lower magnetic susceptibility. High magnetic susceptibility values at the surface reflect strong anthropogenic influence due to the presence of identified Ceramic walls (De Smedt et al., 2024).

Magnetometry data were also collected. Magnetometry is used to detect subtle variations in the Earth's magnetic field attributed to objects or soil disturbances whose magnetic susceptibility or remanent magnetisation contrasts with that of the surrounding soil (De Smedt et al., 2024).

In addition to zones A, C and J, our profile covering zone C also intersects zone D, which was analysed using magnetometry. In Area A, the results suggest the presence of several ceramic-made walls, whose orientation appears to align with that of the permanent remains, the road can also be distinguished (Figure 18).

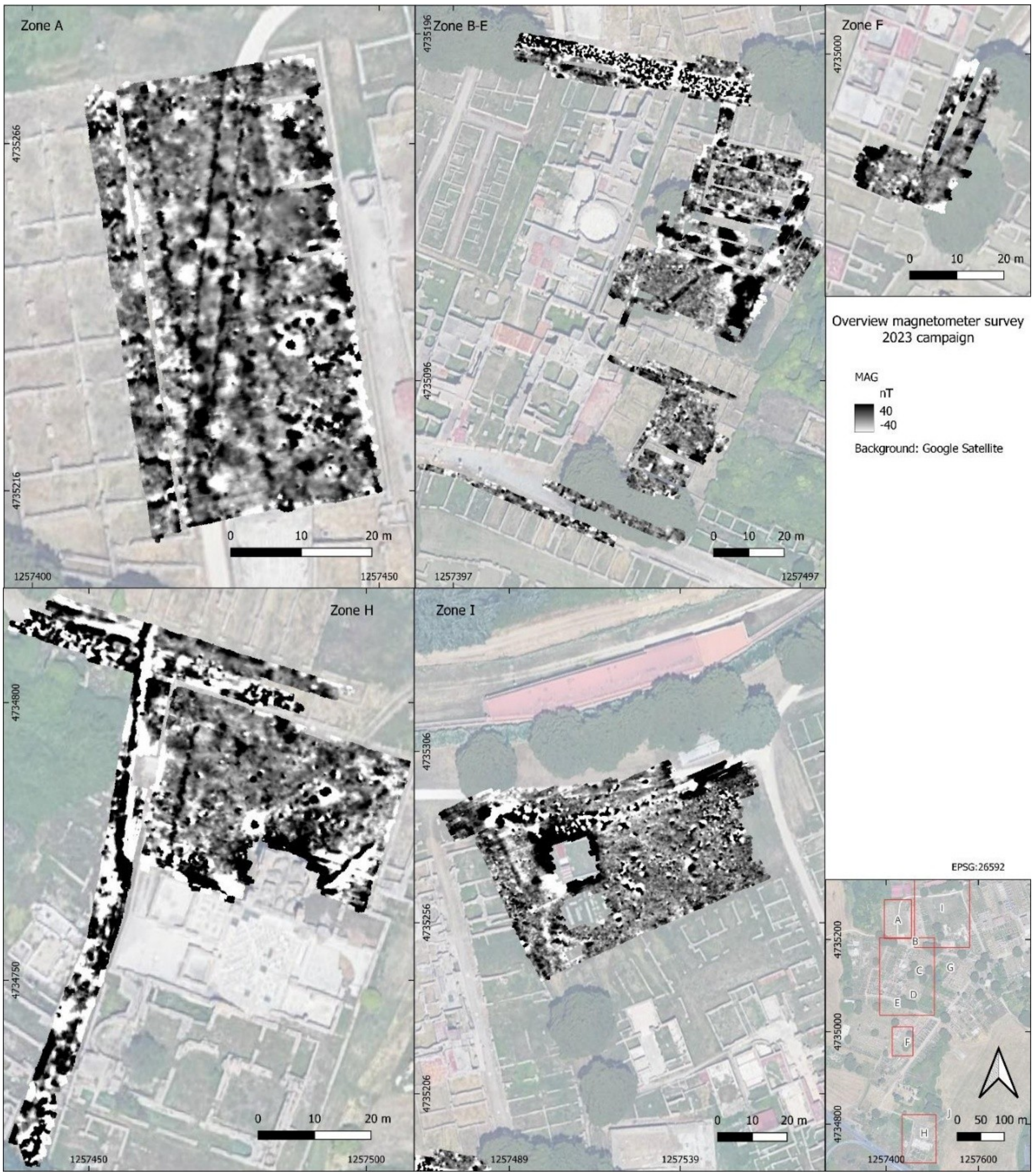

Figure 18: Overview magnetometer survey (De Smedt et al., 2024)

In Zone B, the basalt road surface produced strong dipolar anomalies, making magnetometry ineffective except at a trench location. In Zone C, a previously identified discordant EMI anomaly was confirmed and extended northward through a series of strong magnetic anomalies. Zones D and F showed linear anomalies suggesting buried walls. The analysis of zone E did not bring enormous results (De Smedt et al., 2024).

These data helped identify or confirm several linear archaeological features. These results complemented EMI findings and supported the planning of future borehole investigations.

3.2.4. Seismic

Seismic surveying was used only in the article written by Wunderlich et al, 2018b to investigate the sedimentary infill of the harbour basin.

Three seismic profiles were carried out (shown in light purple in Figure 9). Horizontally oriented geophones spaced one metre apart were used. Shear waves, specifically surface waves of the Love type (horizontally polarised and propagating through a solid medium), were generated by striking a small horizontal steel bar laterally with a hammer (Wunderlich et al., 2018b).

A Multichannel Analysis of Surface Waves (MASW) was performed for two profiles, as standard seismic refraction methods proved ineffective due to a negative velocity contrast. This technique relies on the dispersion of Love waves to examine their variable amplitude sensitivity at different depths (Wunderlich et al., 2018).

The data were first filtered in the frequency–wavenumber domain to remove noise and to normalise the dataset. Then, local wavefields were extracted by multiplying the shot wavefield by a Gaussian amplitude window (Figure 19b). These wavefields were subsequently transformed into slowness–frequency (p-f) spectra (Figure 19c), in which dispersion curves of multiple excited Love-wave modes could be observed. The spectra were finally normalised to the maximum amplitude at each frequency. In the local spectra, the dispersion curves were identified for each offset position and fitted with theoretical curves. Finally, 1D-inversion of fundamental mode was done for each offset (Wunderlich et al., 2018).

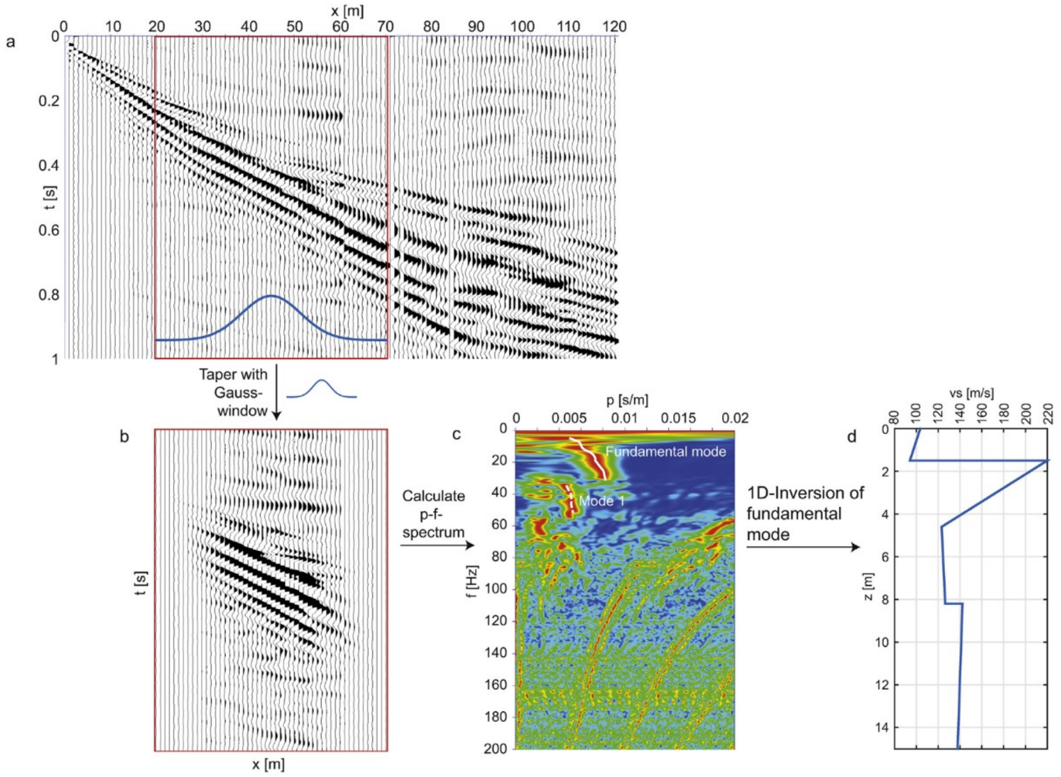

Figure 19: Processing flow seismic profiles S1 and S2. a) Shot gather at 0 m, b) part of Gauss-tapered shot gather around 45 m, c) derived p-f-spectrum of the local wavefield with picked fundamental and first mode, d) resulting vs(z) profile after inversion of fundamental mode. Seismic data was acquired with horizontal geophones with 1 m spacing along the profile.

P-wave refraction tomography could therefore be performed for only one profile. Compression waves (P-waves) were generated by striking a small steel plate placed vertically on the ground with a hammer. In sedimentary environments, velocity typically increases with depth due to progressive compaction. Grain size also plays a role, as it influences both porosity and sediment density (Wunderlich et al., 2018).

The seismic surveys revealed the presence of a layer not detected by ERT. However, although seismic data provide valuable information for extrapolating the results from vibracore analyses, the resolution of seismic imaging decreases with depth and with the distance between the sensors and the target (Wunderlich et al., 2018).

3.2.5. Conclusions

The various techniques used have made it possible to investigate significant and varied depths. Electrical resistivity tomography (ERT) achieves vertical resolutions of around 10 m in the applications carried out here. It has notably been used to map aquifers down to approximately 8 to 10 m for saline waters and around 2 to 5 m for freshwater. Vibracore drilling reached depths of up to 11 m below the surface, while direct push-electrical conductivity (DP-EC) measurements can provide very high vertical resolution data down to about 12 m. Ground-penetrating radar (GPR) is used at shallower depths, with a vertical resolution between 1.5 and 1.7 m. Electromagnetic induction (EMI) reaches depths of about 3 m.

Electrical conductivity is a robust proxy for various subsurface properties, although its interpretation can be ambiguous. ERT can distinguish freshwater aquifers (higher resistivity) from saline aquifers (very low resistivity) and identify building foundations by their high resistivity values. Soil electrical resistivity is mainly influenced by the salinity and saturation of pore fluids, as well as clay content. DP-EC data are proportionally related to the clay and silt fraction of the sediments; however, in brackish or saline environments, this relationship may be reversed due to the increased influence of saline water filling the pores in coarse-grained deposits.

Seismic methods have proven useful for characterising sediments and structures. Seismic tomography, for example, is used to investigate areas prone to cracking and the structure of ancient building foundations. Multichannel Analysis of Surface Waves (MASW) has also revealed a layer not previously observed (approximately 2–3 m below the surface).

The different sources used highlight the importance of integrating multiple methods to overcome the ambiguity and limitations inherent to each technique. Geophysical inversion models, particularly for ERT, can be ambiguous and non-unique, requiring prior information to reduce uncertainty. It is not always possible to achieve sufficient results using geophysical methods alone; combining them with geochemical or geotechnical analyses provides additional and valuable contributions.

The campaigns carried out by the University of Liège in August and September 2024 and in May 2025 were conducted with the aim of improving the geological, hydrogeological and geoarchaeological interpretation of Ostia Antica by performing longer ERT profiles, thereby achieving better vertical resolution. These profiles were also conducted to correlate with cores collected by the University of Strasbourg (Boreholes in Figure 9), to integrate the information and use it to constrain the inversion models. In addition, Ghent University conducted an EMI survey in 2024, which will also be used to provide further data for analysis.

4. Materials and methods

4.1. Purpose of the study

The aim of the survey is to study the subsurface geology down to 20 to 25 m to provide new insights to improve knowledge about the development of the city of Ostia Antica and its paleo-environment. Another goal is to understand the local stratigraphy and to verify the depth at which the boundary between freshwater and saltwater is located.

For the profiles closer to the Tiber River (see Figure 22), an additional objective is to assess whether it is possible to observe the vertical transition between coarser fluvial deposits and the better-sorted sands characteristic of littoral deposits. The survey also aims to characterise and delineate the archaeosphere, as well as to identify potential buried anthropogenic structures.

In addition to the archaeological objectives, this study also aims to propose and test an integrated methodology combining borehole core data, (DP-EC) logs, Electrical Resistivity Tomography (ERT), Electromagnetic Induction (EMI) surveys and seismic surveys. To achieve this, the processing of ERT data will be correlated with sedimentological analyses from cores and DP-EC logs. EMI data will also be examined in conjunction with core information to improve the interpretation of subsurface variations. Where ERT and EMI survey lines overlap, the datasets will be directly compared to assess their consistency and complementarity and to evaluate the potential of EMI as a rapid alternative or supplement to ERT in similar geomorphological contexts. Finally, the surface waves measured along profile R8 will be briefly analysed and compared with the ERT data.

4.2. Drilling and Direct Push

4.2.1. Direct Push

The analysis of the four sediment cores (TEV 1 to 4) allowed the identification of seven major stratigraphic units reflecting different phases of sedimentation visible in Figure 20.

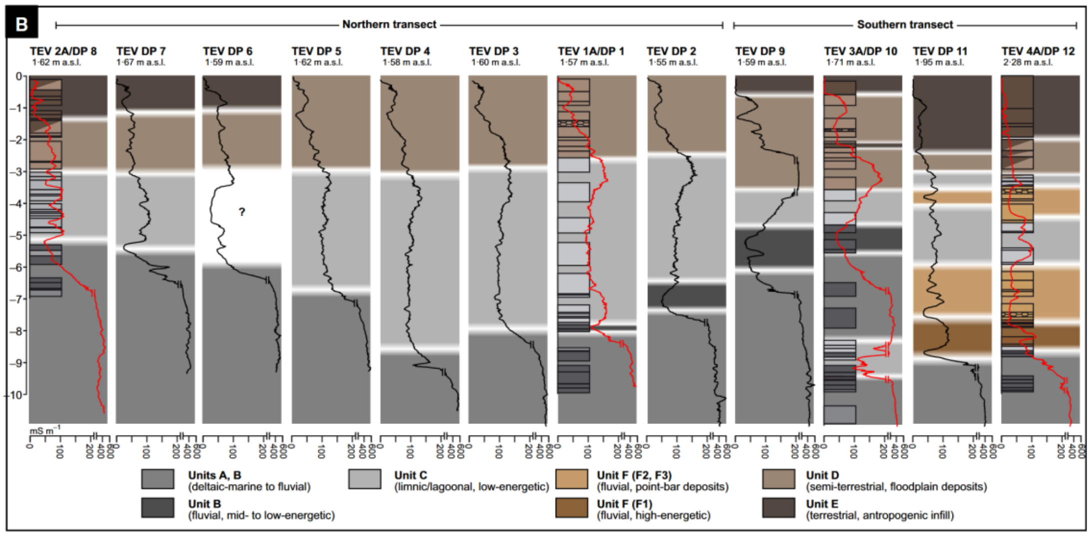

Figure 20: Stratigraphic *sequences and (DP–EC) logs for vibracoring sites TEV 2A, TEV 1A, TEV 3A and TEV 4A along the Fiume Morto vibracore transect (Hadler et al., 2020).*

Marine to deltaic sediments are found in the lower part of the cores (Unit A) and are overlain by fluvial deposits (Unit B), separated by an erosional surface, indicating a phase of Tiber channel development. This is followed by low-energy depositional conditions associated with the establishment of a lagoonal environment within the meander (Unit C), subject to alternating freshwater and saltwater influences. Unit D and E are found in the top of cores and contain anthropogenic deposits (Hadler et al., 2020).

12 direct push soundings were carried out. Of these, 8 were digitised (DP2, DP3, DP4, DP5, DP6, DP7, DP9 and DP11) to estimate conductivity as a function of depth. Based on the analysis of these four cores, it was possible to interpret the DP logs and associate conductivity values with stratigraphic units. Since resistivity is the inverse of conductivity, it was then possible to convert the values into resistivities and associate them with specific facies.

Four of the seven stratigraphic units will be used.

- Salt-water saturated deposits from a marine to deltaic environment (Unit A).
- Silty mud associated with a lagoonal environment (Unit C).
- Silty to sandy mud representing a floodplain environment (Unit D).
- Terrestrial, anthropogenic deposits (Unit E).

The others are not used because they are present in only one or a few of the DP logs used.

4.2.2. Drilling

In 2023, the Strasbourg team conducted a campaign called EOR (Early Ostia Revisited) of 11 shallow boreholes at Ostia Antica. In addition, two deeper cores (S1 and S2) were also drilled. The cores Cat-2 and Cat-3 date from a previous study (Salomon et al., 2018). These cores will be compared with the future geophysical inversions and used for the classification of geophysical data through a multivariate Gaussian statistical analysis such as DPs. Boreholes are represented by white points in Figure 22.

From the analysis of these boreholes, several facies were identified (see annexe 9.1).

In core S1, an alternation of gravels and clay was observed. These facies will not be included in the classification because it is observed only there.

4.2.3. Categorisation of the facies

The inversion does not allow for the distinction of all the facies identified through coring, so certain facies have been grouped into broader categories. Moreover, DP tests reached greater depths than the cores done in 2023 and were carried out approximately 1 km from the study area. Nonetheless, they were included in the classification process to increase the volume of data and improve the robustness of the statistical model.

Based on the analysis of both the cores and DP soundings, six categories were identified:

Category 1: Anthropogenic deposits and silt

This category includes all facies where anthropogenic deposits and silt were observed, according to the observations done by Matthias Delmetz (2024). This category is observed in each drilling and some DPs.

Category 2: Anthropized clay

This category is observed only in the drilling (C2, C4, C5 and C8) and corresponded to a grey silty clay with ceramics and sometimes with organic materials (Delmetz, 2024).

Category 3: Sand

This category is observed in all drilling but is not observed in the DPs. It regroups light and dark sand (Delmetz, 2024).

Category 4: Silt and Sand

This category is observed mainly in the DPs and is composed of silt-dominated mud and sandy mud, but it is also observed in C1 and Cat-2 drilling.

These deposits are also present in cores C4, C5 and C7. They appear to be associated with a lagoonal environment.

Category 5: Silt

This category is mainly observed in the DP logs but is also present in some drillings. It is mostly characterised by greyish silt and mud deposits. Although these silts were identified in both the DPs and the Cat-3 core, they do not correspond to the same depositional environment. Indeed, the silts in the DP tests are linked to a calm, lagoonal setting (Unit C (Hadler et al., 2020)), whereas those in the Cat-3 core are associated with fine fluvial deposits (Salomon et al., 2018).

Category 6: Saltwater-saturated sand

This category is mainly observed in the DP logs because they are deeper but is also present in the deepest boreholes. It consists of sand saturated with saline water with sometimes gravels or fine laminated silts. It is associated with a marine to deltaic depositional environment. These saturated sands are considered a distinct category because the salinity of the water significantly influences the resistivity of the surrounding material (Hadler et al., 2020).

Core C5 is used as an example to illustrate how the categorisation is applied in Figure 21.

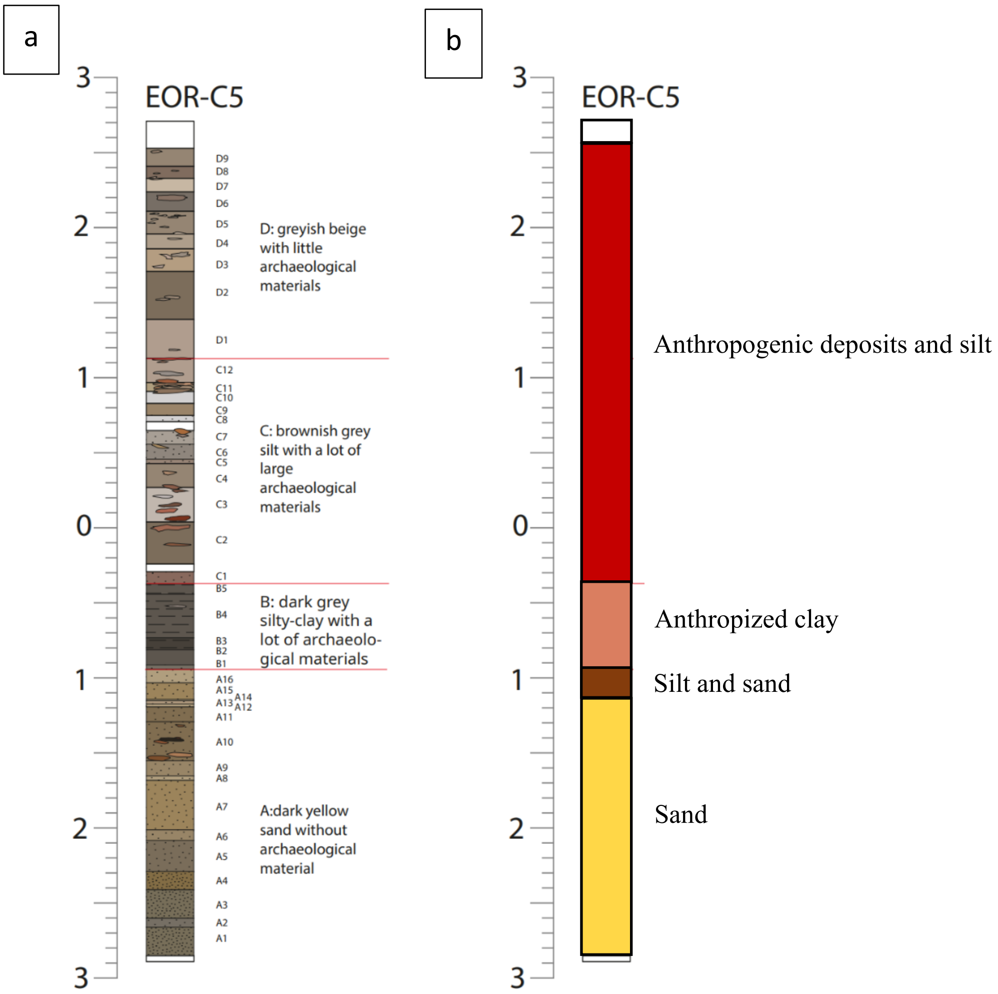

Figure 21: (a) C5 drilling analysed by Delmetz, 2024, (b) Interpretation of the C5 drilling

One more category is used only for the core S1, it is 'Clay + gravel'.

4.3. Fields acquisitions

The data were collected between August 29 and September 5. Nine ERT profiles and three seismic profiles were carried out. In May 2025, others ERT profiles were carried out. Two of these profiles will be studied. All profiles were conducted from north to south, except for profile R9 and the seismic, which were carried out from south to north.

The map in Figure 22 shows the ERT and seismic profiles.

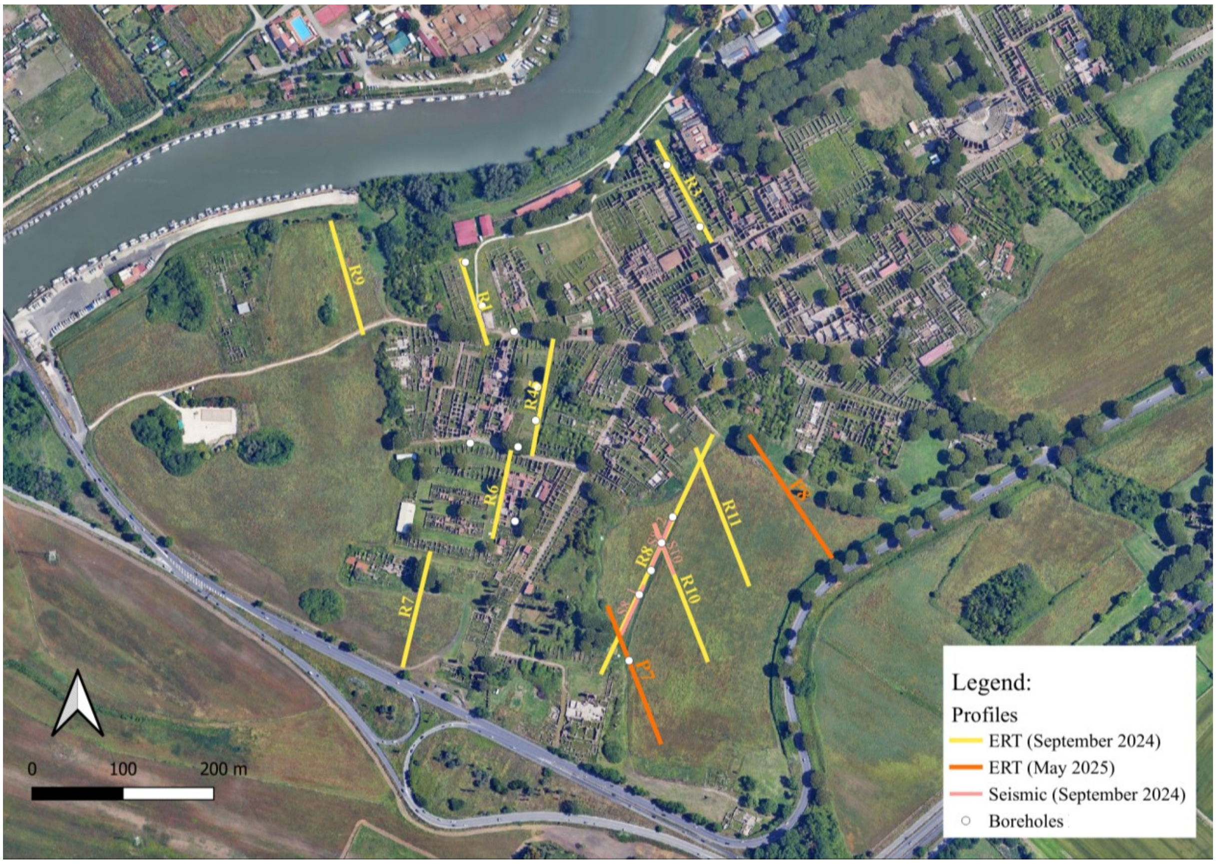

Figure 22: Positions of boreholes and geophysics profiles modified after Google satellite

Using the ERT method, 11 transects were acquired, they have different length:

- Profiles R1 and R6 are 95 m long.
- Profiles R9, R3, R7 and R4-5 are 127 m long.
- Profiles R10, R11, P7 and P8 are 159 m long.
- Profile R8 is 288 m long.

For each profile, the spacing between the electrodes is one meter. Figure 23 illustrates the installation of one ERT profile.

Figure 23: ERT acquisition, profile R3

The data acquisition was carried out using the multi-gradient configuration (GD). GD is suitable for multichannel data acquisition using the ABEM Terrameter LS 2 instrument. It provides well-resolved resistivity images and presents a good signal-to-noise ratio but the horizontal resolution is lower than the vertical resolution (Dahlin & Zhou, 2004).

The survey is controlled by three parameters, named electrode spacing ***a***, separation ***n*** of the current-electrode pair A and B and their moving forward step ***s***. The GD survey is implemented by measuring electrical potential differences (gradients) from all the successive two potential electrodes, M and N, which are all located between the two current-electrode pair A and B (Figure 24).

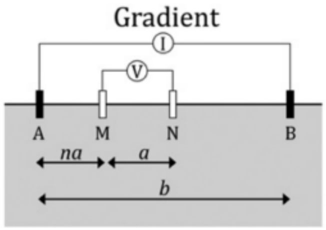

Figure 24: Multiple Gradient configurations, b = (s+2).a with s the maximum number of potential readings for a current injection (Loke et al., 2013) (Modified after Binley and Slater, 2020).

In electrical theory, measuring the potential difference between electrodes M and N following current injection between electrodes A and B is equal to measuring the potential difference between A and B if the injection is done between electrodes M and N, regardless of the resistivity distribution of the subsurface.

During data acquisition, reciprocal measurements are taken in the field to provide an estimate of the noise level for each measurement. However, these estimates do not account for potential procedural errors made in the field or for errors in the data modelling (LaBrecque et al., 1996).

Using the seismic method, 3 profiles were realised, each profiles measure 47 m and the geophones were one meter spacing. For each profile, an offset of 5 m was done at the beginning and at the end. Figure 25 illustrates the installation of one seismic profile.

Figure 25: Seismic acquisition, profile S8_1

For profile S8_2, acquisition was done at each geophone and for profiles S8_1 and S10, there were done every geophone striking a nylon plate with a sledgehammer. Two DaqLink instruments were used.

The position of the electrodes or the geophones for each profile was taken with e GPS with a RTK precision. Elevation measurements will be corrected to align zero level with the sea level measured at Ostia.

5. ERT data processing and results

After data acquisition, the next step is data processing. This phase involves filtering the dataset to remove low-quality measurements and prevent the introduction of artefacts during the inversion process, which is essential for meaningful interpretation of geophysical data. Initially, negative values are excluded, followed by the removal of resistance measurements with a repeatability error greater than 5%.

During modelling, the resistivity is allowed to vary vertically and in one horizontal direction, while the size and position of the cells remain fixed. Various numerical methods can then be applied to compute potential values for the 2D forward model (Loke et al., 2013). Using inverse methods, it is possible to calculate the subsurface resistivity distribution responsible for the observed potential measurements. The next Section outlines the theoretical principles underlying the inversion process and explains how raw field data are transformed into a coherent resistivity model.

5.1. ERT theory

5.1.1. Theory of inversion

Electrical resistance is not an intrinsic property of the medium and must be converted to electrical conductivity or resistivity. To do that, it is essential to use a mathematical process called **inversion**. Thanks to the inversion, it is possible to retrieve the intrinsic properties of the medium ($\boldsymbol{m}$ term in following equations) from data acquired on the field ($\boldsymbol{d}$ term in following equations) (Caterina, 2014).

The objective of the inversion is to minimise the difference between the measured data and the simulated data.

Mathematically, the problem can be written as:

$$d = G(\boldsymbol{m}).$$

where G is commonly used to represent the fundamental physics of the problem.

The forward problem is to find $\boldsymbol{d}$ given $\boldsymbol{m}$. Computing G(**m**) might involve solving an Ordinary (ODE) or Partial (PDE) Differential Equation, evaluating an integral equation or applying an algorithm to **m** for which there is no explicit analytical formulation.

The inverse problem consists in estimating the model parameters $\boldsymbol{m}$ from the observed data $\boldsymbol{d}$.

The inverse problem in ERT consists in reconstructing a model, $\mathbf{m} = [m_1, m_2, \ldots, m_M]$ and the electrical conductivity (σ) is often expressed in its logarithmic form in inverse problem:

$$\boldsymbol{m} = ln(\boldsymbol{\sigma}).$$

Similarly, $\mathbf{d} = [d_1, d_2, \ldots, d_N]$ contains the logarithmic forms of the measured resistances (R):

$$\boldsymbol{d} = ln(R).$$

The inverse problem is solved by numerically minimising the following objective function $\psi(\mathbf{m})$:

$$\Psi(\boldsymbol{m}) = \Psi_d + \lambda\Psi_m.$$

Ψ_d is the measure of the error-weighted data misfit can be computed according to the following equation using L2 norm form:

$$\Psi_d = ||\boldsymbol{W_d}(\boldsymbol{d} - G(\boldsymbol{m}))||_2 = \sum_{i=1}^{N} \frac{\left|d_i - G_{i(\boldsymbol{m})}\right|^2}{|\varepsilon_i|^2}.$$

With $\boldsymbol{W_d} = \text{diag}\left(\frac{1}{\varepsilon_1}, \frac{1}{\varepsilon_2}, \dots, \frac{1}{\varepsilon_N}\right)$ denoting the data weighting matrix, ε_i the individual data errors and λ the regularisation parameter which controls the trade-off between the influence of the data misfit and the model objective function Ψ_m (Binley and Kemna, 2005).

To overcome the ill-posed nature of the inversion problem, an additional constraint is introduced on the model. Typically, a smoothness constraint is applied, encouraging solutions with minimal spatial variability and resulting in a model with the minimum roughness.

$$\Psi_m = ||\boldsymbol{W_m m}||_2$$

$\boldsymbol{W_m}$ typically includes discrete derivative operators to penalize spatial variations (Caterina, 2014).

The problem is nonlinear because the inverse of $\boldsymbol{G}$ does not exist. The inverse model is solved iteratively; it is necessary to start by defining an initial model m_0, usually a homogeneous value.

After each iteration, the model is updated:

$$\boldsymbol{m_{k+1}} = \boldsymbol{m^k} + \Delta \boldsymbol{m^k}.$$

Where $\Delta\boldsymbol{m^k}$ is obtained after the resolution of a linear system using the Jacobian matrix (containing partial derivatives):

$$J_{ij} = \frac{\partial G_i(\boldsymbol{m})}{\partial \boldsymbol{m}_j}.$$

The Jacobian is used to evaluate the sensibility of each cell of the model. It is essential for updating the model iteratively.

Here is the linear system:

$$\left(\boldsymbol{J^T W_d^T W_d J} + \lambda \boldsymbol{W_m^T W_m}\right)\Delta\boldsymbol{m} = \boldsymbol{J^T W_d^T W_d}\left(\boldsymbol{d} - G(\boldsymbol{m_k})\right).$$

The quality of the obtained solution depends on the subsurface data coverage, the choice of regularisation and the characteristics of the noise.

The process of inversion is stopped when the RMS (Root Mean Square) value of error-weighted reaches the suitable value.

$$\text{RMS} = \sqrt{\frac{1}{N}\sum_{i=1}^{N}\left(d_i^{\text{obs}} - d_i^{\text{sim}}\right)^2}$$

Where N is the number of data, d^{obs} the measured data and d^{sim} the data simulated by the inversion.

The RRMS (Relative Root Mean Square Error) is also calculated for each iteration of the inversion. It is the value more often use because it normalises the misfit, making it easier to compare across datasets.

$$\mathrm{RRMS} = \sqrt{\frac{1}{N}\sum_{i=1}^{N}\left(\frac{d_i^{\mathrm{obs}} - d_i^{\mathrm{sim}}}{d_i^{\mathrm{obs}}}\right)^2}$$

In the context of geophysical inversions, the χ^2 (chi^2) value is also used to assess the quality of the fit between the measured and calculated data, with a value close to 1 generally indicating a satisfactory fit given the level of measurement uncertainty.

5.1.2. Depth of investigation (DOI)

The depth of investigation DOI is defined as the depth below which the model parameters are not constrained by the surface data anymore. The advantage of using DOI is that it does not depend on the linearisation assumption for non-linear problem.

Let m_{ref1} and m_{ref2} represent two different homogeneous reference models. The model parameters $m_{\mathrm{ref1}}(x, z)$ and $m_{\mathrm{ref2}}(x, z)$ are obtained using m_{ref1} and m_{ref2} as reference models, respectively. If (x, z) are the coordinates of one cell, then the DOI index for every cell can be calculated as follows:

$$DOI(x,z) = \frac{m_{\mathrm{ref1}}(x,z) - m_{\mathrm{ref2}}(x,z)}{m_{\mathrm{ref1}} - m_{\mathrm{ref2}}}.$$

The DOI index is typically used in its normalised form, DOI_{norm}, by dividing the index vector by its maximum value DOI_{max}:

$$DOI_{\mathrm{norm}} = \frac{DOI}{DOI_{\mathrm{max}}}.$$

Indexes approaching zero imply that both inversions produce the same electrical structures, meaning the inverted model remains constrained by the surface data. Conversely, a DOI approaching one indicates that the reference model increasingly influences the resulting image, meaning the model parameters are less constrained by the surface data (Caterina, 2014).

The DOI for one profile was calculated but is inconclusive due to the highly conductive nature of the deeper layers. Under these conditions, DOI interpretation proves does not allow for a reliable determination of the true depth of investigation of the ERT measurements. Instead, cumulative sensitivity will be represented by a white dashed line on the inversion results. This is a key tool for understanding data coverage and the level of confidence that can be placed in the ERT inversion results. Sensitivity is generally higher near the surface and in the centre of the profile. It decreases rapidly with depth and towards the sides of the section, due to insufficient data coverage in these areas (Caterina et al., 2014).

5.2. Isotropic ERT Inversion

In practice, the inversion is performed using the open-source Python library PyGIMLi[3] on the remaining data. All the inversion are done assuming a relative error of 4% and an absolute error of 10^{-4} Ω·m. A low relative error is essential to ensure that the data simulated through inversion are consistent with the field measurements. These values were chosen arbitrarily but were verified using the resistance error model for one profile, after removing data points with a reciprocal error greater than 5% (Figure 26).

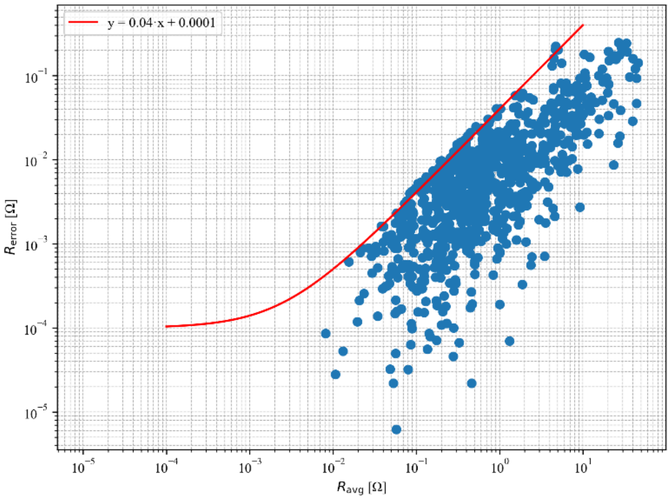

Figure 26: Multi bin power-law resistance error plot

The regularisation parameter (λ) also must be fixed. The larger the value of λ, the greater the emphasis on model smoothness. Conversely, the smaller the λ, the more priority is given to fitting the data closely, even if this results in a noisier model. For all inversions, λ is set to 5 to control the trade-off between data misfit and model smoothness.

The choice of the inversion norm must also be made. There is the robust inversion, which seeks to find a model minimising the absolute values of the data-model residuals (L1 norm) and the regularised inversion, which aims for a smoother model by minimising the squares of the residuals (L2 norm) (Dahlin & Zhou, 2004). For the inversions performed here, the L2 norm will be used to avoid over-constraining the model and potentially hindering its flexibility, even though it is more sensitive to outliers.

If the resulting RRMS error exceeds 10%, data points with high relative error are removed, as this indicates that the difference between the measured and simulated data is too significant.

For the isotropic inversions, the starting model is the median of the data for each profile.

The final number of measurements in Table 2 is the number of data used for all the inversions in the following Sections.

---

[3] Developed by Jens Rücker, Florian Rücker and Thomas Günther, Open-source project available on https://www.pygimli.org.

Table 2: Summary of relevant information for each ERT profile

Profiles	Initial number of measurements	Number of measurements after the threshold of 5% of the repetition error	Final number of measurements	χ^2	RRMS [%]
R1	3076	2922	2839	1.14	4.3
R3	5105	4622	3725	1.36	5.79
R9	5025	4803	3414	1.3	4.53
R4-5	5428	5428	5140	1.27	4.61
R6	3110	2905	2642	1.28	5.58
R7	5504	5328	4877	1.46	4.81
R8	18297	17543	15201	2.58	6.37
R10	8508	8250	7880	1.46	4.78
R11	8473	8295	7520	2.49	6.25
P7	8291	8269	8269	0.81	3.81
P8	8636	8133	8070	0.95	3.87

For profile R9, a large number of data points were removed, as the dataset was noticeably noisier. This was due to two cables being connected incorrectly during data acquisition.

The profiles were divided into three groups: those located near the Tiber River (R1, R3 and R9), those conducted within the ruins of Ostia but farther from the river (R4-5 and R6) and finally, the profiles carried out in the fields surrounding Ostia (R7, R8, R10, R11, P7 and P8). A summary of relevant information for each profile is shown in Table 2.

5.2.1. Profiles near the Tiber

Firstly, the three profiles near the Tiber will be analysed. Figure 27 shows the inversion of profile R1.

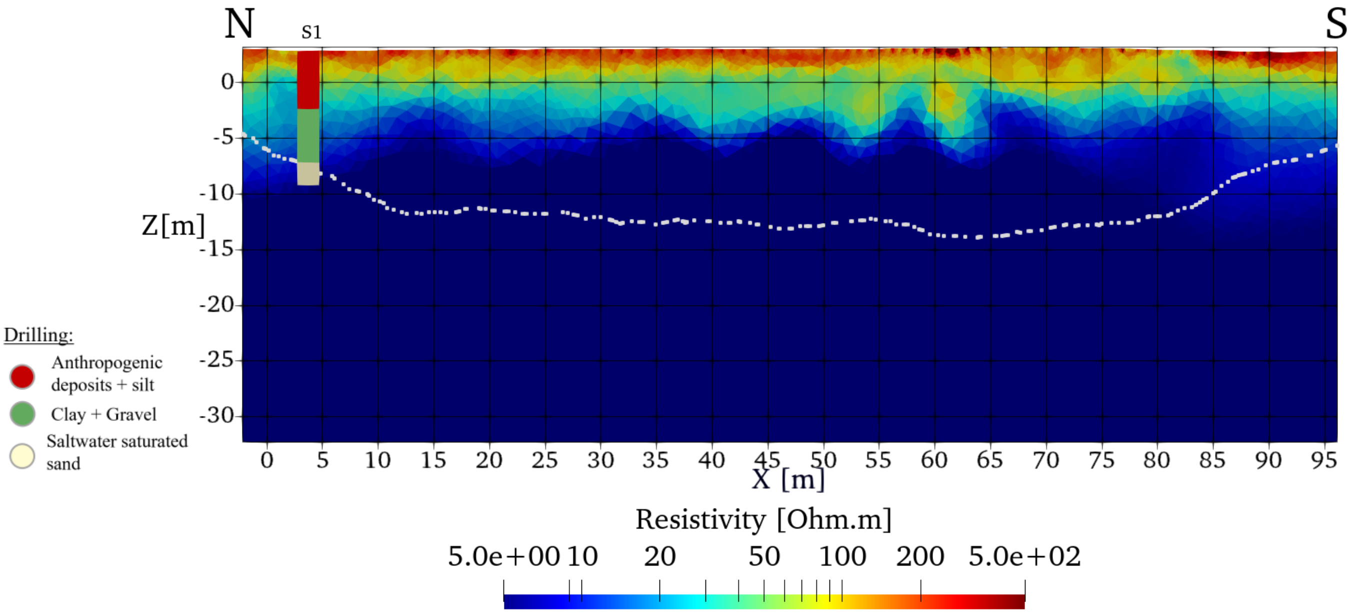

Figure 27: Isotropic inversion of profile R1

The aim of this analysis is to delimit the fluvial and littoral deposits. R1 (Figure 27) and R3 (Figure 28) are similar, they have a homogeneous resistivity zone in the three first meters. Below, the resistivity is lower and characterised by unsaturated and saturated sand and silt (2 to 6 m below sea level). Finally, below 6 m, there are saturated deposits characterised by a resistivity below 10 Ω·m.

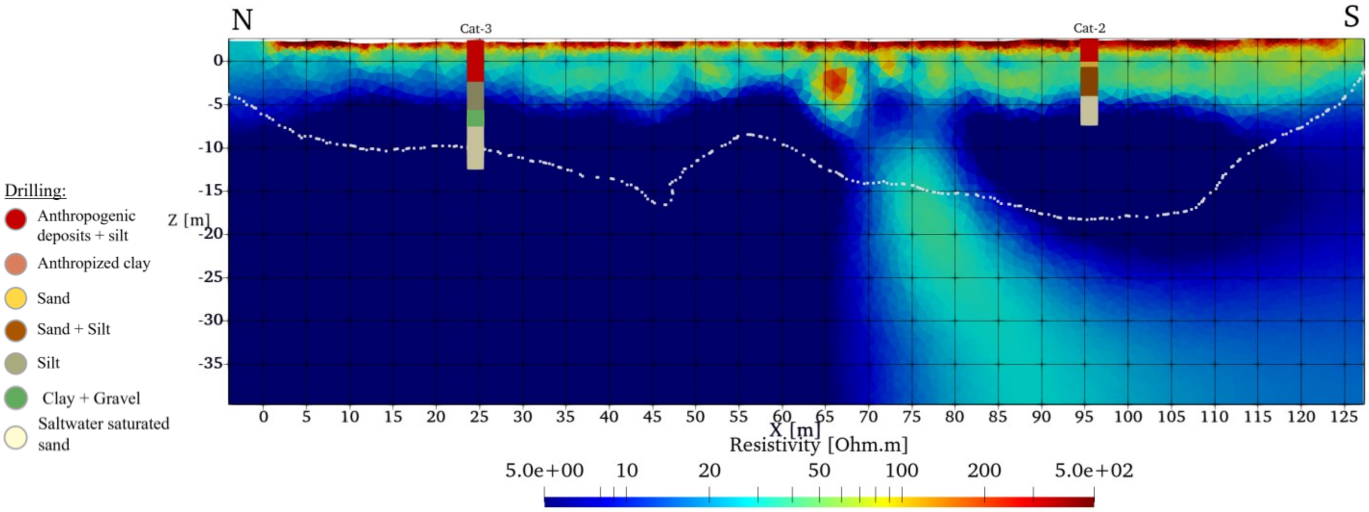

Figure 28: Isotropic inversion of profile R3

The R3 profile is located approximately fifty metres southeast of the Tiber River. Two cores were collected along this profile (Cat-2 and Cat-3). Cat-3 reveals a fluvial depositional environment down to a depth of six metres, whereas Cat-2 shows only deltaic deposits. The R3 profile is thus characterised by fluvial deposits in the northern part and coastal deposits in the southern part. This transition can maybe be located around 75-80 m where there is an anomaly.

It is also important to note that the inversion does not seem able to distinguish between silts and sands beyond 5 m below sea level. This may be due to the presence of saline water, which causes a significant drop in resistivity values.

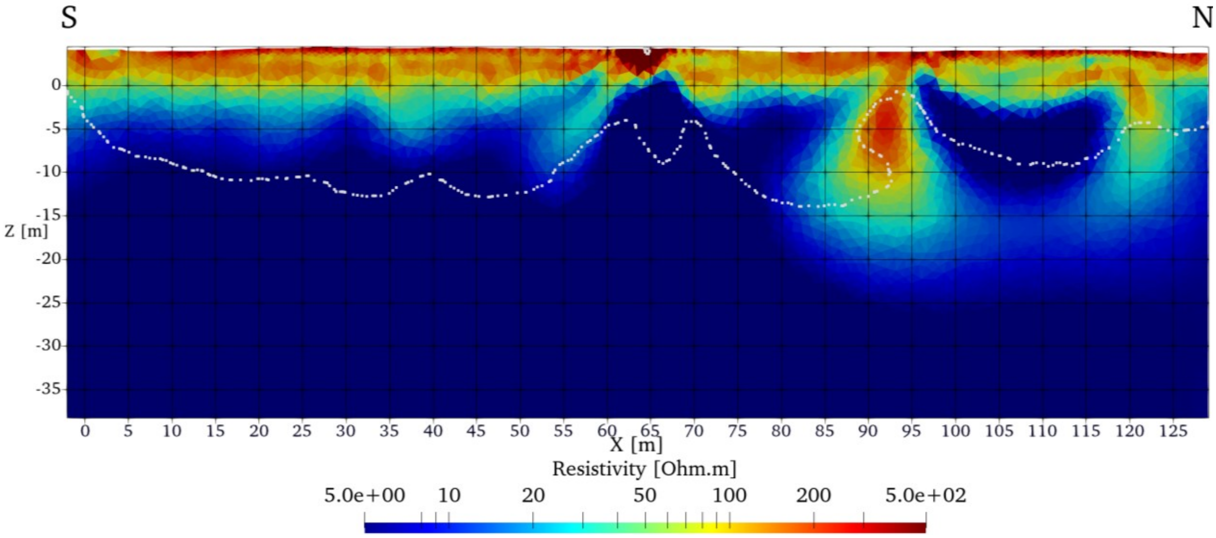

Figure 29: Isotropic inversion of profile R9

Profile R9 (Figure 29) is characterised by a thicker layer of more resistive deposits, with a particularly resistive zone between 60 and 65 m. At the northern end of the profile, two more resistive zones extend with depth. This is likely due to the inversion process, as it corresponds to the area where the cable was incorrectly connected.

5.2.2. *Profiles between the Roman remains of Ostia*

Profiles R4-5 (Figure 30) and R6 (Figure 31) were conducted within the archaeological remains of Ostia. They intersect various structures such as building ruins, gardens and roads.

Profile R4-5 is composed of anthropogenic deposits, more resistive, except at both ends of the profile, in fact roads are less resistive. Beneath this layer lies a more conductive unit, like what was observed in profiles R1 and R3. However, here it appears to extend deeper in the medium part of the profile. The third layer is characterised by very low resistivity values; it seems to be salt-water saturated deposits.

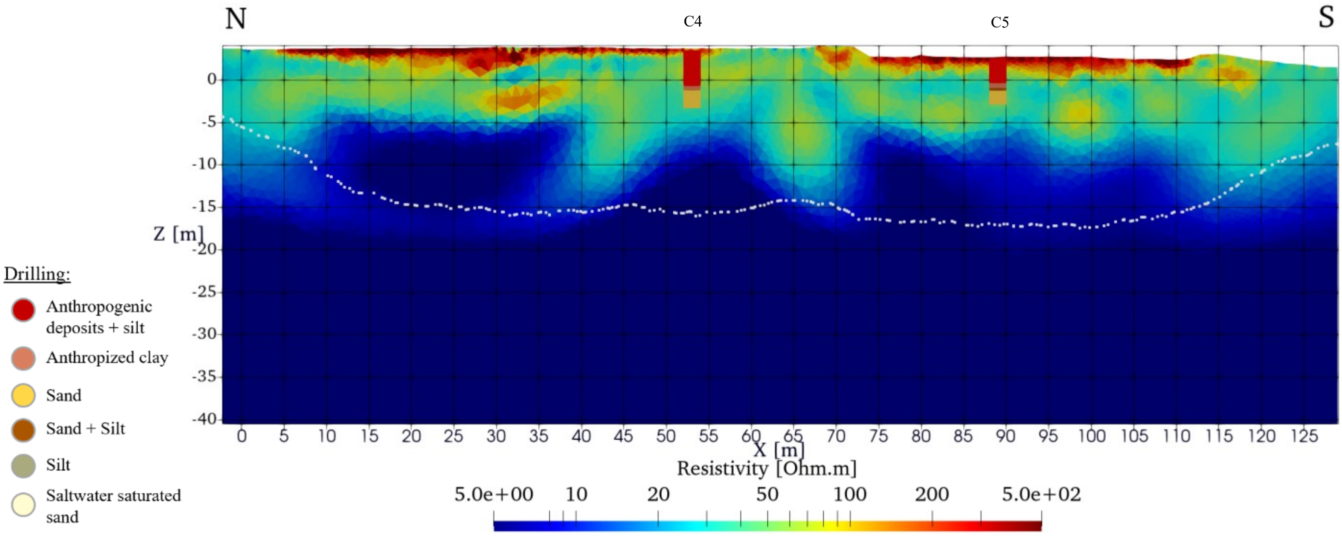

Figure 30: Isotropic inversion of profile R4-5

Cores C4 and C5 were projected onto the profile. Core C4 is located about 3 m from the profile, while Core C5 is about 7 m away.

Profile R4-5 (Figure 30) is expected to show an alternation of beach ridges and inter-ridge depressions (swales). Beach ridges are relict landforms. They are semi-parallel to the shoreline and were built by the action of waves and wind. Their origin lies in the intertidal and supratidal zones. The inter-ridge depressions (swales) are long and narrow depressions that extend parallel to the coastline. These beach ridges and swales are characteristic of the outer deltaic plain of the Tiber (Juncker et al., unpublished manuscript). The presence of swales beneath Ostia, evidenced by certain boreholes (C4 and C5), indicates the development of wetland zones but in this inversion it difficult to see it.

Profile R6 (Figure 31) has the same structure as profiles R3 and R1, except that the middle layer is thicker. In the centre of the profile (between 35 and 55 m along x-axis), close to the surface, a more conductive zone can be observed. A more resistive anomaly is also identified between 2 and 6 m below the sea level and cannot be explained for now.

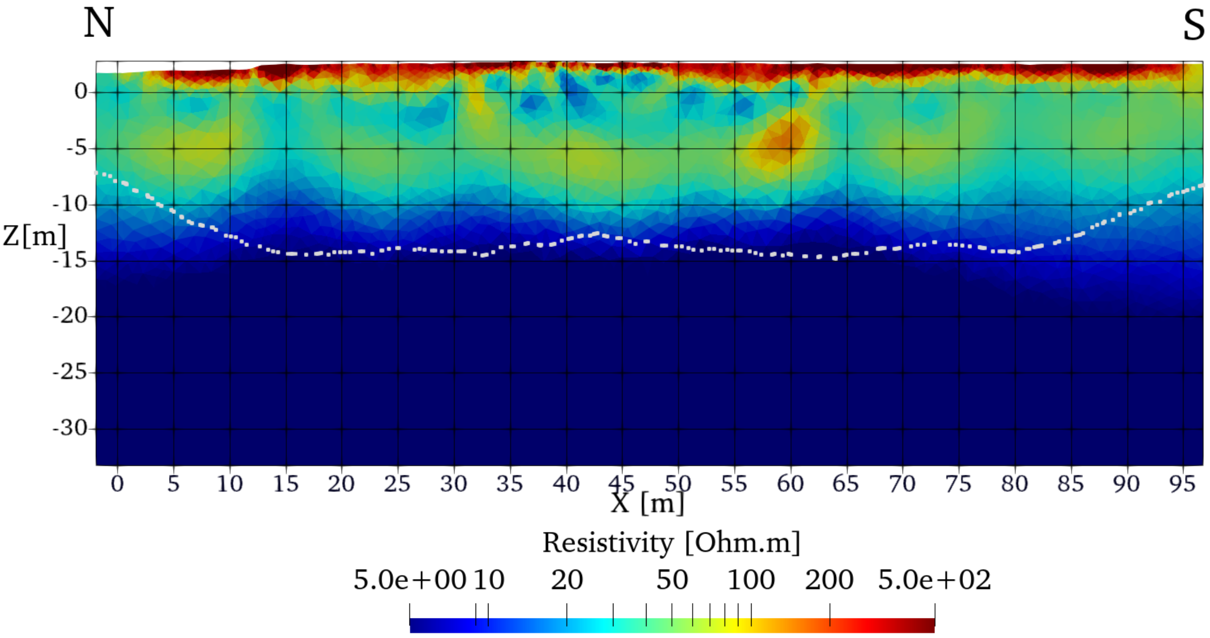

Figure 31: Isotropic inversion of profile R6

5.2.3. Profiles in the field around Otia Antica

Profile R7 (Figure 32) is located to the west of profile R6. Its inversion result differs significantly from what has been observed so far. In this case, the more resistive zone extends below the current sea level in the southern part of the profile. A more resistive anomaly also extends down to a depth of 20 m below current sea level. At this stage, it is difficult to determine whether this feature is an inversion artefact or reflects a real subsurface characteristic of the site.

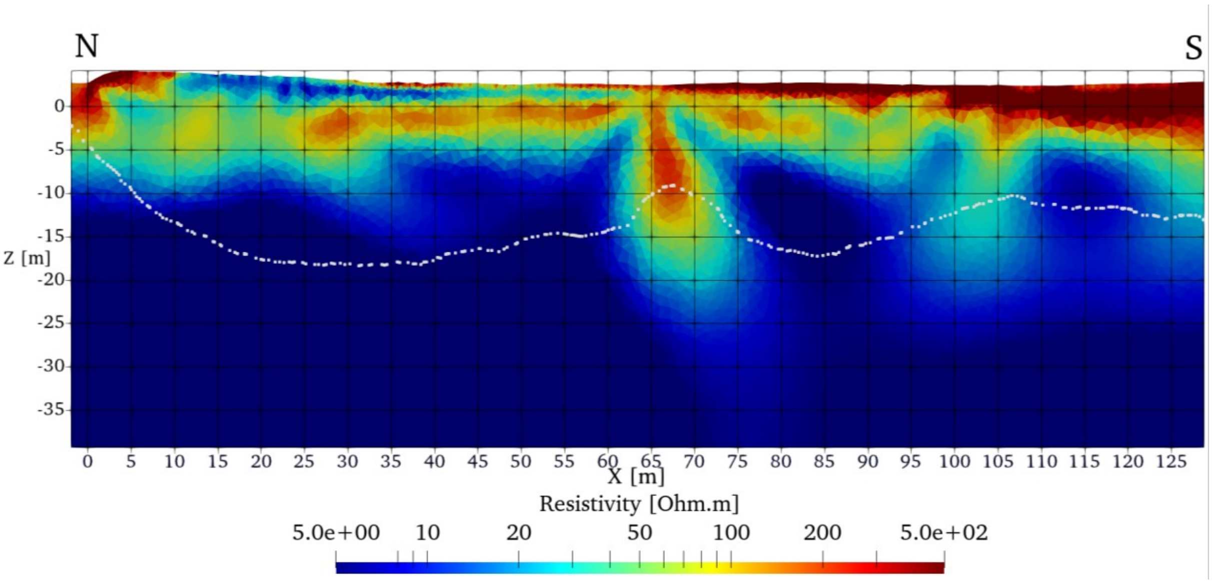

Figure 32: Isotropic inversion of profile R7

The last five profiles were used to investigate the field located to the south of Ostia Antica. Profile R8, the longest one, intersects with three other profiles (R11, R10 and P7). Four cores are also located along this profile. Over the first 10 m, the inversion results of profile R8 (Figure 33) are similar to those obtained previously and correspond well with the core analyses. However, as with profile R7, two more resistive anomalies extend in depth.

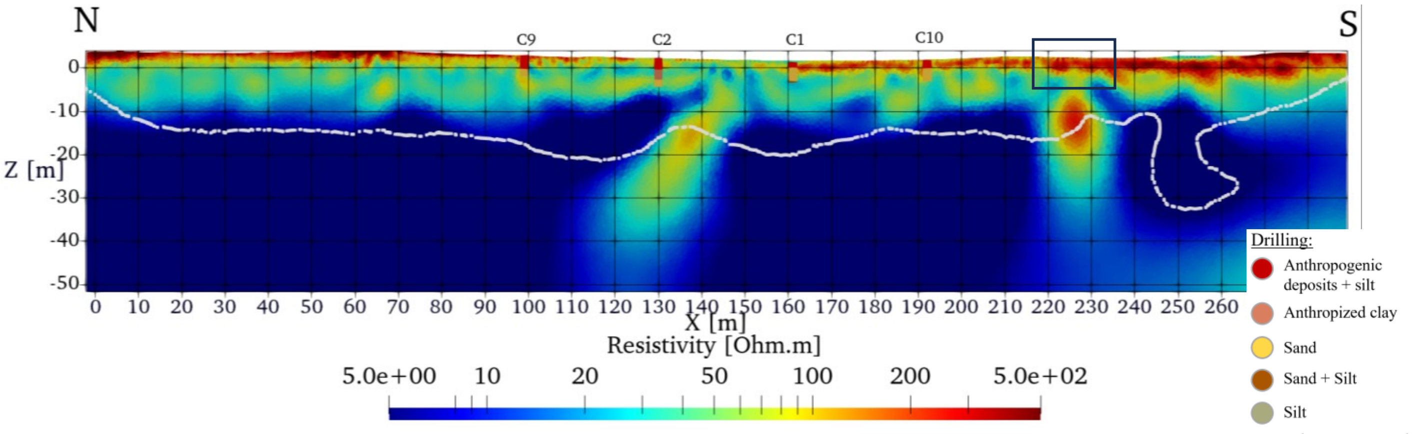

Figure 33: Isotropic inversion of profile R8

Profiles R11 (Figure 34) and R10 (Figure 35) are similar over the top ten meters and both show a more resistive anomaly around 100 m along the x-axis, located approximately 5 m to 10 m below current sea level. These two anomalies are aligned.

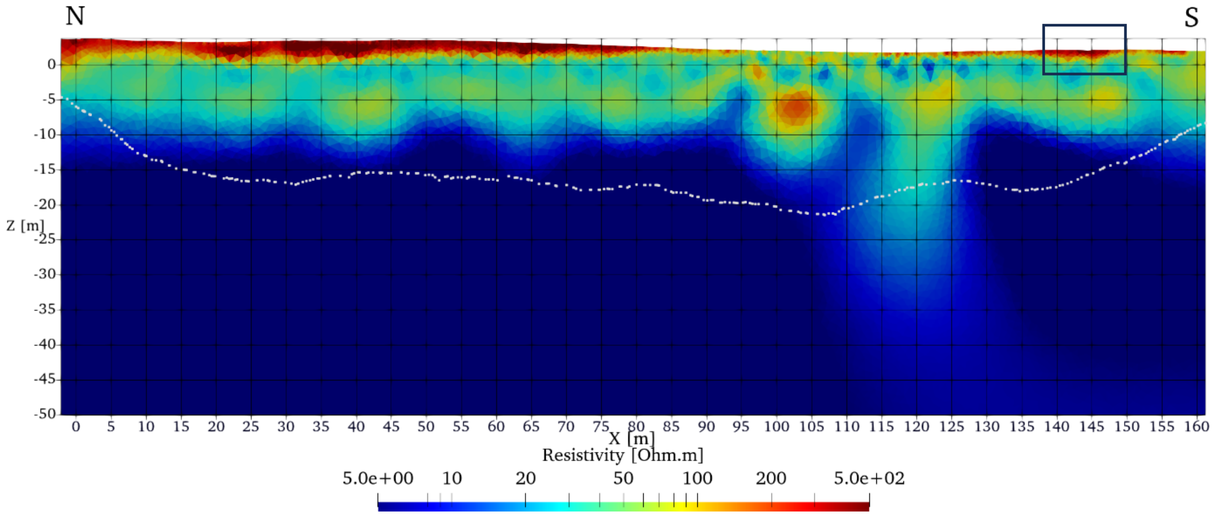

Figure 34: Isotropic inversion of profile R11

Profile R10 intersects with profile R8 at core C2. Analysis of this core revealed a layer of anthropized clay, which corresponds to a more conductive lens in the inversion of profile R10.

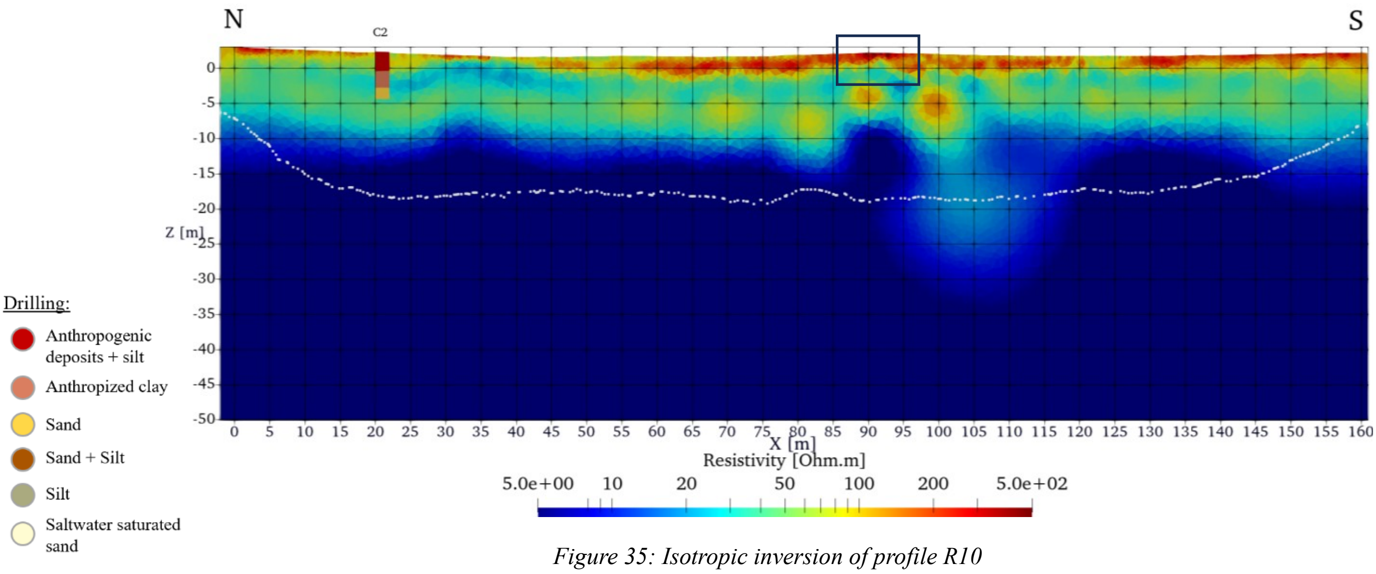

Figure 35: Isotropic inversion of profile R10

Profiles R8, R10 and R11 also intersect the ancient city wall of Ostia Antica highlights by the black rectangle on profiles. It is particularly well visible in the inversion of profile R11, where it appears between 140 m and 150 m along the profile.

The pseudo-sections of profiles R7 and R8, shown in the Annexe 9.2, display slightly higher apparent resistivities at the locations of the identified anomalies, although the contrast with the surrounding measurements is less pronounced.

In May 2025, profiles P8 (Figure 36) and P7 (Figure 37) were carried out. Their inversion results are similar to those of profiles R10 and R11. Profile P8 also show a more resistive anomaly at depth, between 5 m and 10 m below the sea level. This anomaly appears less resistive than those observed in profiles R10 and R11, but the measurements were not taken at the same time. Such variations could be due to differing environmental or measurement conditions.

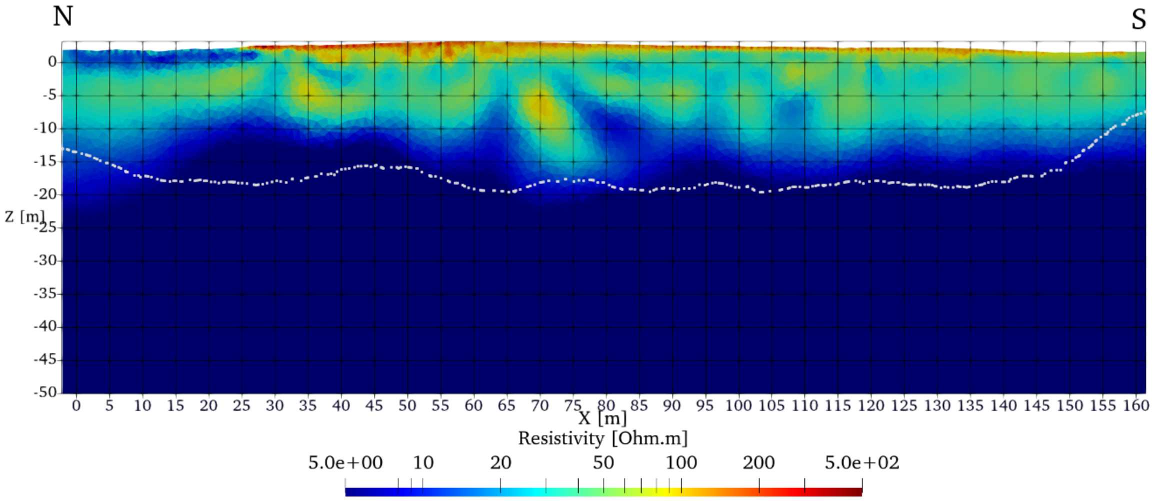

Figure 36: Isotropic inversion of profile P8

Profile P7 intersects with core S2 and its inversion aligns with the analysis of this core. The southern part of P8 is also more resistive at the surface, which is expected as it corresponds to a known anthropized area.

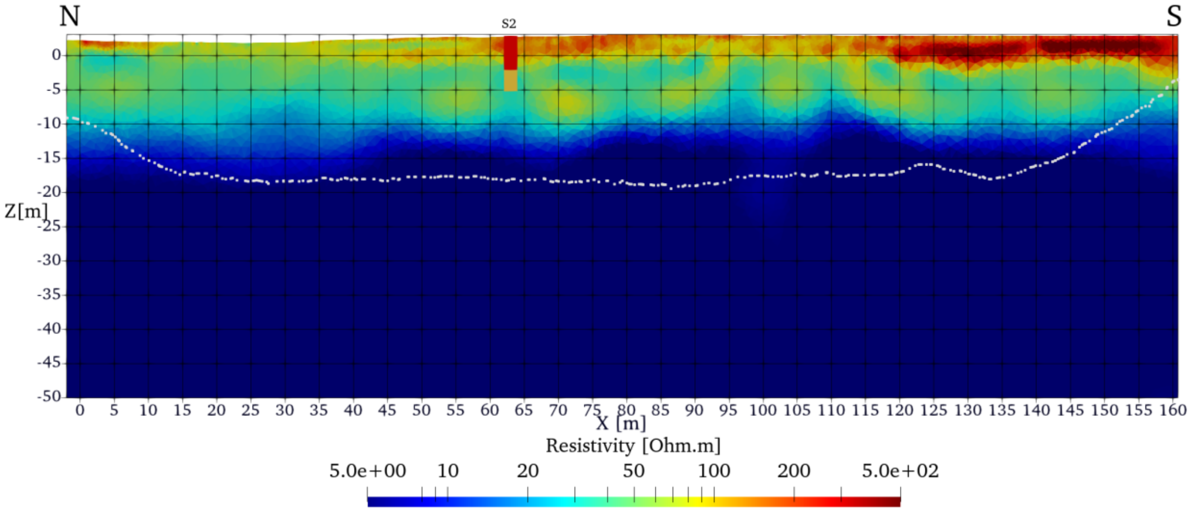

Figure 37: Isotropic inversion of profile P7

Finally, in general, each inversion can be divided into three zones. The first zone concerns the upper part of the inversion and is characterised by high resistivity values. It represents the archaeosphere. The second zone is characterised by lower resistivity values correspond to sandy formations from the Tiber channel. Finally, the last and deepest zone is characterised by very low resistivity values approximately and corresponds to a saltwater-saturated deposits.

However, at depth, some anomalies are visible, raising the question of whether they are caused by the inversion process or not. To investigate this, forward modelling followed by constrained inversions will be performed on some profiles.

A more detailed and in-depth interpretation of the archaeosphere is also presented in Section 5.6.

5.3. Forward modelling

To ensure that the anomalies exist and are not numerical artifacts, some profiles will first be modelled by direct modelling. Each profile will be drawn by distinguishing different zones: an anthropogenic zone over the first 2 or 3 m, a less resistive zone corresponding to the sand and finally a zone of very low resistivity at depth corresponding to the saltwater-saturated zone. The anomalies are represented and a higher resistivity than their environment is imposed. These modelling are done without topography.

Profiles R8, R11 and R10 will be analysed. Profile R7 could also be included in the analysis.

Table 3: Legend for direct modelling

	🟥	🟫	🟦	🟥	🟪
Categories	Anthropogenic deposits	Sand	Saturated salt water	Anomaly 1	Anomaly 2
Resistivity [Ω·m]	300	50	10	150	60

In this Section, the inverted data do not originate from field measurements, but from synthetic data generated through forward modelling. For each region of the forward modelling, a value of resistivity is associated (Table 3). The inversions are then compared to the results of the classical isotropic inversion of Section 5.2.

In Figure 38a, the modelized of the profile R8 is represented, in this profile, the less resistive anomaly, represented in purple is not visible in profile R10. It is therefore important to know if it is real or due to the inversion.

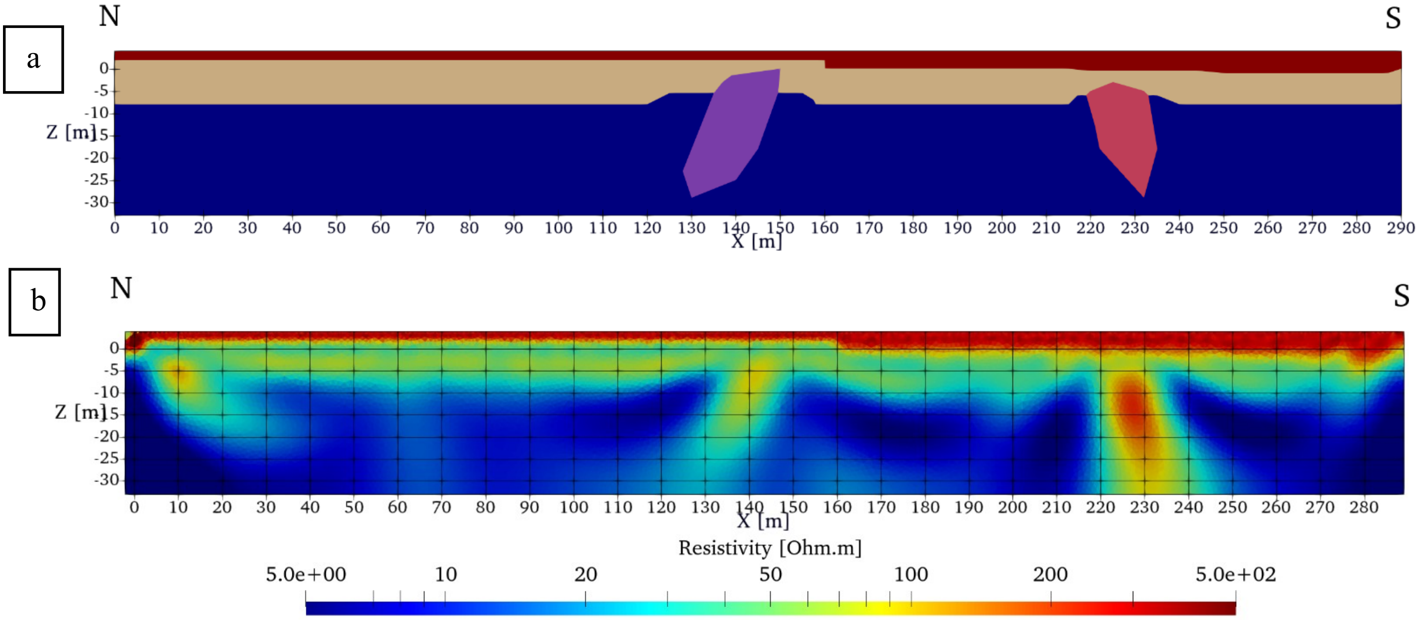

Figure 38: (a) Forward modelling, (b) Inversion of synthetic data generated through forward modelling (profile R8)

The inversion represented in converges after 7 iterations and its RRMS is equal to 4.03% (Figure 38b).

The inversion of profile R8 looks like a smoother version of the isotropic inversion but shows an anomaly in the north that was not previously present, which is most likely due to the inversion process. Both anomalies remain visible. The anthropogenic zone is highly resistive and does not show significant variation compared to the isotropic inversion; it also appears more extensive, which can be explained by the absence of topography in this model. The deepest zone appears slightly more resistive.

R11 is modelled in Figure 39a and R10 is modelled in Figure 40a. The more resistive anomalies on both profiles are aligned.

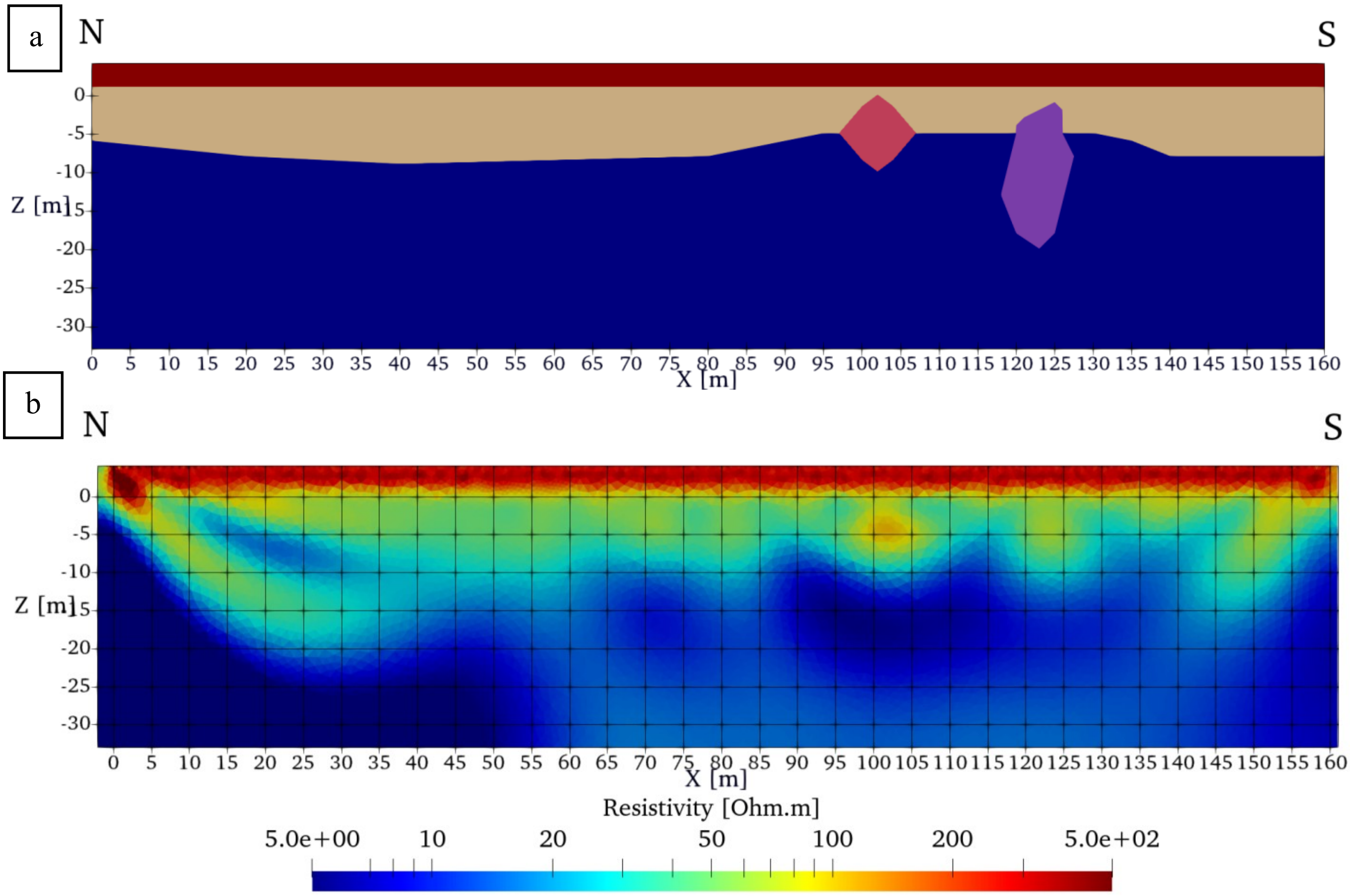

Figure 39: (a) Forward modelling R11, (b) Inversion of synthetic data generated through forward modelling (profile R11)

The inversion of profile R11 converges after 8 iterations and its RRMS is equal to 4.28% (Figure 39b).

The inversion also appears as a smoother version of the isotropic inversion for profile R11. Additionally, the more resistive anomaly still appears but is characterised by slightly lower resistivity values (100–120 Ω·m) and is slightly smaller. The less resistive artefact does not extend as deeply as it does in the classic isotropic inversion. This deeper extent may therefore be an artefact of the inversion process itself. As observed for profile R8, both the anthropogenic zone and the saltwater-saturated zone exhibit higher resistivity values in the inversion based on forward modelling compared to the classical isotropic inversion.

The inversion of profile R10 converges after 12 iterations and its RRMS is equal to 4.57% (Figure 40b).

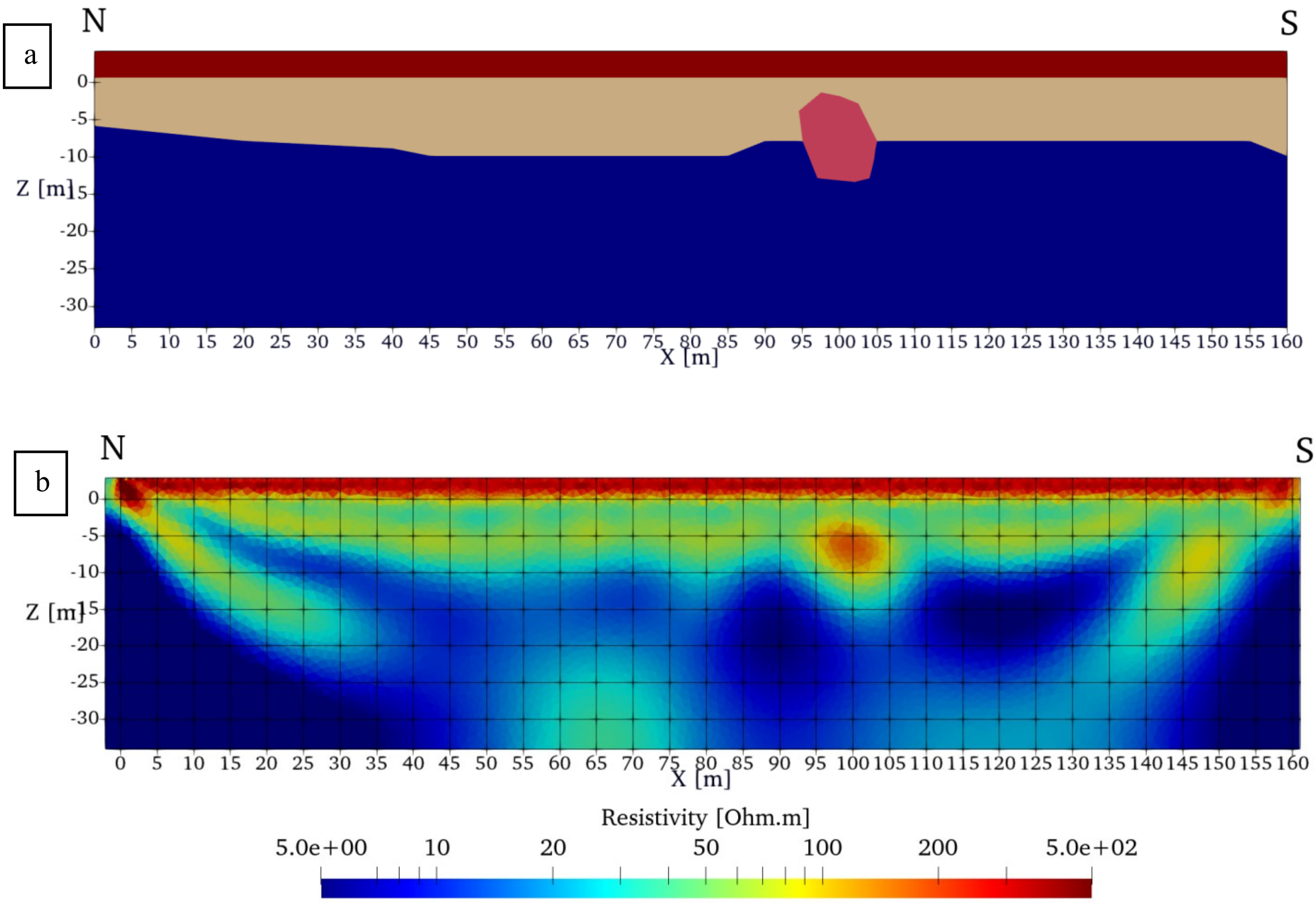

Figure 40: (a) Forward modelling, (b) Inversion of synthetic data generated through forward modelling (profile R10)

In this inversion, there are artefacts due to inversions in the bottom. Over the first 10 metres, the inversion is very similar to that of profile R11. The anomaly is still present and aligned with the one observed in profile R11, but it is slightly more resistive (150–170 Ω·m).

In conclusion, the forward modelling still reveals deep anomalies and shows the same boundaries for the three zones identified in the isotropic inversion, even though the resistivity values are not the same. These resistivity values depend on the values assigned to each region prior to the data simulation. By changing these values, the inversion outcome could be different, the resistivity values attributed to saltwater-saturated zone is maybe too high.

5.4. Inversions constraint by drilling and Direct Push

After attempting to model the anomalies, the objective is to constrain the inversions using the analysis of cores and DP-EC logs. In the first phase, the DPs will be used to test a geostatistical method, while the cores will be employed to perform a structurally constrained inversion.

5.4.1. Geostatistical method

The DPs are used to construct a variogram, which serves as a basis for performing an inversion with geostatistical constraints. This allows us to assess whether this type of inversion is relevant and effective in this context.

A semi-variogram is a fundamental tool in geostatistics to analyse the spatial distribution of a propriety. In this case, it is used to study the distribution of the conductivity on depth. The semi-variogram is used to quantify the spatial correlation.

This formula expresses the spatial variability between two points separated by a distance h:

$$\gamma(h) = \frac{1}{2}\big(Z(x) - Z(x+h)\big)^2.$$

This expression is calculated for many pairs of points located at the same distance h and then averaged to obtain a more reliable estimate of the spatial variability at that distance. For this variogram, 15 classes were defined, meaning that spatial variability was calculated for 15 different distances h. The variogram is represented using the package Geone[4] in Python in Figure 41.

If $\gamma(h)$ is high, the correlation at this specific h is weak.

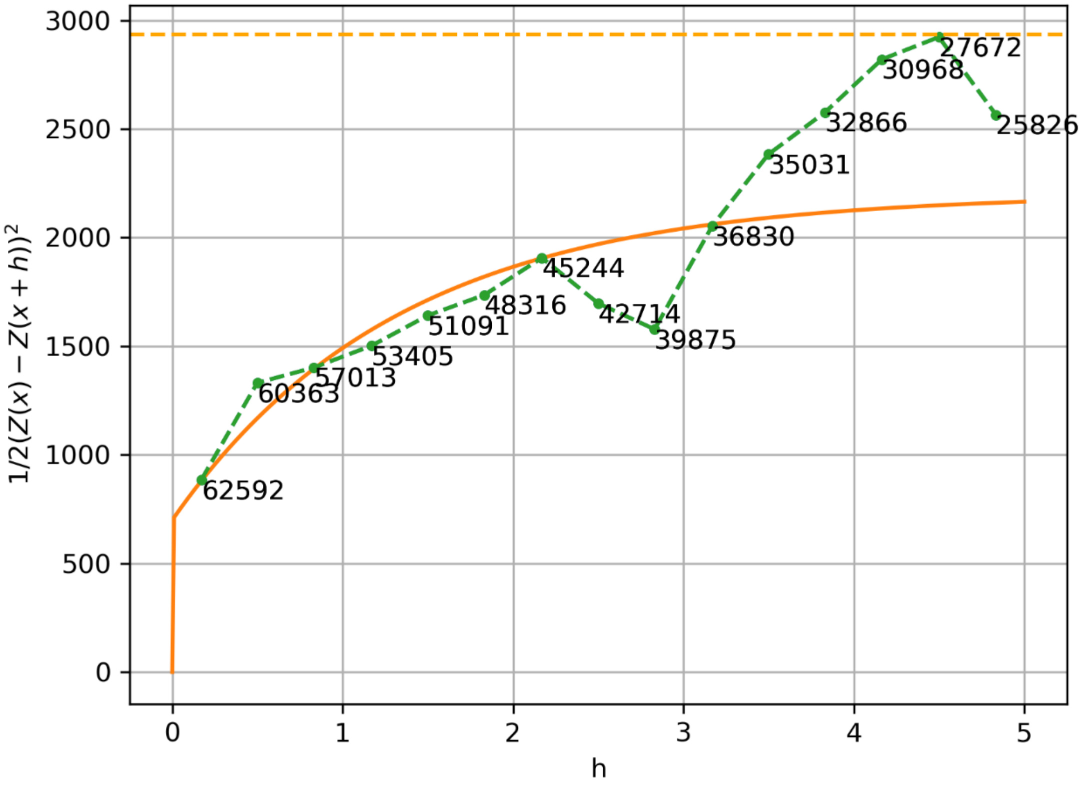

Figure 41: Experimental variogram done with Geone

The experimental variogram realised with an exponential model. A nuggets effect of 800 and a range of 3 m are fixed to fit the data.

The mean of the data, represented by the orange dashed line, is relatively high, which indicates that conductivity values can vary significantly even between two very closely spaced points. In theory, the experimental variogram should asymptotically approach this mean. However, in this case, doing so would result in a poorer fit for the initial points, which are the most important. Therefore, this variogram was chosen to best fit the most strongly correlated points.

---

[4] Renard, P., & Straubhaar, J. (2024). *geone: Geostatistical Python package* [Python package]. GitHub. https://github.com/randlab/geone

The inversion was done on the first twenty meter with a coefficient of anisotropy of 0.6 and a correlation length of 3 m fixed thanks to the range of the variogram. The range defines the maximum distance of correlation. Beyond this distance, the points are considered statistically independent. The result of the inversion is shown in Figure 42.

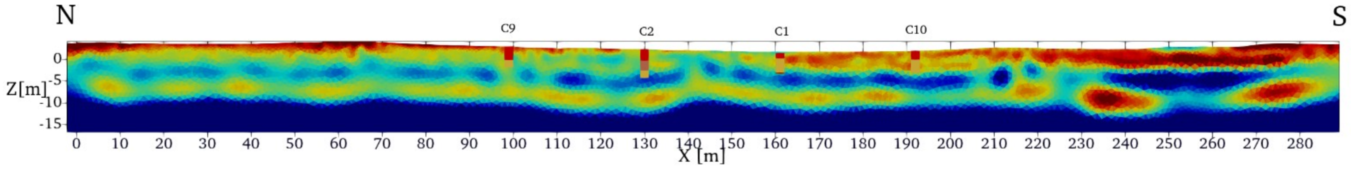

Figure 42: Inversion of profile R8 with geostatistical method

The inversion converges after 8 iterations with a final RRMS of 8.7% and a χ^2 of 2.44.

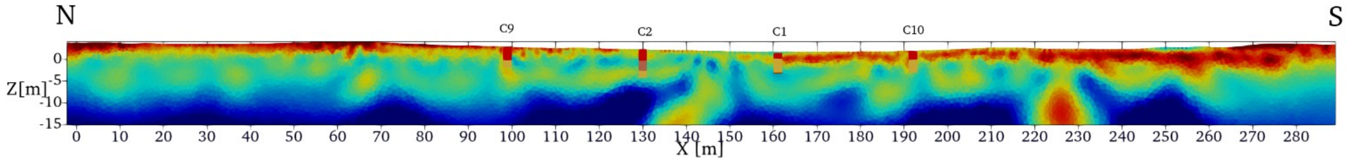

Figure 43: Isotropic inversion of profile R8 on the first twenty meters

By examining the inversion results (Figure 42), the anthropized zone, very resistive and shallow, appears similar to that obtained with the isotropic inversion (Figure 43). From about 10 m below sea level, a highly conductive zone is also observed, likely corresponding to deposits saturated with saline water. However, the intermediate region between these two layers shows notable differences: a less resistive lens is visible at approximately 5 m depth, which was not apparent in the isotropic inversion.

Moreover, the two previously identified anomalies do not seem to extend at depth. In fact, the comparison of the inversions highlights that the resistive anomaly observed in the southern part of the profile, between approximately 220 and 240 m on the isotropic inversion (Figure 43) and extending in depth from about 5 to 15 m below current sea level, is also present on the constrained inversion (Figure 42), but in a different form. Indeed, applying this constraint has the effect of smoothing vertical and horizontal variations over short distances. The anomaly therefore appears shallower and more "flattened," as if it had been shifted upward. The anomaly further north, located between 130 and 150 m on the isotropic inversion, is also more flattened and less deep.

The imposed correlation length represents a strong constraint that significantly affects the rendering of deeper anomalies. Based on these results, two conclusions can be drawn: either the artifacts do not actually extend at depth and are a result of the inversion method used or the geostatistical inversion is too restrictive and fails to accurately reproduce subsurface features at greater depths. A better option would be to impose a variable correlation length depending on the different zones of the studied environment.

5.4.2. Structural constraint inversion

In R8, four cores are located, and structural information can provide valuable information about geological boundaries in the subsurface. It is therefore possible to define a boundary for the archaeosphere near cores C1 and C10. To do so, a boundary is drawn between the anthropogenic deposits and the sandy deposits (dotted white line in Figure 44).

The inversion shown in Figure 44 was done on the first twenty meter with a coefficient of anisotropy of 0.6 as with the geostatistical method. The inversion converges after 8 iterations with a final RRMS of 6.5% and a χ^2 of 2.64.

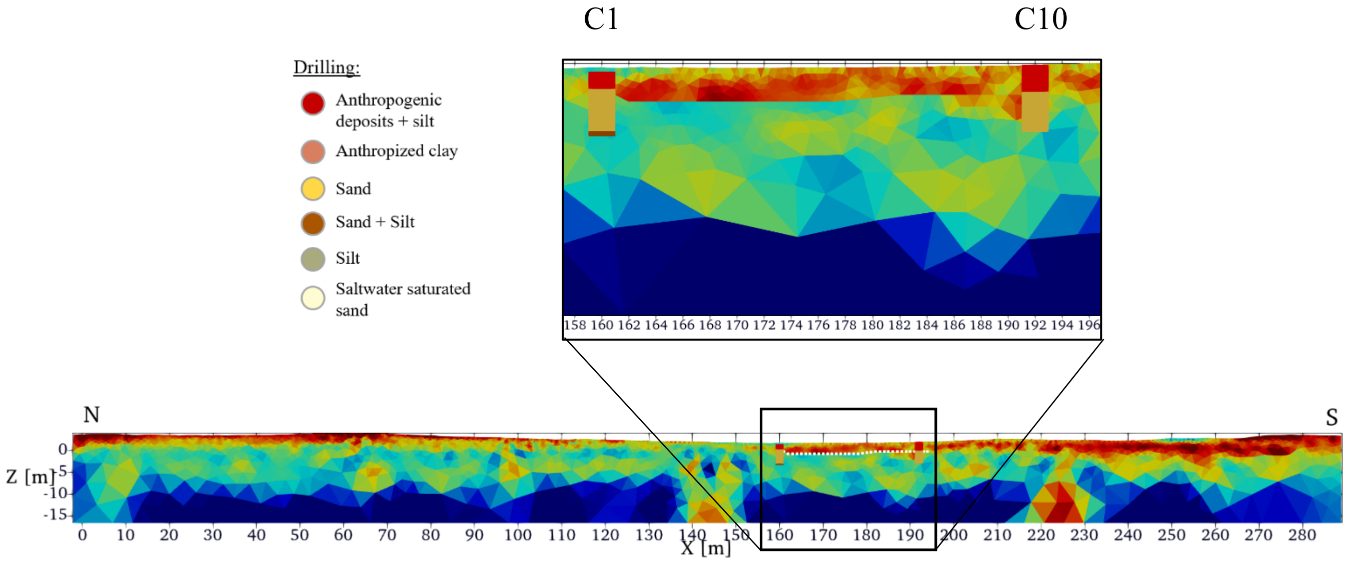

Figure 44: Structural constraint inversion of profile R8

As the cores are spaced 30 m apart and the profile is 288 m long, the influence of this boundary on the entire profile is minimal but still noticeable between the two cores. In fact, the limit between the anthropogenic deposits and the sandy deposits is clearer. Therefore, this method strongly restricts inversion. It would be interesting to apply this type of inversion to other profiles once other cores have been taken and analysed.

5.4.3. Comparison

Both inversions were constrained, but in different ways. In the inversion of Section 5.4.1, the constraint was applied over the entire mesh, whereas in the inversion of Section 5.4.2, the model was constrained only over a shallow and limited portion. In the second case, artifacts appear to extend to greater depths compared to the inversion constrained using geostatistical methods. Since the anisotropy factor was imposed in both inversions, it is the correlation length that effectively prevents the downward propagation of anomalies.

5.5. Probabilistic approach

The non-uniqueness of the solution to inverse problems in geophysics can lead to interpretation errors when characterising the subsurface. To avoid these, ‘ground truth’ independent information, such as that obtained from boreholes, can be used to improve, calibrate and interpret the inverted models. The objective is to provide a quantitative interpretation of inverted geophysical data, based on probability theory and focused on solving a classification problem. To do this, Isunza Manrique et al., 2023 propose two approaches, including a probabilistic approach.

The probabilistic method is based on **Bayes rule** and the principle of the permanence of ratios to calculate the joint conditional probabilities of different chosen categories. The goal is to obtain the P(A|B,D) where A is the category we want to classify from geophysics, B is the (inverted) resistivity values and D is the investigation depth. The aim of this is to transform a tomography into a classified image. To compute the joint probabilities in the presence of interdependence between B and D which is the case here, the approach of Journel (2002) called the principle of permanence of ratios is used, where the following metrics a, b, d, X measure the prior uncertainty and takes the value 0 if the probability is 1 (no uncertainty) and goes to the infinity is the probability is 0 (impossible event) (Isunza Manrique et al., 2023).

For the classification, the first step is an estimation of the **a priori** probabilities for each category, based on the proportions observed in the borehole data and the DP data form (Hadler et al., 2020).

The following equation corresponds to the ratio of the prior probabilities:

$$a = \frac{1 - P(A)}{P(A)} = \frac{P(\tilde{A})}{P(A)}.$$

P(A) represents the prior probability that event A occurs, while $P(\tilde{A})$ denotes the probability of the opposite event occurring.

Then, the distributions of the variables (such as resistivity ρ and investigation depth z) are determined for each category from the training data, using a Gaussian model (Isunza Manrique et al., 2023).

The conditional probabilities for each variable and category are then calculated using **Bayes rule**. These probabilities are combined with the **a priori** probabilities through the principle of the permanence of ratios to obtain the joint conditional probabilities. These are then normalised so that their sum equals 1 at each point of the model (Isunza Manrique et al., 2023).

The parameters b and d of the following equations represent the ratio of conditional probabilities after observing either B or D, respectively:

$$b = \frac{P(\tilde{A}|B)}{P(A|B)} \; and \; d = \frac{P(\tilde{A}|D)}{P(A|D)}.$$

Finally, X expresses the ratio of the conditional probabilities after both B and D have been observed:

$$X = \frac{P(\tilde{A} \mid B, D)}{P(A \mid B, D)}.$$

The ratio $\frac{d}{a}$ quantifies how the observation D affects the initial belief in event A. It can be called the ‘D contribution’:

$$\frac{d}{a} = \frac{P(\tilde{A} \mid D)}{P(A \mid D)} \cdot \frac{P(A)}{P(\tilde{A})}.$$

It is assumed that this influence remains valid even when an additional observation B is introduced. This means that the contribution of D to the probability of A remains the same before and after taking B into account.

$$\frac{X}{b} = \frac{d}{a}$$

As a result, one can derive a formula for the updated probability, which simplifies calculations since it only requires knowledge of P(A), P(A|B) and P(A|D):

$$P(A \mid B, D) = \frac{1}{1 + X} = \frac{a}{a + b \cdot d}.$$

In the application presented here, multiple categories are considered. Thus, the conditional probabilities must be computed for each category:

$$P(A_i \mid B) = \frac{P(B \mid A_i) \cdot P(A_i)}{P(B)}.$$

To estimate these probabilities, we analyse how resistivity values are distributed across known categories, based on reference points such as boreholes and DP-EC logs. These distributions are approximated using Gaussian functions. The same approach is applied to elevation data.

As explained in Section 4.2.3 six categories were defined, and each category has a probability to appear (Table 4). The determination of prior probabilities is crucial, as it significantly influences the outcome of the classification.

Table 4: Prior probabilities for the ERT inversion classification

Category	Description	Probability
1	Anthropogenic deposits + Silt	0.31
2	Anthropized clay	0.021
3	Sand	0.145
4	Silt + Sand	0.12
5	Silt	0.195
6	Saltwater-saturated sand	0.209

The sum of these 6 probabilities is equal to 1.

In this case, it is important to note that DP logs go deeper than the cores but are fewer in number. As a result, the percentage of Categories 4, 5 and 6 is higher in the DPs than in the drilling whereas the percentage of Categories 1, 2 and 3 are higher in drilling than in DPs. Therefore, the final percentages are biased because they are calculated by adding the length of each category and dividing it by the total length of drilling and DP. There are approximately 95 m of cores and 76 m of DPs.

After that, the parameters of the PDFs must be determined. They describe how the geophysical data behave for each known category and are used as the likelihood in Bayes theorem to update prior uncertainties into posterior probabilities (Isunza Manrique et al., 2023). They are therefore essential.

Since the DP tests have been digitised, there are more measurement points and therefore more resistivity values per meter compared to the cores, where resistivity values were assigned to a category based on the core's location within the inversion mesh.

This leads to two options based on Table 5:

- Retain the entire dataset (classification 1)
- Reduce the number of data points from the DP logs by averaging resistivities of each DP log each 0.01 m (classification 2).

Table 5: Datasets

	Drilling	**Entire DPs dataset**	**Reduce DPs dataset**
number of measurement points	680	12400	3520

Moreover, for classification 1, the elevation of the DP logs was simplified and fixed based on the average height of the profiles equals to 2.65 m, whereas for classification 2, the elevation corresponds to the one measured by Hadler et al., 2020. The purpose of these two classifications is to test the sensitivity of the classification to the prior and the PDF (Probability Density Function). Indeed, since the number of measurement points changes, the parameters (mean and standard deviation) of the Gaussian distributions will vary, which will in turn affect the classification result.

Once the priors have been defined, it is possible to compute the univariate Gaussian distributions for each category for both classifications. The integration of each distribution must be equal to one. It is the case for each distribution except for the distribution of the Category 1 because the scale for the x-axis does not allow the integral to reach 1, but if the axis were extended, the total integration would equal 1.

To illustrate both classifications, profile R4-5 and R8 will be used because boreholes were done on or near these profiles. After that, the best classification will be used for the other interesting profiles.

5.5.1. Classifications

Classification 1

Table 6 represents the resistivity mean and the standard deviation for the Gaussian PDF’s when the entire dataset is used. The PDF of each category is represented in Figure 45.

Table 6: Resistivity mean (μ) and standard deviation (σ) (Classification 1)

Category	Description	μ [Ω.m]	σ [Ω.m]
1	Anthropogenic deposits + Silt	117.7	185.49
2	Anthropized clay	47.77	9.68
3	Sand	49.91	27.84
4	Silt + Sand	20.25	12.03
5	Silt	10.51	3.52
6	Saltwater-saturated sand	4.46	3.61

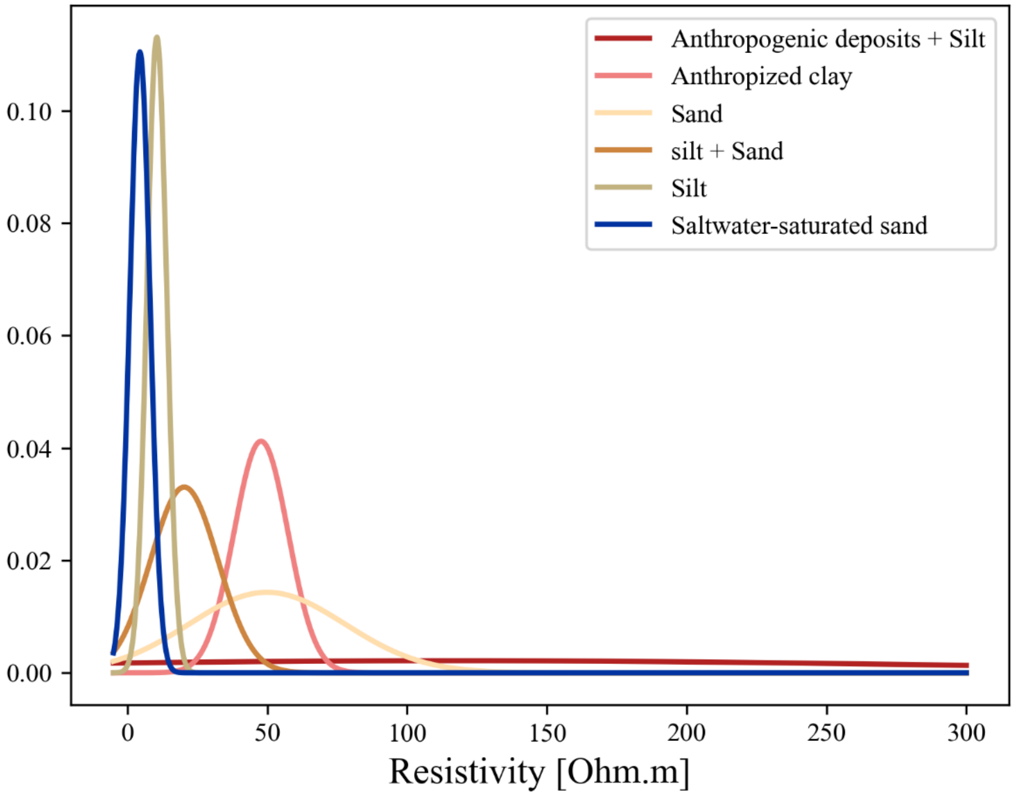

Figure 45: Univariate Gaussian distribution of resistivity with Classification 1

The PDFs of the Category 6 (saltwater-saturated sand) and Category 5 (silt) are distinguishable and are characterised by lower standard deviations, indicating that they correspond to a narrow range of resistivity values. In contrast, the PDF of the anthropogenic deposits is much flatter, as it is associated with a large standard deviation, suggesting a wider range of resistivity values. The PDF of the sands displays a higher standard deviation than that of the Category 2 (anthropized clays), but with a mean that is very similar. This indicates that sands share a similar resistivity range with the anthropized clay which are characterised by a smaller standard deviation. Finally, the Category 4 (silt + sand) can be more distinguishable for the resistivity values above its mean because a part of its PDF is recovered by those of saltwater-saturated sand and Silt.

Table 7 represents the mean and the standard deviation of elevation for Classification 1 used to trace the PDF of each category (Figure 46).

Table 7: Elevation mean (μ) and standard deviation (σ) (Classification 1)

Category	Description	μ [m]	σ [m]
1	Anthropogenic deposits + Silt	1.87	0.90
2	Anthropized clay	-0.89	0.42
3	Sand	-1.99	1.13
4	Silt + Sand	1.25	1.13
5	Silt	-2.37	1.68
6	Saltwater-saturated sand	-5.50	1.64

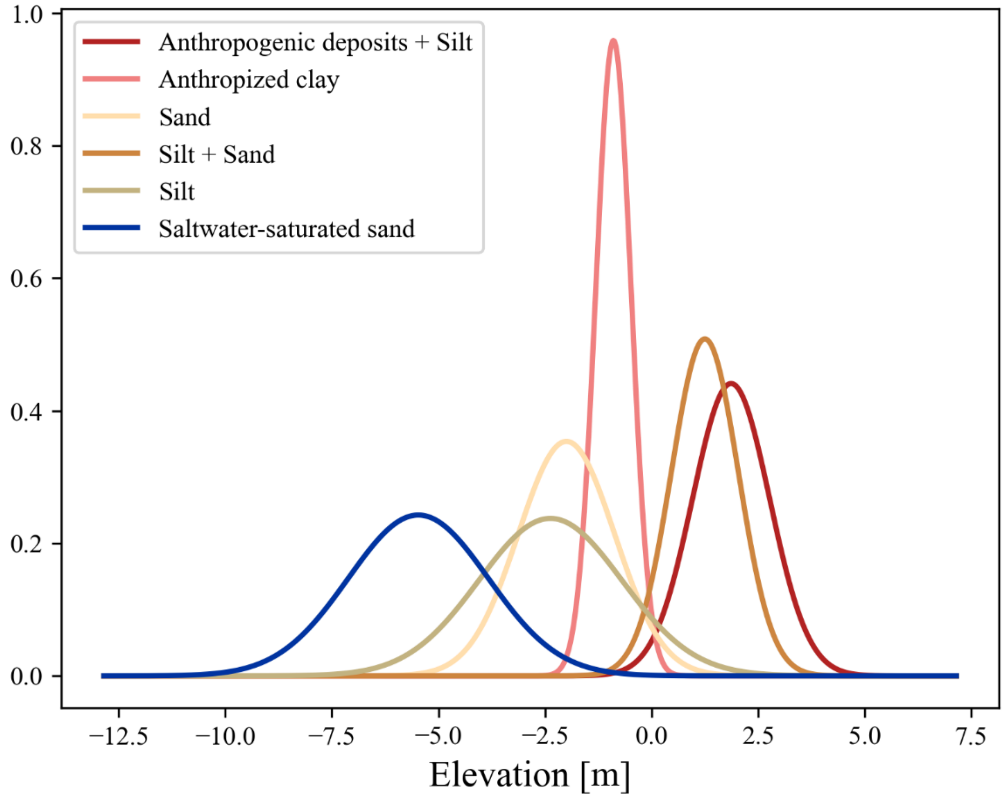

Figure 46: Univariate Gaussian distribution of the elevation with Classification 1

Category 6 (saltwater-saturated sand) are clearly distinguishable at greater depths and the anthropized clay also stand out due to their low standard deviation. The Category 3 (sand) and the Category 5 (silt) show a significant overlap, similar to the overlap observed between anthropogenic deposits and silty-sandy muds.

The result of the classification is then visualised. A final classification map is generated by assigning to each cell of the mesh the category with the highest probability and a map with the probability of the category for each cell of the final classification.

In this part, the profiles R45 and R8 are shown to compare the results of the classification with the drilling.

The result of Classification 1 for profile R4-5 (Figure 47) shows small lenses of anthropized clay, which correspond to the observations made in core C5. However, in core C4, no lens was detected where the core indicated anthropized clay. The less resistive cells near the surface are classified as silty and sandy mud deposits (Category 4), but with low probability (Figure 48). Moreover, silt deposits (Category 5) are not very represented and have a low probability. This is consistent with expectations, as the distributions overlap at shallow depths and this type of deposit was rarely observed in the cores. Finally, the saltwater-saturated sand seems to appear at 5 or 6 m bellow current sea level.

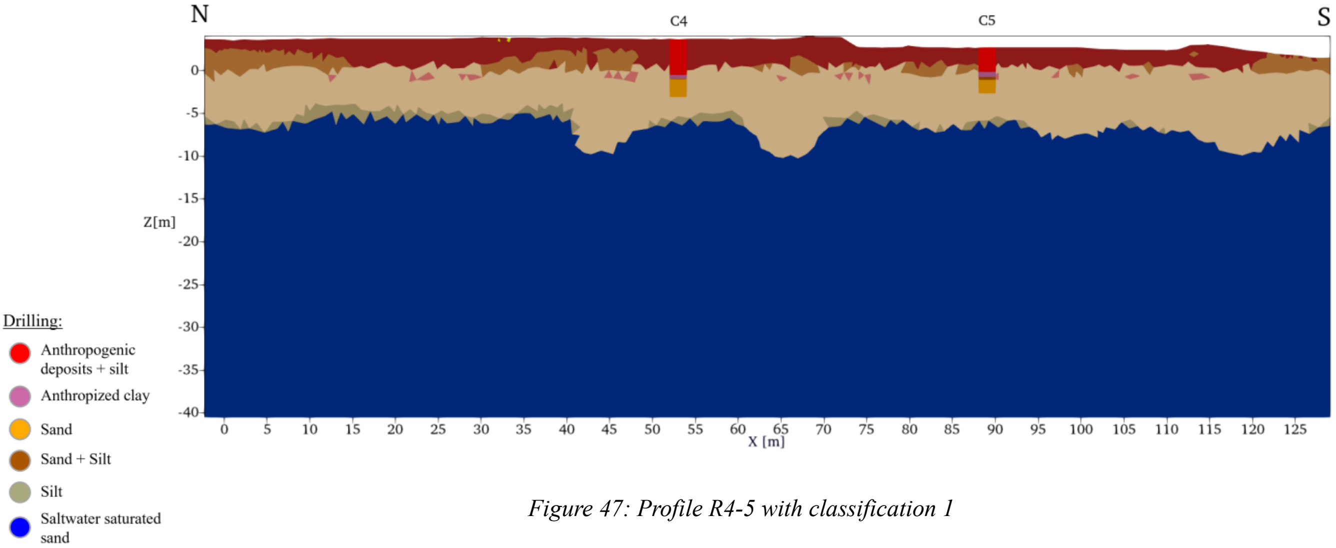

Figure 47: Profile R4-5 with classification 1

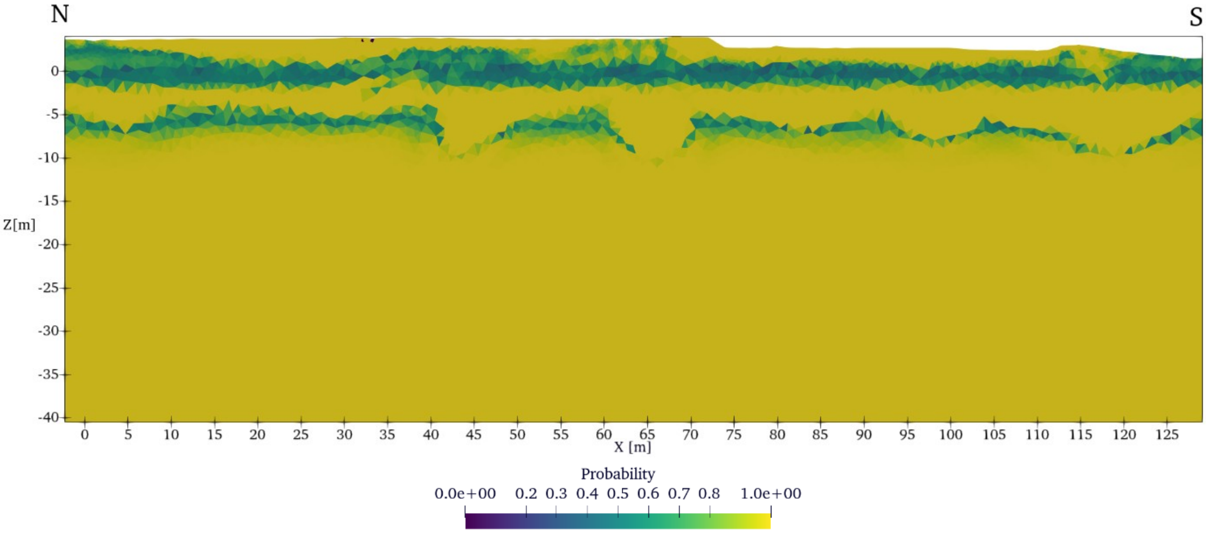

Figure 48: Probability of each cell with Classification 1 (Profile R4-5)

The result of Classification 1 for profile R8 (Figure 49) shows some small lenses of clay anthropized but none of them correspond to observations made in core C2. Anthropized clay has a probability of occurrence of 2.1%, which explains its underrepresentation. The classification failed to identify the silty sand present at the bottom of core C1, as it was underrepresented in the dataset.

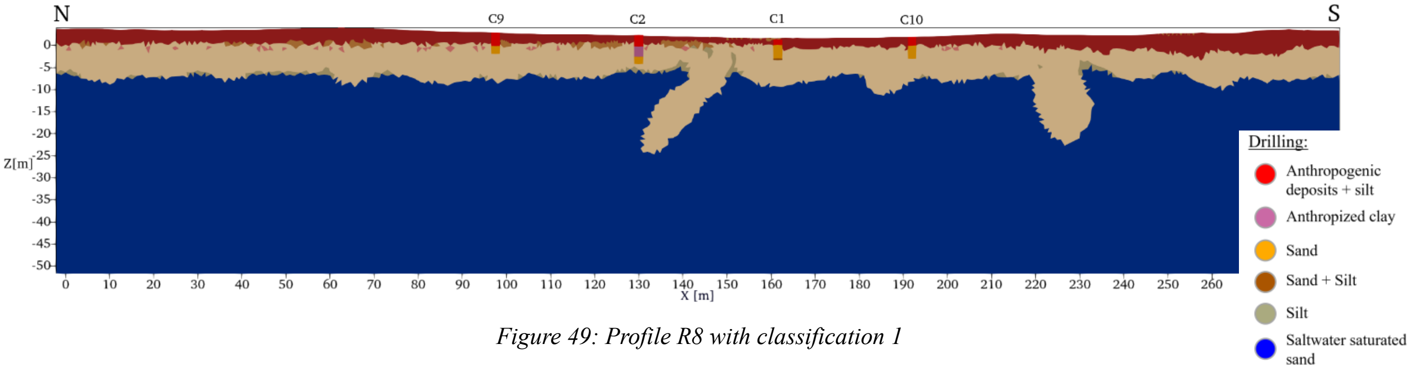

Figure 49: Profile R8 with classification 1

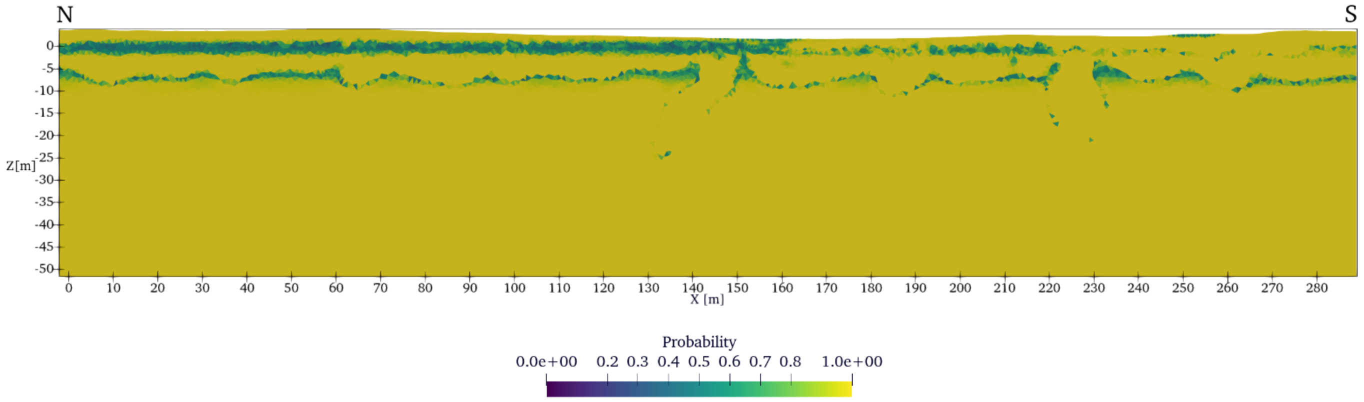

Figure 50: Probability of each cell with Classification 1 (Profile R8)

In contrast, core C10 matches the classification results perfectly. The sand at the bottom of core C9 is also correctly classified, but a lens of silty sand appears on the southern edge of C9 where it should not be present. The primary aim of the classification is to distinguish anomalies at depth. In this case, these anomalies are likely to be more resistive sands than the saltwater-saturated sands and are not of anthropogenic origin.

For both profiles, the area beneath the anthropogenic deposits is characterised by low probability (Figure 48 and Figure 50). The classification is also uncertain regarding the boundary between the more resistive sands (most likely unsaturated or saturated with freshwater) and the sands saturated with saltwater.

Classification 2

Table 8 represents the resistivity mean and the standard deviation for the Gaussian PDF's when the number of data points from the DP logs is reduced. PDFs are represented in Figure 51.

Table 8: Resistivity mean (μ) and standard deviation (σ) (Classification 2)

Category	Description	μ [Ω.m]	σ [Ω.m]
1	Anthropogenic deposits + Silt	129.97	129.74
2	Anthropized clay	47.77	9.61
3	Sand	49.91	27.84
4	Silt + Sand	21.24	10.61
5	Silt	11.50	3.81
6	Saltwater-saturated sand	5.30	3.98

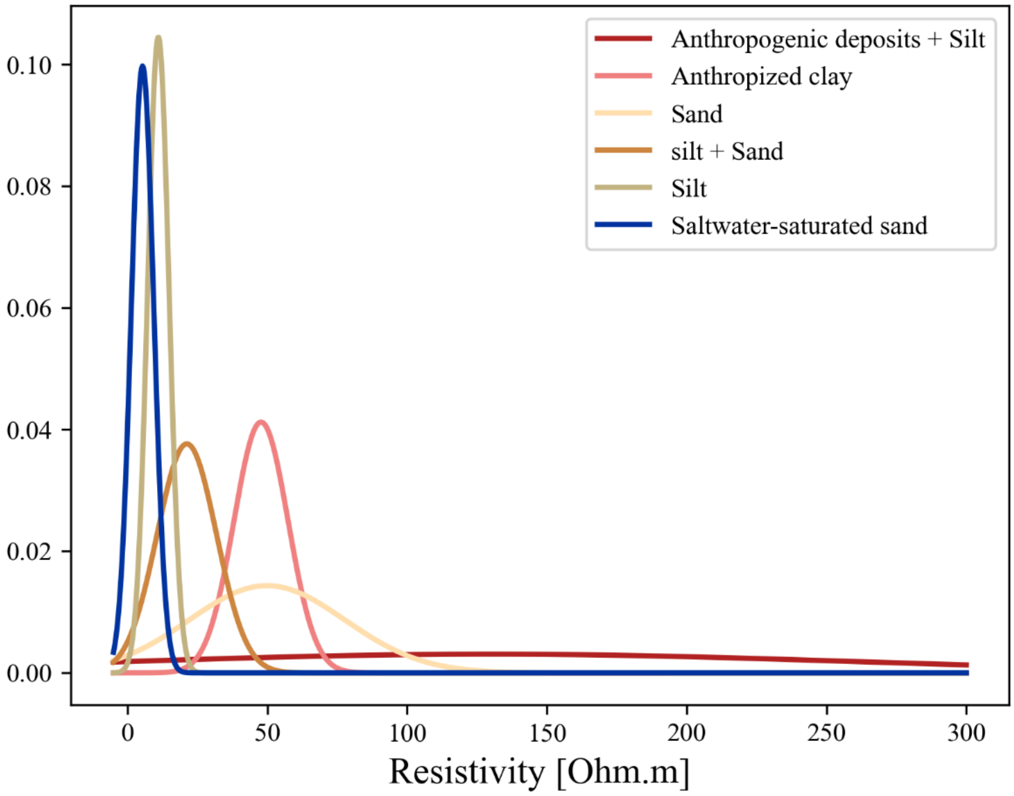

Figure 51: Univariate Gaussian distribution of resistivity with Classification 2

With Classification 2, the resistivity PDFs are quite similar to those of Classification 1, except that the Category 1 (Anthropogenic deposits and Silt) are characterised by a higher mean resistivity and a smaller standard deviation, although their PDF remains relatively flat.

As for the Classification 1, the PDFs of the Category 6 (saltwater-saturated sand) and Category 5 (silt) are distinguishable and are characterised by lower standard deviations quite similar. Their means are slightly higher than those obtained with Classification 1. For Category 4, there is also only slight variations between the two classifications. The resistivity PDFs of Categories 2 and 3 do not vary between classifications, as they are not represented in the DP tests.

Table 9 represents the mean and the standard deviation of elevation for Classification 2 used to trace the PDF of each category (Figure 52).

Table 9: Elevation mean (μ) and standard deviation (σ) (Classification 2)

Category	Description	μ [m]	σ [m]
1	Anthropogenic deposits + Silt	1.18	1.04
2	Anthropized clay	-0.89	0.42
3	Sand	-1.99	1.13
4	Silt + Sand	0.10	1.13
5	Silt	-3.58	1.59
6	Saltwater-saturated sand	-6.59	1.65

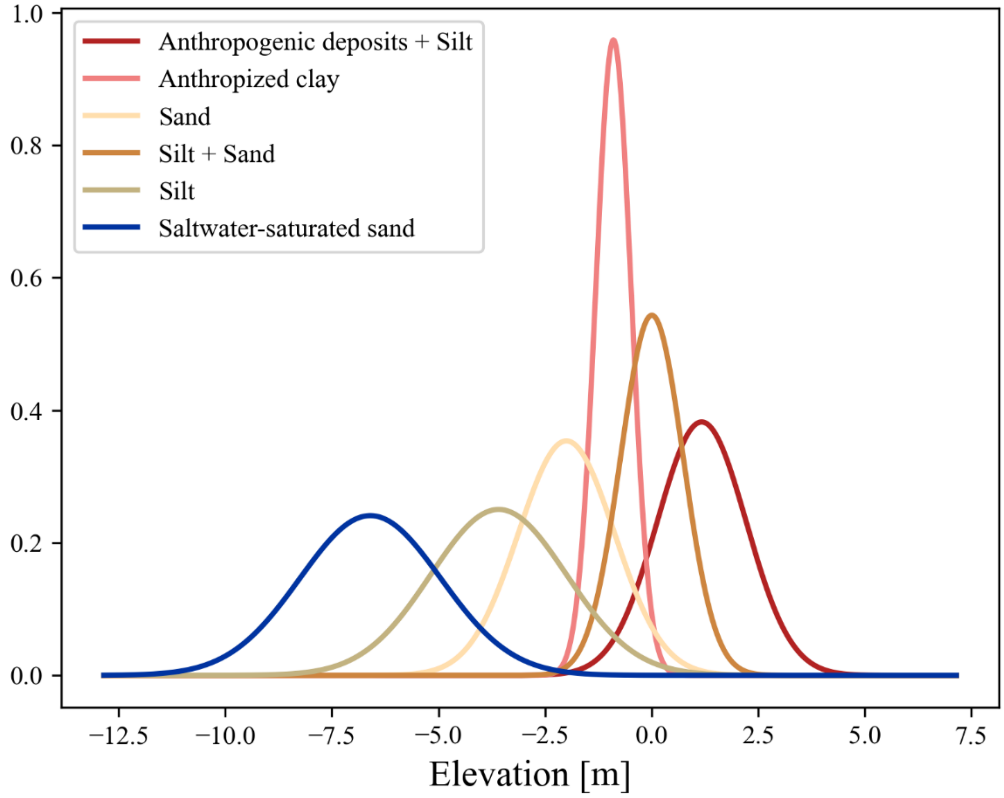

Figure 52: Univariate Gaussian distribution of the elevation with Classification 2

The elevation PDFs of category 1, 4, 5 and 6 in Classification 2 have lower elevation mean than Classification 1 but it is predictable because the real DPs elevation is lower than the elevation mean of ERT data measurements. With Classification 2, the peak of each PDF can be better isolated than with Classification 1.

The result of Classification 2 for profile R4-5 (Figure 53) shows more silty and sandy mud (Category 4) and silty mud (Category 5) but always in less probable cells. Anthropogenic deposits (Category 1) are more present in Classification 2 and aligns a little bit better with the observations made from the boreholes C4 and C5. A more resistive lens can also be observed at 2 m bellow the sea level between 30 and 35 m in the x-axis.

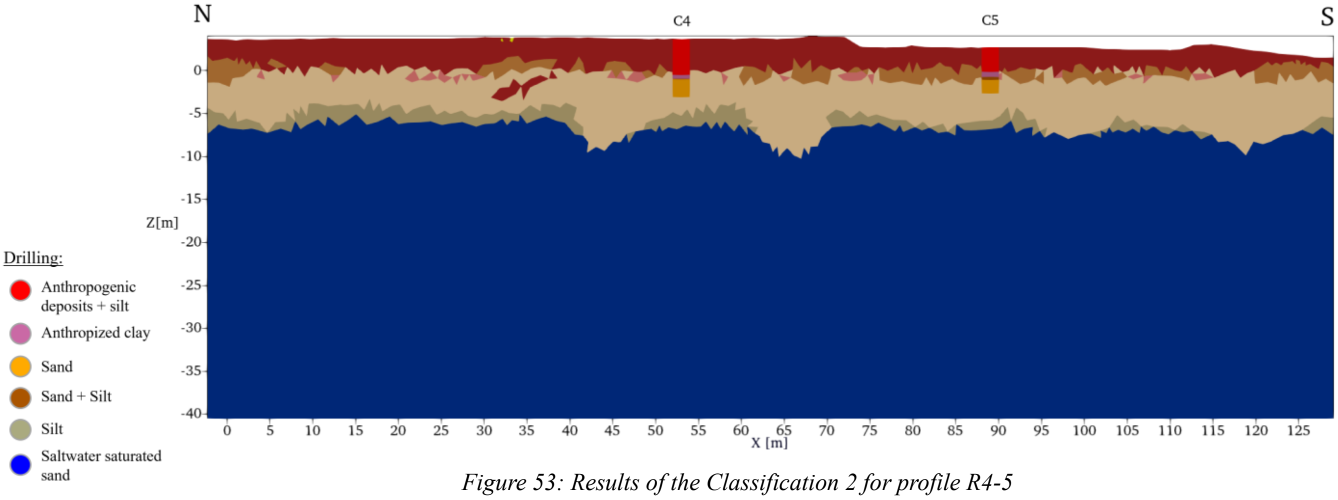

Figure 53: Results of the Classification 2 for profile R4-5

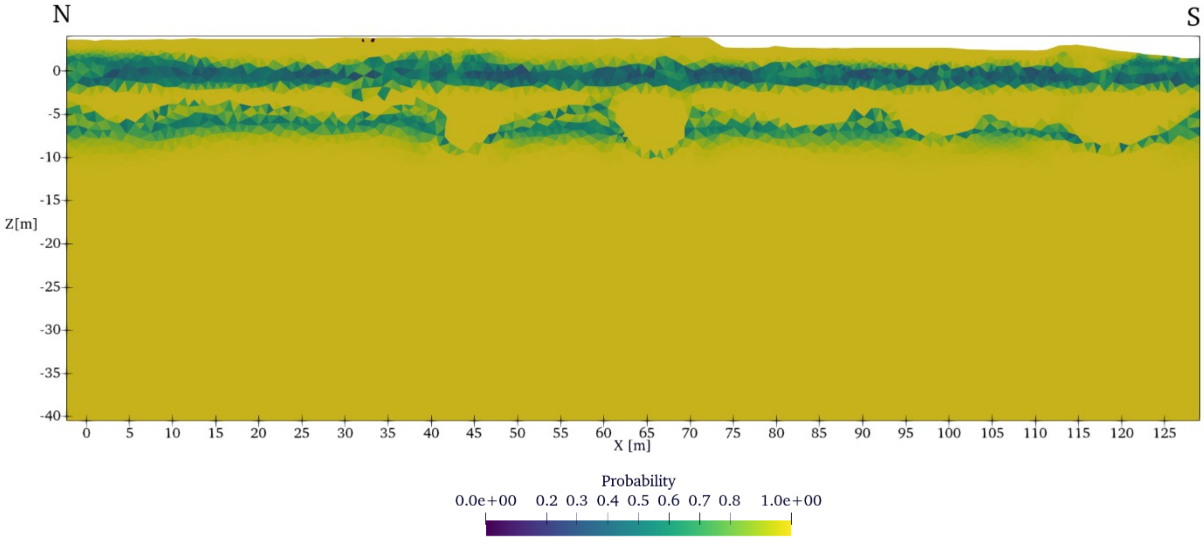

Figure 54: Probability of each cell with Classification 2 (profile R4-5)

The probability of each cell is quite similar for both classifications for profile R4-5 (Figure 48 and Figure 54).

Regarding profile R8 shown in Figure 55, the classification also shows a higher proportion of anthropogenic deposits, which better matches the core analyses in the anthropogenic zone for cores C9 and C2. However, the proportion of anthropic deposits is too high compared with cores C1 and C10. The muddy sand-silt (Category 4) observed in the lower part of core C1 is also not represented here. The anthropogenic clay observed in core C2 is also not well represented with Classification 2.

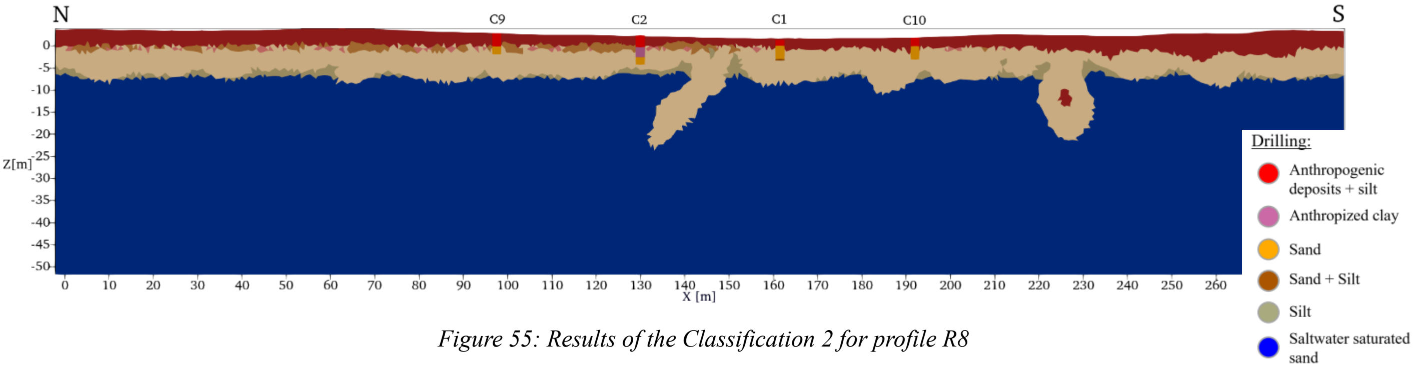

Figure 55: Results of the Classification 2 for profile R8

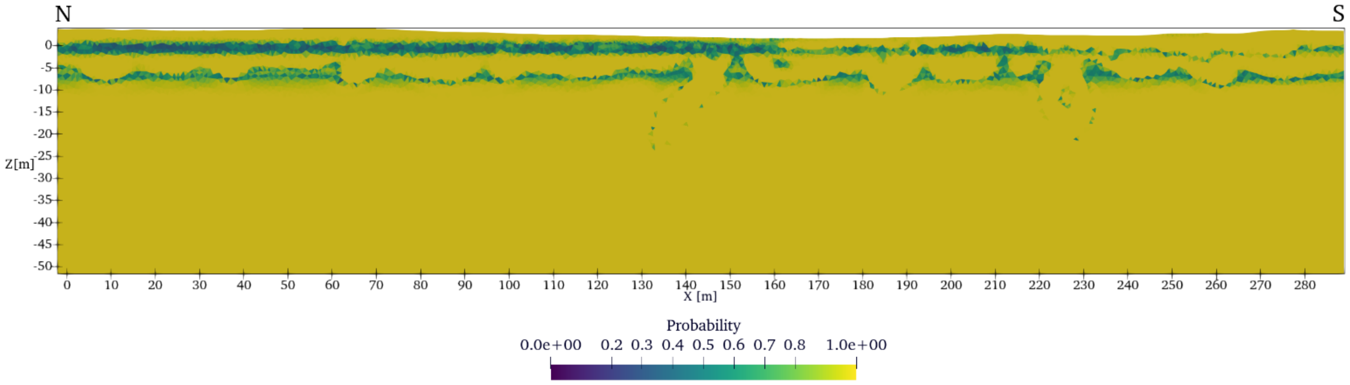

Figure 56: Probability of each cell with Classification 2 (profile R8)

As with profile R4-5, deposits from Categories 4 and 5 are more present than in Classification 1, though still associated with low probabilities (Figure 56). Deep anomalies are also filled with more resistive sands, even though an anthropogenic lens is present within the southernmost anomaly at approximately 12 m below current sea level. These anomalies are also smaller and extend slightly less in depth compared with those from Classification 1.

Comparison between the two classifications

- Category 1 is more prominent when the number of data points is reduced (Classification 2). As a result, some cells classified as Category 3 (sand) or category 4 (Silt + Sand) are classified as Category 1 (Anthropogenic deposits and silt) in Classification 2. For both classifications, the probability of these cells is around 0.4.

- With Classification 2, there is also a lens of anthropogenic deposits at greater depth but it cannot be archaeological deposits because it is too deep so if it is perhaps a classification error.

- With Classification 2, there is also a greater presence of silt, which does not correspond well to reality, as these deposits are fluvial, whereas these profiles are characterised by littoral deposits according to the geological context.

- Most cells where the probability of the selected category was equal to one in Classification 1 remained in the same category in Classification 2.

In conclusion, at first sight, both classifications can be good to classify the resistivity obtained thanks to the inversion of the field data because each classification has advantages and drawbacks:

Table 10: Advantages and drawbacks of each classification

Classification	Advantages	Drawbacks
1	+ Not anthropogenic deposits in depth + Better proportion of silt	- Greater overlap of the PDFs for elevation.
2	+ Better representation of anthropogenic deposits	- Too much silt - Low-resistivity zones not represented at the surface.

The choice of prior probabilities, the PDFs and the resolution of the inverted models have a significant impact on the classification results. In this case, the prior is identical for both classifications. If one category dominates the prior probability and the inversion does not provide sufficient distinctive information to clearly differentiate the subsurface lithologies, this can lead to a final classification biased towards the most probable facies (Isunza Manrique et al., 2023). This is why Category 2 (anthropized clay) is under-represented in both classifications, as it is dominated by the more probable Category 3.

The PDFs distributions define the parameters such as the shape, location and scale (Isunza Manrique et al., 2023). They play a crucial role in the classification results, as they statistically characterise how each category (lithology or deposit type) is distributed in terms of resistivity and elevation within the model.

The classification process compares the inverted data to these PDFs to estimate the likelihood that each point belongs to a given category. When PDFs are well-separated with minimal overlap, the classification is more accurate. However, significant overlap or poorly defined PDF lead to ambiguity and less reliable classification.

The PDFs themselves are influenced by the data used to construct them. In this study, the main difference between the two classifications lies in the choice of PDFs, which vary depending on how the DP-EC data were incorporated. Depending on the way these data were used, the parameters and shapes of the PDFs changed, causing variations in the classification results. Therefore, careful estimation and selection of PDFs are essential to obtain meaningful and representative classification outcomes.

The resistivity data obtained from the inversion used for classification do not allow all subsurface features to be resolved. The physical property values of the different deposits or lithology categories can overlap within the inverted model space. This overlap reflects an inherent uncertainty in the inversion process, limiting the ability of the methods to clearly distinguish between the different classification categories. It is also important to consider the sensitivity of the inversion to ensure the reliability and accuracy of the classification for a quantitative interpretation of geophysical data (Isunza Manrique et al., 2023). Indeed, the inversion becomes less sensitive and less reliable with depth because the signal is more attenuated, noise increases and spatial resolution decreases.

While variations in class separability may slightly influence the sharpness or clarity of the classification results, the overall impact on the resolution of the inverted model is expected to be limited.

5.5.2. Comparison between iterations of inversion

To evaluate if each classification is consistent with the field data, to each classified cell is assigned the average resistivity of its corresponding category. This is composed a specified starting model for other inversions. This builds on the work presented in the paper written by Isunza Manrique et al., 2023 but had not yet been carried out.

It is also interesting to examine the correspondence between the resistivities obtained from the isotropic inversion and those obtained using the specific starting model. For that, the results of each iteration will be represented in a graph.

Firstly, this type of graph will be plotted for profile R4-5 for both classifications (Figure 57 and Figure 58).

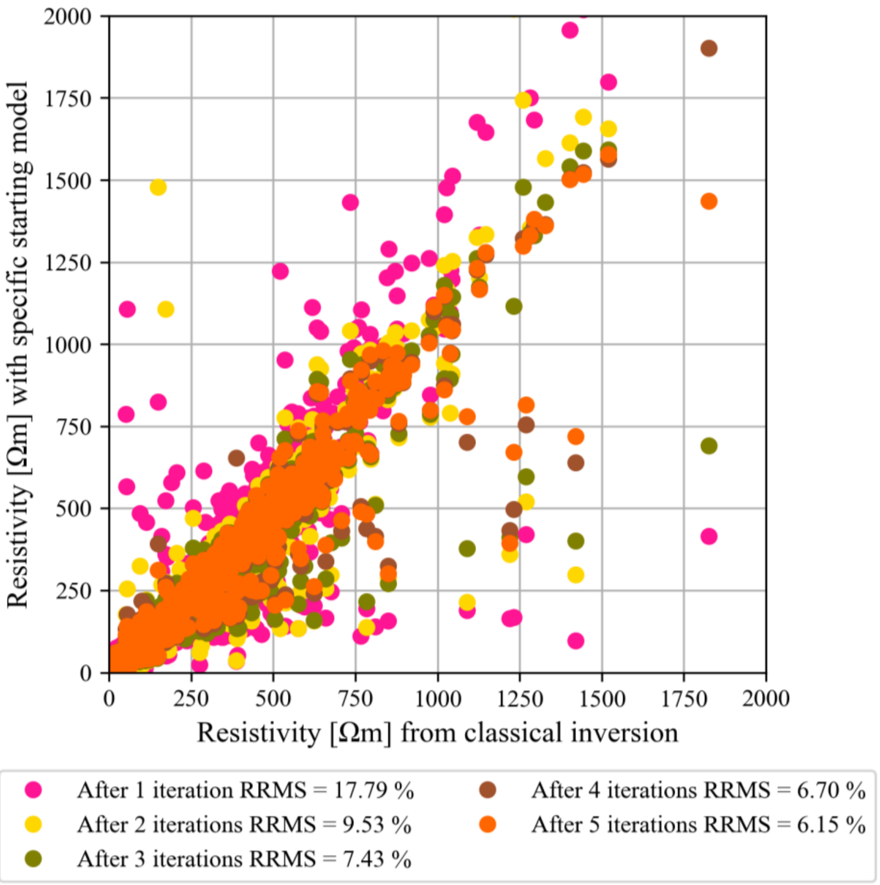

Figure 57: Comparison of inverted resistivities: classical vs specific starting model for R4-5 with Classification 1

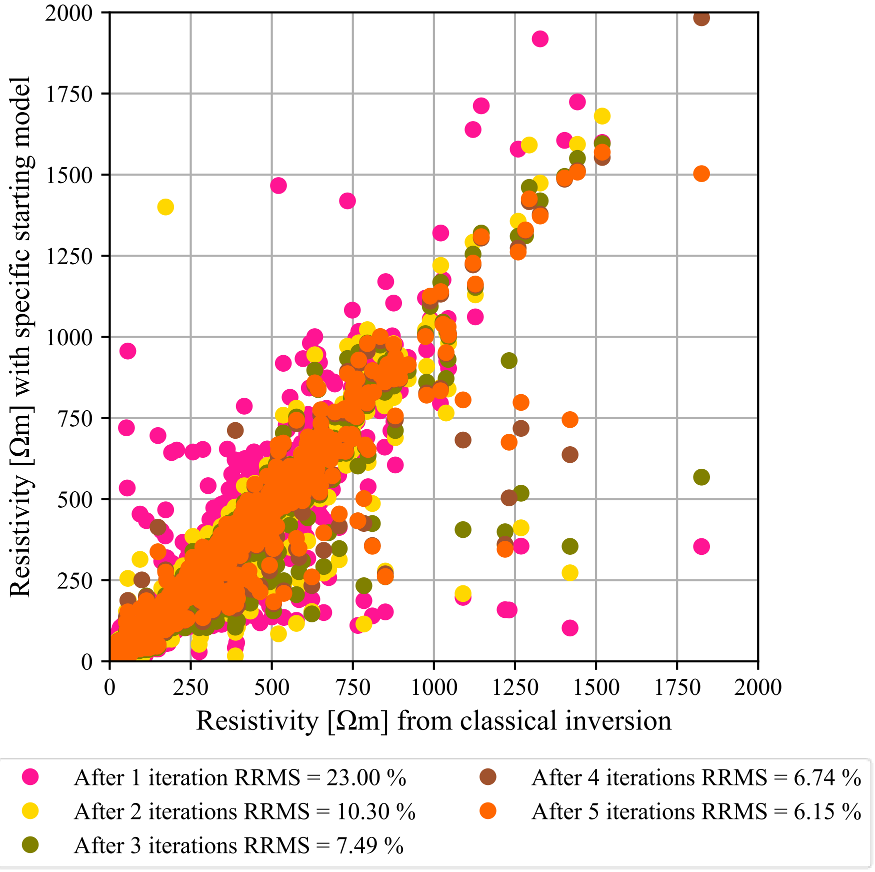

Figure 58: Comparison of inverted resistivities: classical vs specific starting model for R4-5 with Classification 2

For both graphs, the data are distributed around the 1:1 axis, but for each iteration, there are outliers. This indicates that some mesh cells are characterised by resistivity values different from those obtained in the classical isotropic inversion in particular for the first inversion.

The RRMS for the first iteration of Classification 1 (17.79%) is lower than that of the first iteration of Classification 2 (23.00%), indicating that the starting model and thus Classification 1, is more likely to be adequate. After five iterations, the RRMS is the same for both classifications (6.15%) and look vert-y similar. This RRMS remains higher than that of the classical isotropic inversion (4.61%).

To have another example, this type of graph will also be plotted for profile R8 for both classifications (Figure 59 and Figure 60).

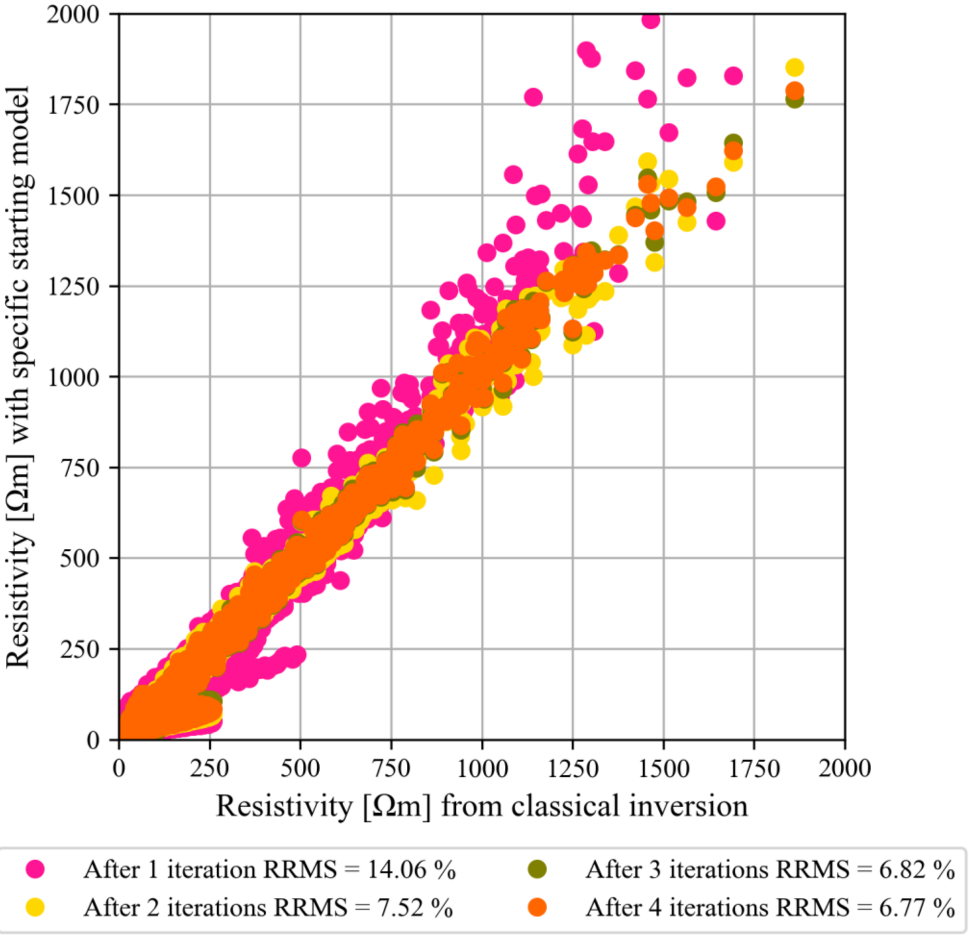

Figure 59: Comparison of inverted resistivities: classical vs specific starting model for R8 with Classification 1

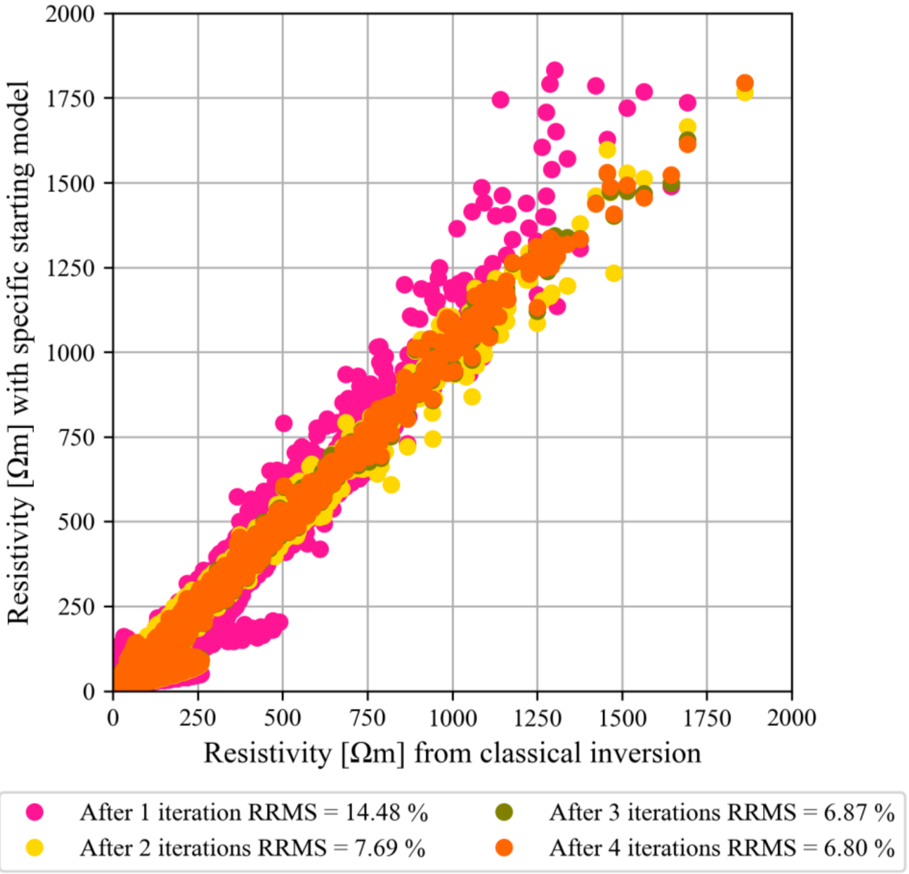

Figure 60: Comparison of inverted resistivities: classical vs specific starting model for R8 with Classification 2

By analysing both graphs and comparing them with profile R4-5, after just one iteration the points are already better aligned along the 1:1 axis for both classifications. In the case of the first classification, the points are slightly offset, indicating that the resistivity values from the specific starting model are higher than those from the classical isotropic inversion. After 2 iterations, points are very well aligned along 1:1 axis which means that the resistivities of both types of inversions are very similar.

The RRMS values for both classifications are very similar at each iteration and in both cases the inversion converges after four iterations with an RRMS of approximately 6.80%, which is slightly higher than the RRMS of the classical isotropic inversion (6.37%).

For these two profiles, both classifications converge in the same number of iterations, with the first classification consistently yielding lower RRMS values at each iteration, indicating a slight performance advantage. Once convergence is achieved, both classifications produce identical results. In fact, the inversion could feasibly be terminated after just two iterations for R8 or three iterations for R4-5, as the outcomes are already compelling.

5.5.3. Inversion results

Here are the inversion results with Classification 1. Figure 61 shows the inversion of profile R4-5.

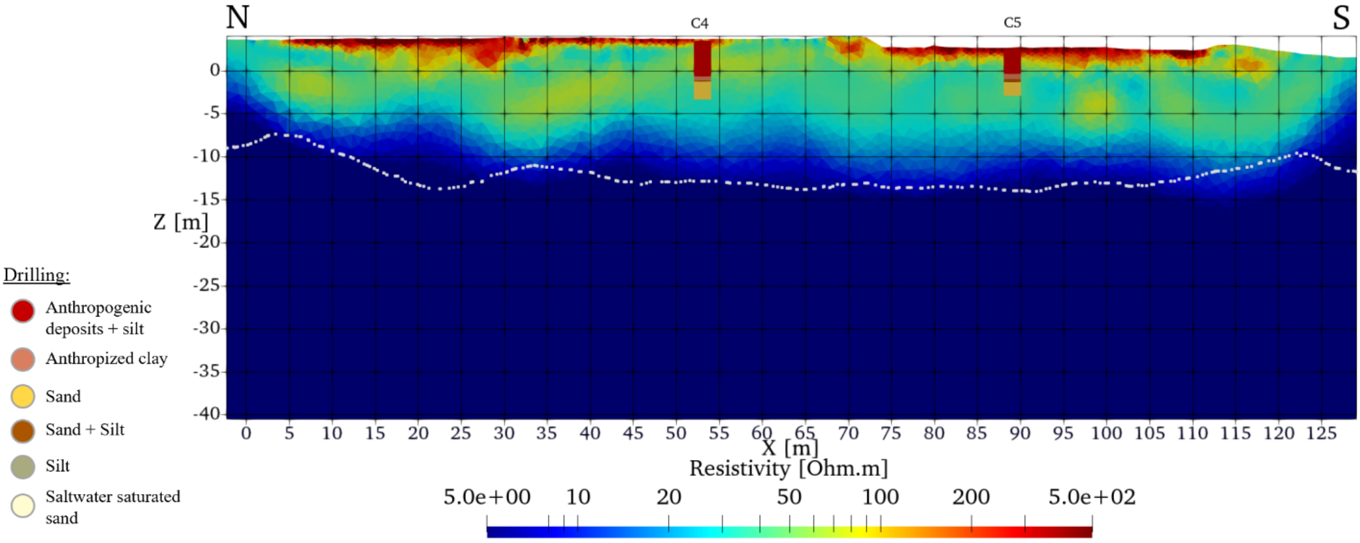

Figure 61: Results of inversion with Classification 1 for profile R4-5 (RRMS = 6.15% – χ^2 = 0.98)

The inversion of profile R4-5 using a starting model derived from classification appears similar to the isotropic inversion near the surface.

When comparing the inversion results with the anthropogenic deposit zones identified through coring, these deposits are not only characterised by very high resistivity values (above 200 Ω·m), but also by intermediate values ranging from 70 to 80 Ω·m. This can likely be explained by the presence of water, as the current groundwater table lies approximately 2 m below the surface.

The more resistive zone observed between 30 m and 40 m along the x-axis in the isotropic inversion is no longer visible in the classification-based inversion.

Figure 62 shows the inversion of profile R8 with Classification 1.

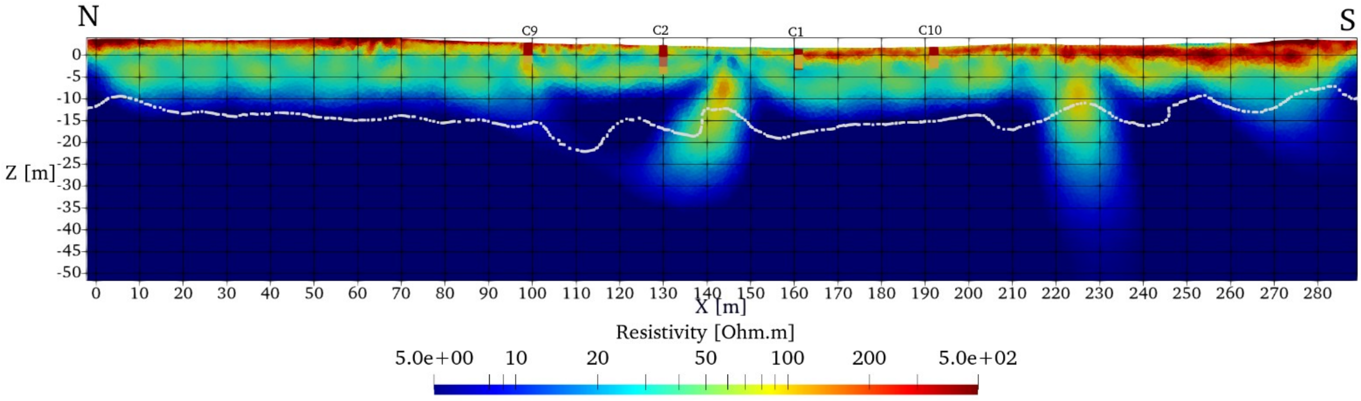

Figure 62: Results of inversion with Classification 1 for profile R8 (RRMS = 6.77% – χ^2 = 1.56)

For profile R8, the inversion over the first 10 m is consistent with the isotropic inversion. However, the anomalies appear less resistive and extend less deeply.

The greater depth extent of these artifacts in the isotropic inversion is most likely a result of the inversion process itself.

5.5.4. Classification and inversion for other profiles

The profiles R6, R7, R10, R11, P7 and P8 will be classified. The classification results are presented in the Annexe 9.3.

The profiles R7, R11 and R10 are inversed using Classification 1 as starting model. For these inversions, the limit of each layer is shown in different colour.

For the inversions of the three profiles shown in Figure 63, Figure 64 and Figure 65 the anomalies are also limited in depth. In all three cases, the category ‘anthropogenic deposits + silts’ corresponds to the highest resistivity values. Furthermore, the boundary of the sandy deposits, likely saturated with freshwater, is clearly visible and aligns with the limit defined by the classification (beige line). Moreover, in all three cases, the silty deposits are scarcely represented and are likely not present in reality; these are misclassified areas.

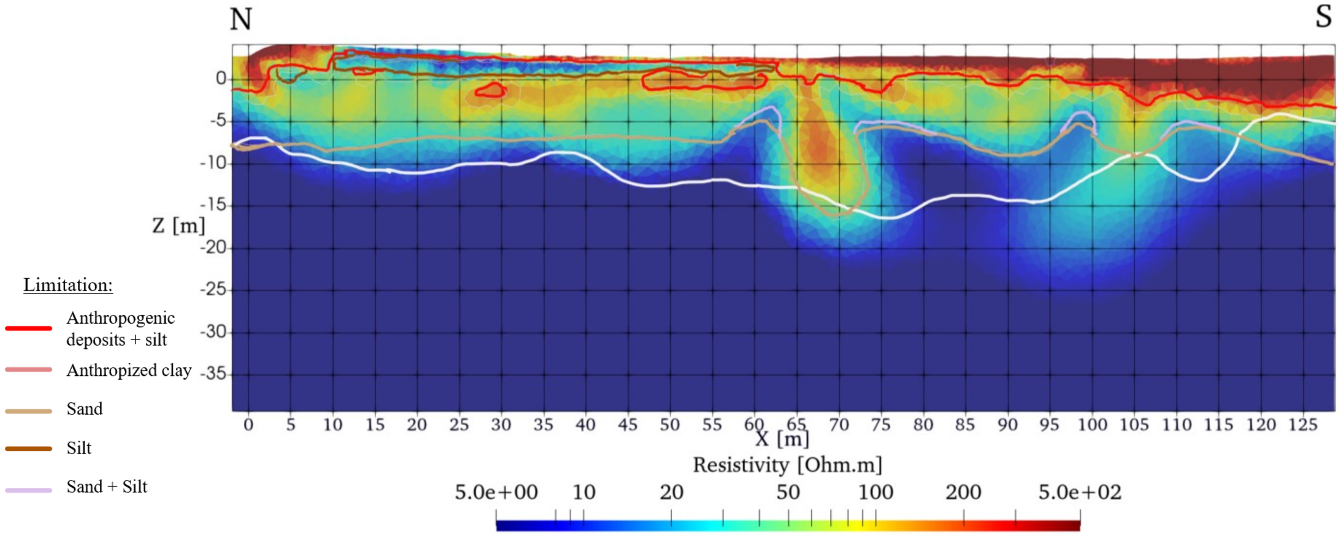

Figure 63: Results of inversion with Classification 1 for profile R7 (RRMS = 4.82% – χ^2 = 1.47 – iterations = 5)

For profile R7, the conductive lens near the surface (between 10 and 45 m along the x-axis) is associated with the 'silt + sand' deposits but with low probability. The origin of this lens will be discussed in more detail in Section 5.6.

For profiles R10 (Figure 64) and R11 (Figure 65), a more resistive cluster is still present at around 100 m along the x-axis. It appears deeper on profile R11 (5 to 10 m below sea level) than on profile R10 (3 to 8 m below sea level).

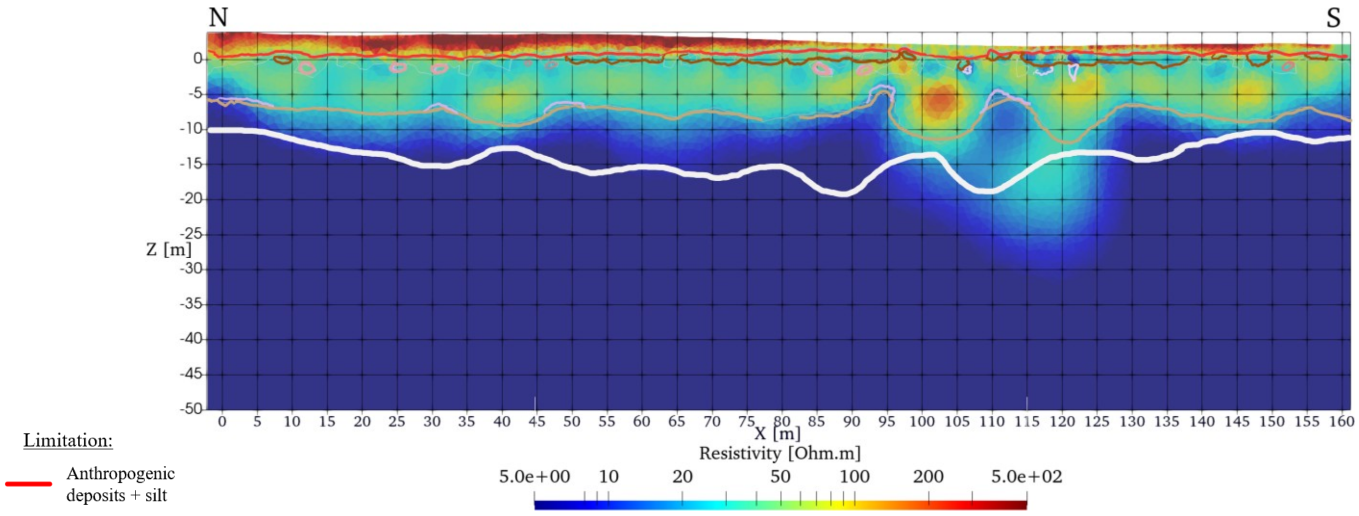

Figure 64: Results of inversion with Classification 1 for profile R11 (RRMS = 6.29% – χ^2 = 2.52 – iterations = 4)

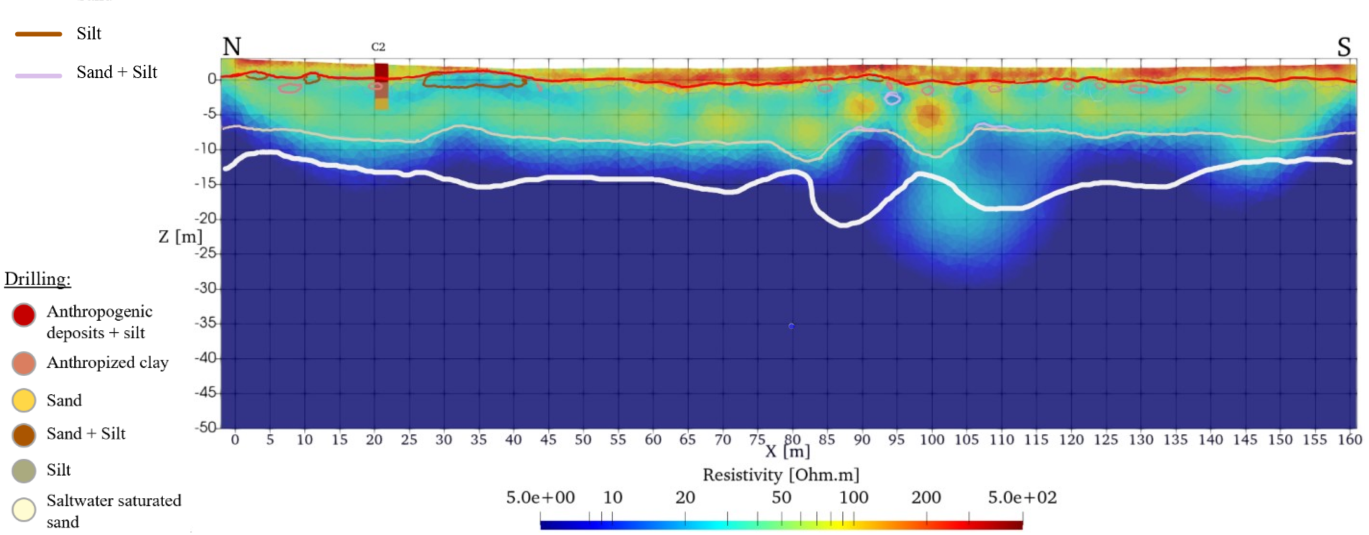

Figure 65: Results of inversion with Classification 1 for profile R10 (RRMS = 4.81% – χ^2 = 1.47 – iterations = 4)

For profile R10, an anthropogenic clay lens is situated in the core C2 but is too small. The less resistive area near the surface (between 30 and 40 m along the x-axis) is classified as 'silt + sand', but it should rather be characterised as anthropized clay, as it appears to be part of the same less 'anthropized clay' lens identified from the core.

5.5.5. Conclusion for the probabilistic approach

The probabilistic approach made it possible to define a suitable starting model for inverting the profiles, which obviously significantly reduced the inversion time.

Moreover, all profiles are very similar to the isotropic inversions previously conducted, except that no deep-reaching anomalies are present anymore and the boundary between the anomalies and the water-saturated sands is more clearly defined.

The RRMS was used as the primary criterion for determining the most relevant classification. A lower RRMS value indicates that the inversion more accurately reproduces the field-acquired data. In this case, the parameters distinguishing the two classifications were the probability density functions (PDFs); thus, selecting one classification over the other implicitly means considering its associated PDFs as more representative. The prior probabilities also play a decisive role and varying them could lead to significantly different classification results. Moreover, the final classification outcome serves as a key basis for interpretation; therefore, the choice of the retained classification is particularly important, as the interpretation directly depends on it.

In this study, both classifications are visually consistent. The first classification was chosen because it achieved a better RRMS after one iteration, indicating that the starting model was more reliable. The second classification remains good overall. For interpretation purposes, however, the two classifications do not lead to the same conclusions. Indeed, in the first classification, the anomalies observed at depth are classified as sands, whereas in the second classification, anthropogenic lenses appear. Since anthropogenic material at a depth of 10 to 15 m is unlikely, this further supports the conclusion that the first classification is better.

Drilling additional cores of varying depths in the study area would help improve the classification. Having more measurement points within the first five meters could potentially reduce the number of cells for which the associated category probability is low. Drilling deeper cores at the location of the more resistive anomalies could also help determine their exact nature.

The ’silt’ category is not present in the cores done on the area studied by the classification except for the drilling done near the Tiber but this zone (profiles R1, R3 and R9) is not study by this classification because to study these profiles, one other category has to be considered: the ‘clay + gravel’ category observed in core S1. Moreover, for this profile, ‘silt’ category is saltwater saturated as it visible in isotropic inversion of profile R3 (Figure 28).

5.6. Anisotropic inversion over the first metres

To better delineate the archaeosphere, the profiles were re-inverted, this time focusing only on the first few meters. The profiles were divided into two groups. The inversions were carried out with the same parameters as the complete ones, with the additional consideration of some anisotropy.

The first group concerns the profiles close to the Tiber (R3, R1 and R9) to focus on the transition between fluvial and littoral deposits. The second group consists of the six other profiles (R45, R6, R7, R8, R10 and R11) and focuses on coastal-type deposits.

5.6.1. Profiles closed the Tiber

For profile R1, the shallow-depth inversion does not provide more information than the full-depth inversion. However, profiles R3 and R9 were reinverted by introducing a certain degree of anisotropy (Figure 66 and Figure 67). The purpose of reinverting profile R3 was to verify whether the anomaly observed at 75 m is due to the inversion process or if it is a real feature.

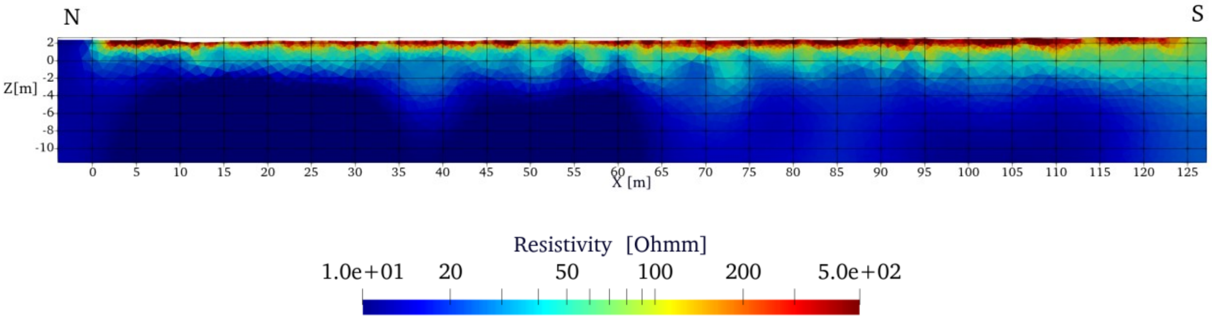

Figure 66: Surface inversion for profile R3 (RRMS = 3.62% – χ² = 0.73)

Upon analysing Figure 66, the anomaly appears to be absent, but a vertical resistivity contrast can be observed around 65 m along x-axis. This vertical change may correspond to the boundary between fluvial deposits to the north and littoral deposits to the south. To confirm this hypothesis, additional analyses would be necessary. From a physical perspective, it is possible that fluvial deposits saturated with saline water, having a coarser grain size and thus better pore connectivity, exhibit lower resistivity than coastal deposits, which are also saturated with saline water but are finer-grained, with good porosity but poor pore connectivity.

In comparison with the other profile, the region with very low resistivity appears at a shallow depth, around 2 m below sea level.

The same conclusion can be done by examine profile R9 in Figure 67, below the archaeosphere, the resistivity is a little bit higher in the south of the profile. Moreover, for this profile, the inversion no longer shows any highly resistive anomaly extending in depth in the northern part of the profile.

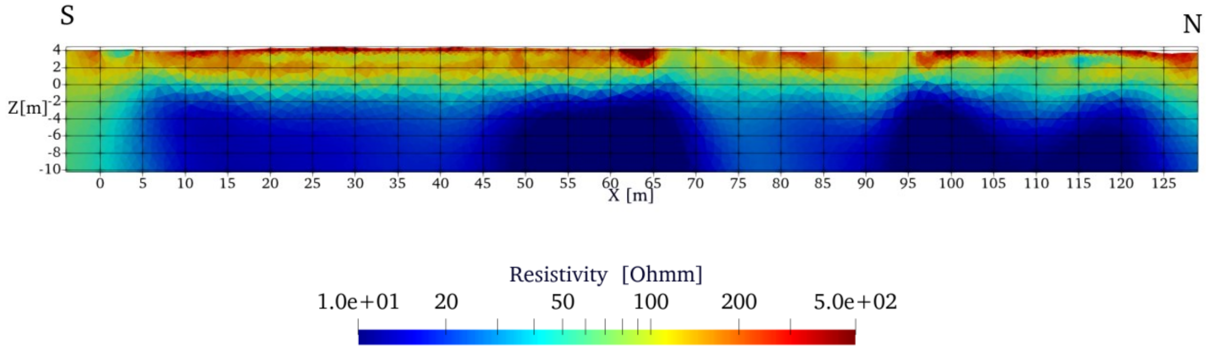

Figure 67: Surface inversion for profile R9 (RRMS = 3.62% – χ² = 0.88)

5.6.2. *Other profiles*

To focus on the archaeosphere, the profiles were inverted over the first 10 m using an anisotropy factor of 0.5 and then classified (using Classification 1). These classifications were subsequently used as the starting model for new inversions.

To help with interpretation, the profiles were also subdivided into different zones based on surface observations. For each zone, a graph was created showing depth as a function of resistivity.

R4-5 interpretation

Profile R4-5 is a section that has already been studied. Figure 68 shows the classification of the profile R4-5. As for the classification of the isotropic inversion, the core analysis doesn't fit perfectly with the classification results.

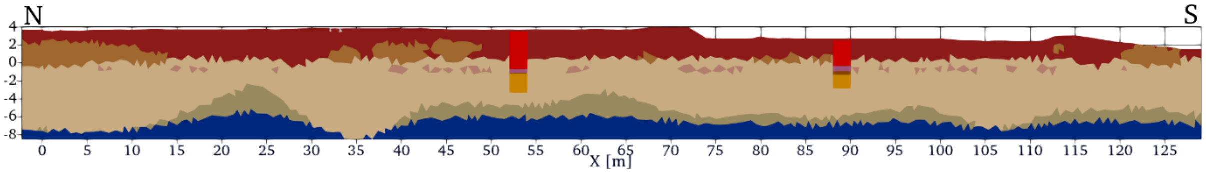

Figure 68: Classification of the first 10 m for profile R4-5

Figure 69 shows the inversion results superimposed on the satellite map to compare them with what can be observed in the field.

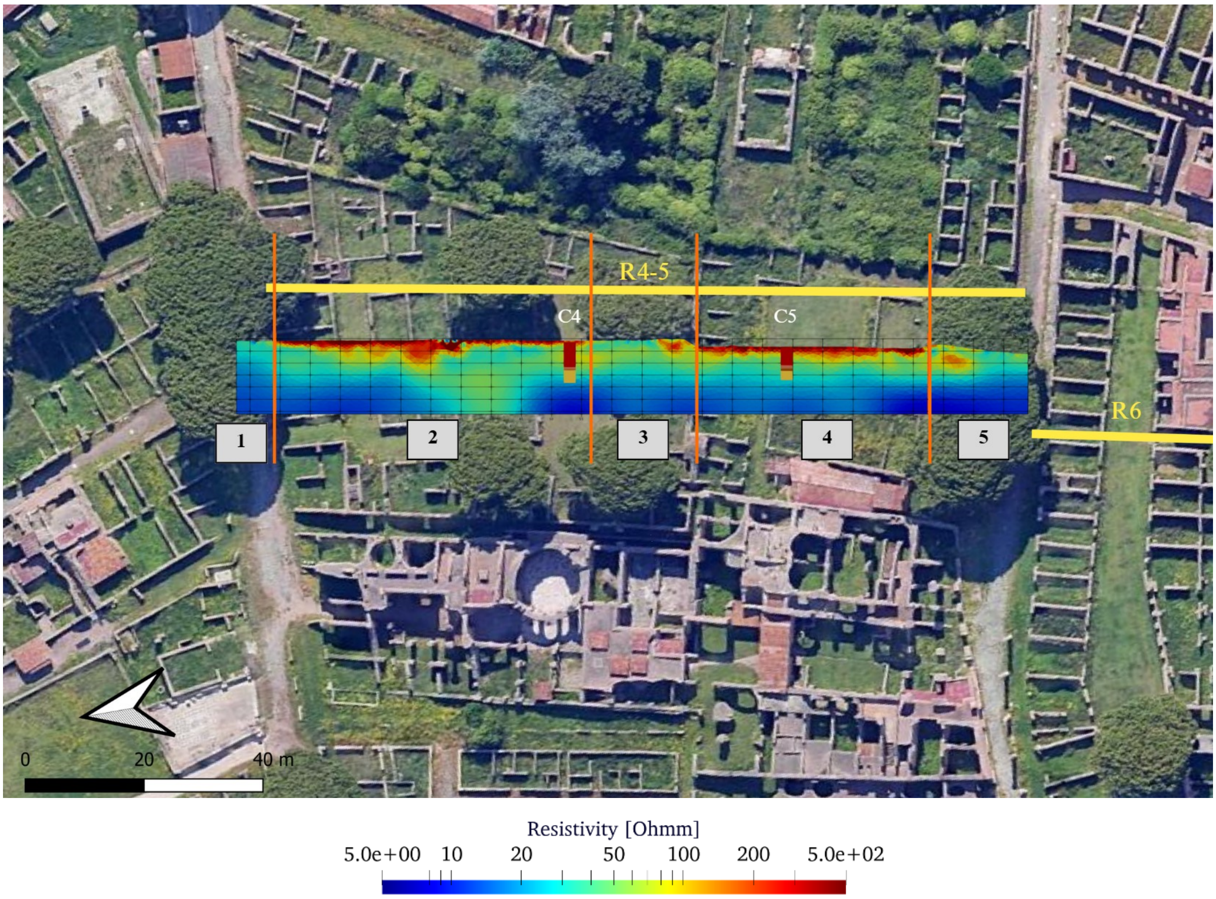

Figure 69: Map shown the correlation between the inversion of R4-5 and the satellite image (RRMS = 3.22% – χ^2 = 0.70 – iterations = 5)

As for the classifications results, upon examining the results from core C4, it appears that the inversion does not match the core analysis. Indeed, strongly anthropogenic deposits are present about thirty centimetres below current sea level in the cores, whereas the inversion shows anthropogenic deposits, associated with high resistivity values, only in the first two meters. This discrepancy suggests that part of the anthropogenic deposits may be characterised by lower resistivity values, likely due to their location in a water content region or that the projection of the cores onto the profile is not correct because the environment is very complex.

A horizontal alternation of more and less resistive zones can be observed in Figure 69. The less resistive Zones (1, 3 and 5) seem to correspond to areas that, during the Roman period, were used as roads. Zones 2 and 4 are more resistive and correspond to areas interpreted as residential structures.

At greater depths, ridges and swales should be distinguishable. The residential areas were likely built on unsaturated sandy deposits, which are generally more resistive, while roads were constructed on finer, clay-rich deposits that tend to have lower resistivity. The two swales also appear to differ. The one to the north is more resistive than the one to the south. In the northern part, the data exhibit a wider spread extent.

Figure 70 shows the alternation of highly resistive and less resistive zones.

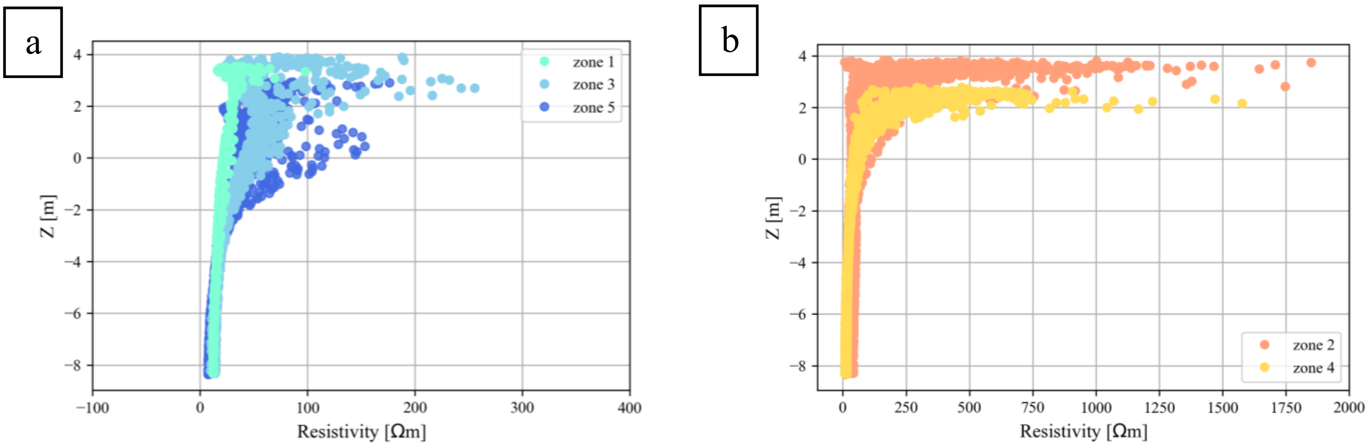

Figure 70: Resistivity [Ω·m] in function of elevation (Z) for the 5 zones (profile R4-5): (a) less resistive zones, (b) more resistive zones

Analysing the graphs, residential zones display resistivity values reaching up to 2000 Ω·m, while road areas show resistivities not exceeding 100 Ω·m for the Zone 1 and 200 Ω·m for the Zone 3 et 5 because there are also more resistive lenses in these areas.

R6 interpretation

The analysis of this profile must be linked to profile R4-5 because it is located as a continuation of R4-5 towards the south. The classification result is shown in Figure 71. In profile R6, the freshwater-saturated sands appear to extend deeper than on profile R4-5, while the anthropogenic deposits reach the same depth as on profile R4-5.

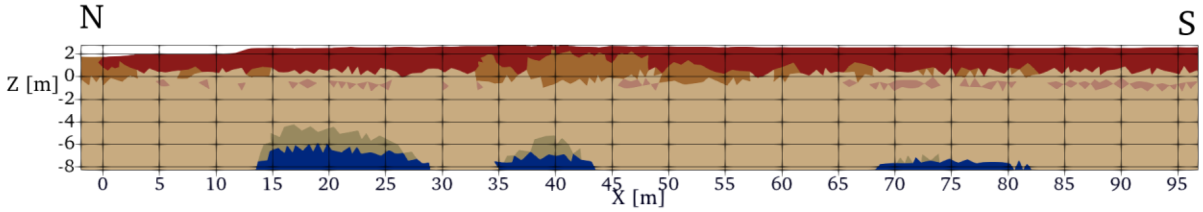

Figure 71: Classification of the first 10 m for profile R6

In Figure 72, six areas were delineated using the satellite imagery. The inversion is quite similar than the isotropic inversion.

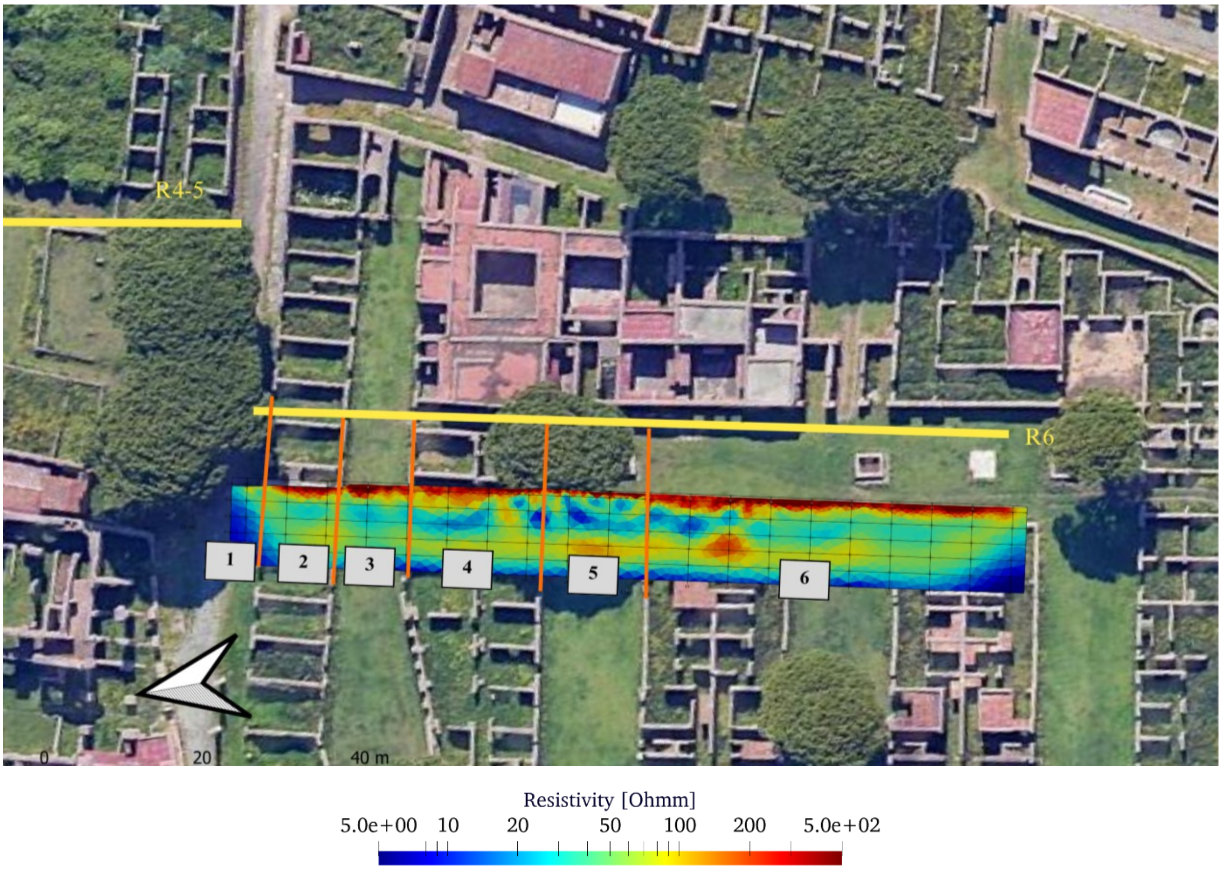

Figure 72: Map shown the correlation between the inversion of R6 and the satellite image (RRMS = 5.07% – χ^2 = 1.36 – iterations = 4)

From north to south, zone 1 represents a road and is characterised by same resistivity values than roads observed in profiles R4-5. Zone 2 represents a living room and Zone 3 represents a path, both zones are characterised by resistivity values between 200 and 900 Ω·m (Figure 73a). Then, Zones 4 and 5 represent a corridor and have the same range of resistivity. However, in Zone 5, below the more resistive layer, there is a more conductive lens. This seems to be related to the presence of a stone pine on the surface. Finally, Zone 6, the southernmost, is characterised by higher resistivity values that can reach up to 1800 Ω·m (Figure 73b). This zone most likely represents a slab. The different surface resistivity values may possibly be explained by using different construction materials.

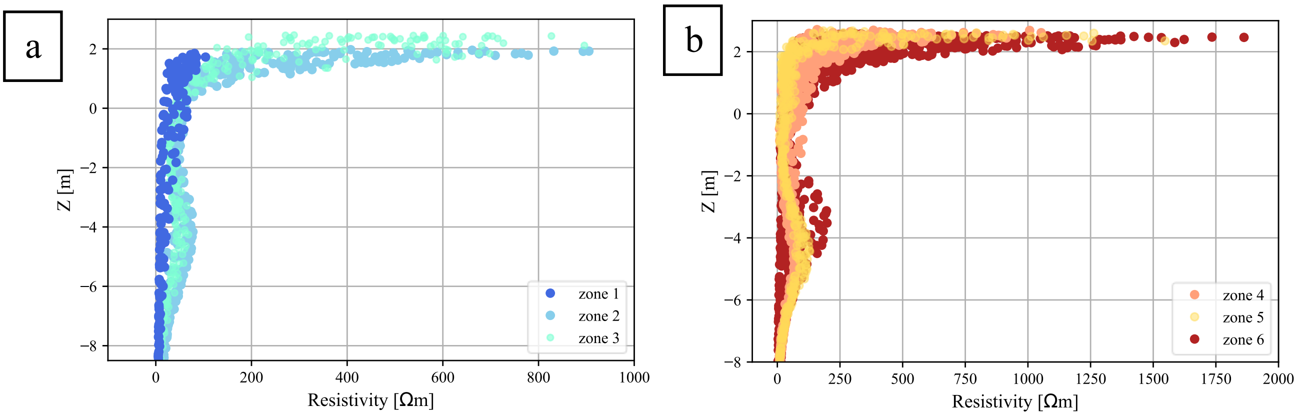

Figure 73: Resistivity [Ω·m] in function of elevation (Z) for the 6 zones (profile R6): (a) zones 1, 2 and 3, (b) zone 4, 5 and 6

A more resistive lens is observed in Zone 6, around 4 m below sea level, and is characterised by resistivity values reaching approximately 240 Ω·m. Additional resistive lenses are also visible elsewhere on the profile.

<u>R7 interpretation</u>

Profile R7 is located to the south of profile R6. The classification result is shown in Figure 74. The anthropogenic deposits, however, reach greater depth than the two previous profiles, particularly in the southern part of the profile.

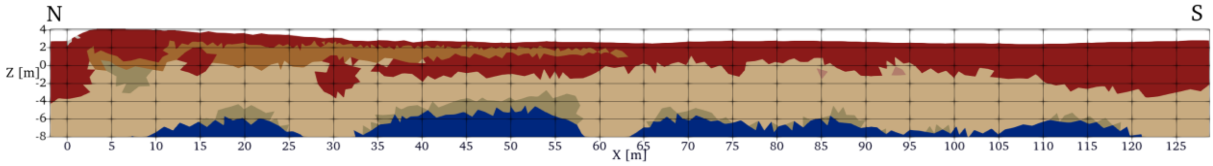

Figure 74: Classification of the first 10 m for profile R7

In Figure 75, four areas were delineated using the satellite image.

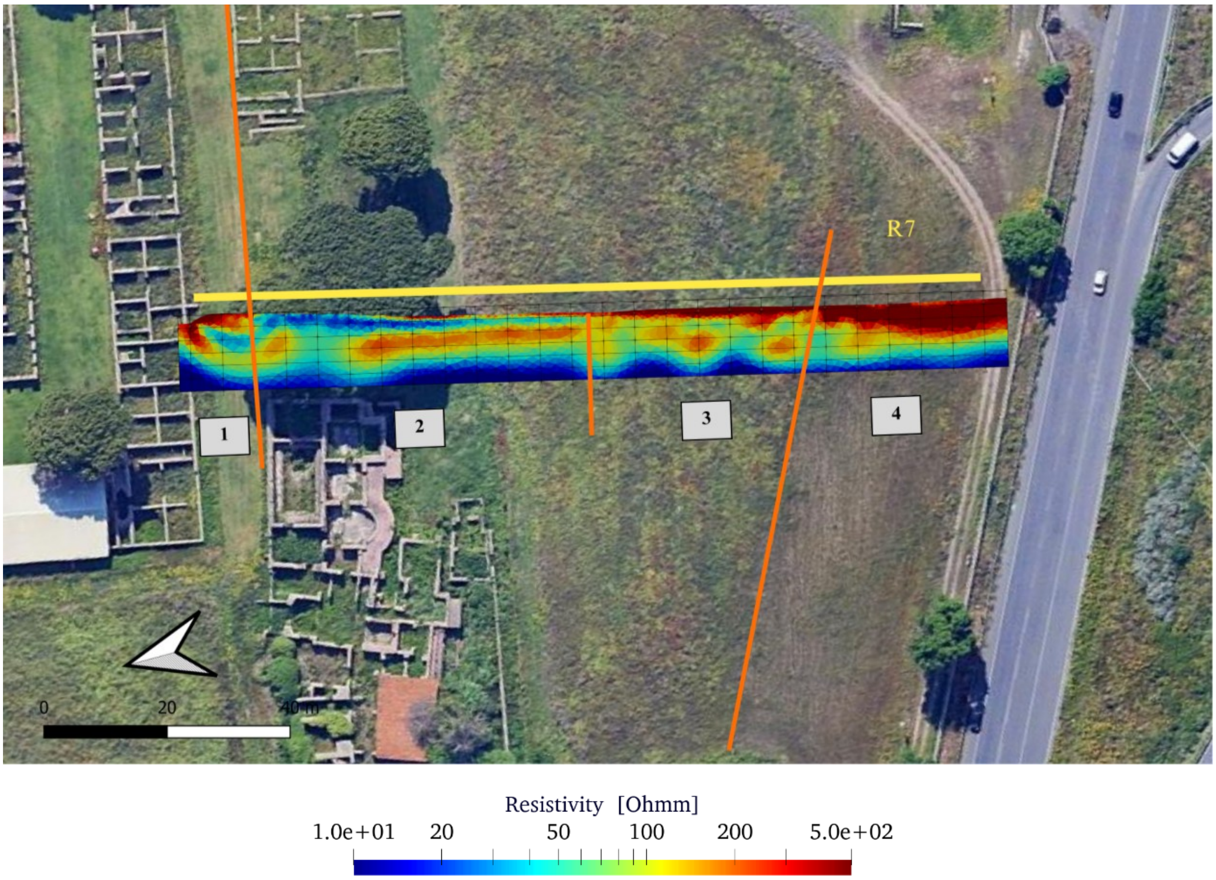

Figure 75: Map shown the correlation between the inversion of R7 and the satellite image (RRMS = 5.99% – χ^2 = 1.67 – iterations = 3)

Zone 1 is a highly resistive area (up to 1500 Ω·m) on the top as shown in the graph of Figure 76. Zone 2 is characterised by a more conductive lens between 2 and 0 m, above which a more resistive area can be observed between 35 and 63 m along the profile (Figure 75). This conductive lens is also located beneath stone pines, as observed on profile R6. The observed lower resistivity is likely due to the shading effect caused by the stone pine trees.

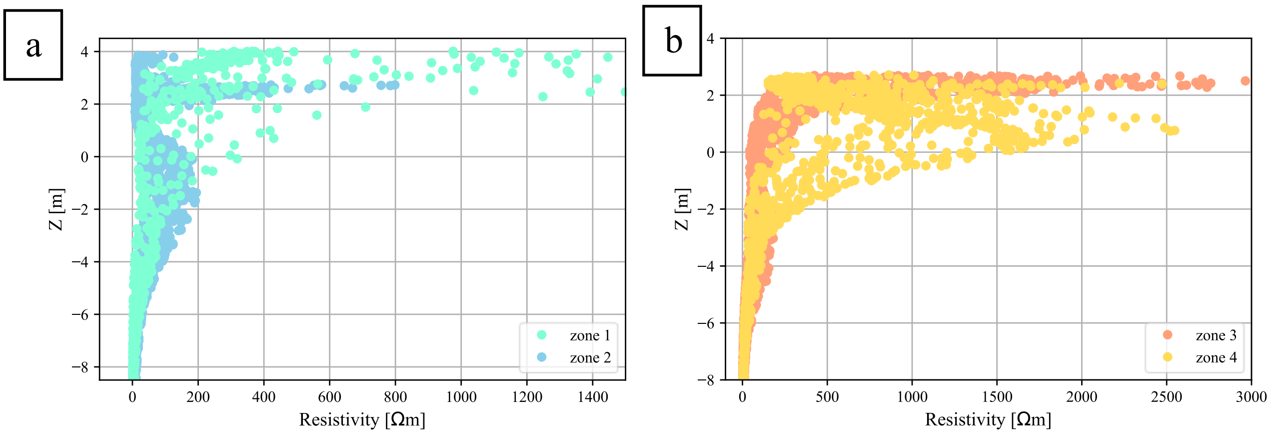

Figure 76: Resistivity [Ω.m] in function of elevation (Z) for the 4 zones (profile R7): (a) zones 1 and 2, (b) zones 3 and 4

Zone 3 is again marked by very high resistivity values at the surface, reaching up to 3000 Ω·m. These values are significantly higher than those observed on other profiles (Figure 76b).

Zone 4 is characterised by high resistivity values that extend deeper. Two modes can be distinguished (Figure 76b). The first mode between 1 and 3 m in elevation, is most likely characterised by a backfill layer containing numerous anthropogenic deposits, while the second, deeper, likely represents the maximum erosion level.

This boundary can be observed in the satellite image as represented by the line between zone 3 and zone 4 (Figure 75). The northern part of the profile is characterised by a progradation zone, while the southern part corresponds to an erosional zone. The erosion level lies below current sea level.

Most surprisingly, the anomaly extending in depth in isotropic inversion is not visible anymore.

R8 interpretation

Profile R8 is the longest profile carried out and intersects with two other profiles analysed in this section (R10 and R11). For better visibility, it has been divided, Figure 77 shows the northern part of the profile, while Figure 78 shows the southern part.

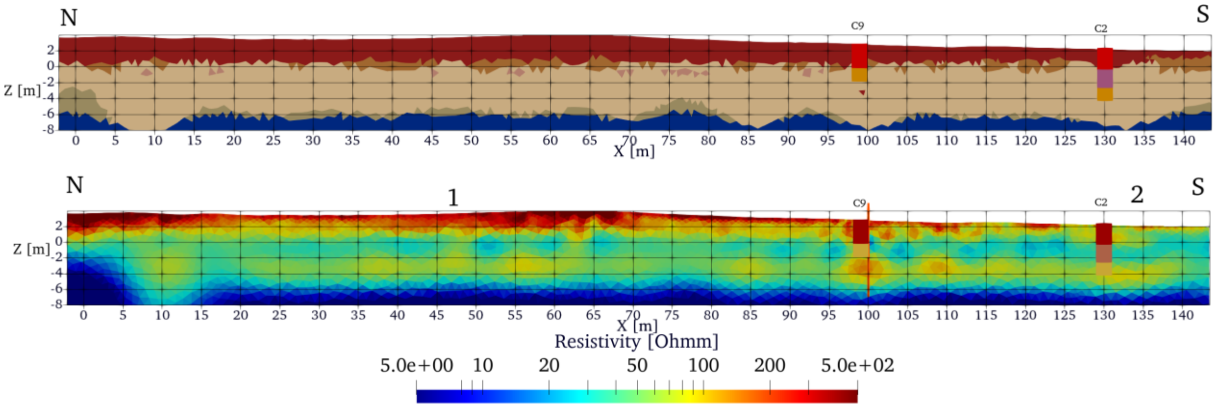

Figure 77: North part of profile R8: interpretation of the first 10 m. (a) Classification, (b) Inversion (RRMS = 5.38% – χ² = 1.47 – iterations = 4)

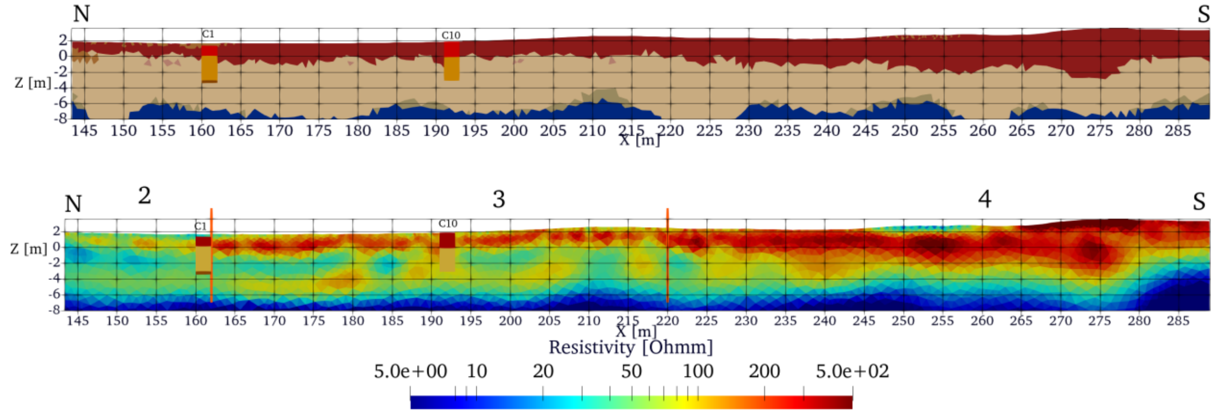

Figure 78: South part of profile R8: interpretation of the first 10 m. (a) Classification, (b) Inversion (RRMS = 5.38% – χ² = 01.47 – iterations = 4)

In the southern part, highly resistive deposits are observed below sea level (Figure 78a).

This profile was acquired in an area where four cores had already been drilled. The inversion shown in Figure 77a and Figure 78a appears to match what was identified in cores C1, C9 and

C10. Core C2 differs from the other three, as anthropogenic deposits are characterised by lower resistivity values.

Zones 2 and 3 represent a depression area and are characterised by lower resistivity values (Figure 79a). Zone 1 is characterised by high resistivity values on the top. Two distinct modes can be identified in Zone 4. The first mode corresponds to higher resistivity values near the surface (Figure 79b). Indeed, Zones 1 and 4 corresponded to more anthropised area than Zones 1 and 2. The second mode is characterised by higher resistivity values at depth, with a resistivity peak of approximately 500 Ω·m just near sea level. The higher resistivity values located around sea level are most likely unsaturated beach sands.

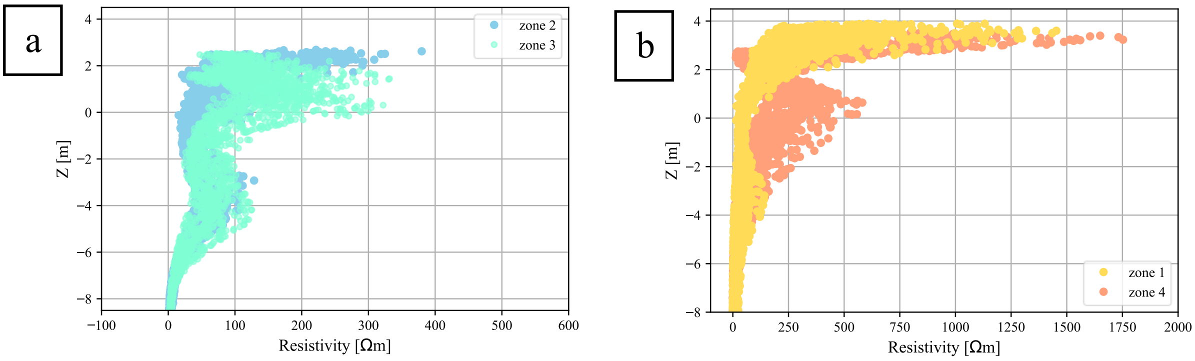

Figure 79: Resistivity [Ω.m] in function of elevation (Z) for the 4 zones (profile R8): (a) less resistive zones, (b) more resistive zones

The resistivity signature at depth is like those observed in the previous three profiles except that some more resistive lenses, reaching up to 100 Ω·m, which are located around 4 m below sea level.

As with the isotropic inversion, the former city wall of Ostia should also be visible in the southern part of the profile, but based solely on the inversion, it is difficult to locate it precisely. However, this wall is clearly visible in the southern part of profile R11 (between 143 and 147 m) and on profile R10 between 90 and 95 m (Figure 80b and Figure 82b).

Moreover, on this profile, the anomaly located between 120 and 140 m along the x-axis in the isotropic inversion is no longer visible here. In fact, between these values, the boundary between the freshwater-saturated (more resistive) and saltwater-saturated (more conductive) deposits is clearly defined. The second anomaly, located between 220 and 230 m along the x-axis, is also not visible. This may indicate that it is located at a greater depth.

R10 and R11 interpretation

These two profiles are divided into three zones. Figure 80 and Figure 82 show classification and inversions results. In both profiles, the central zone is a depression area.

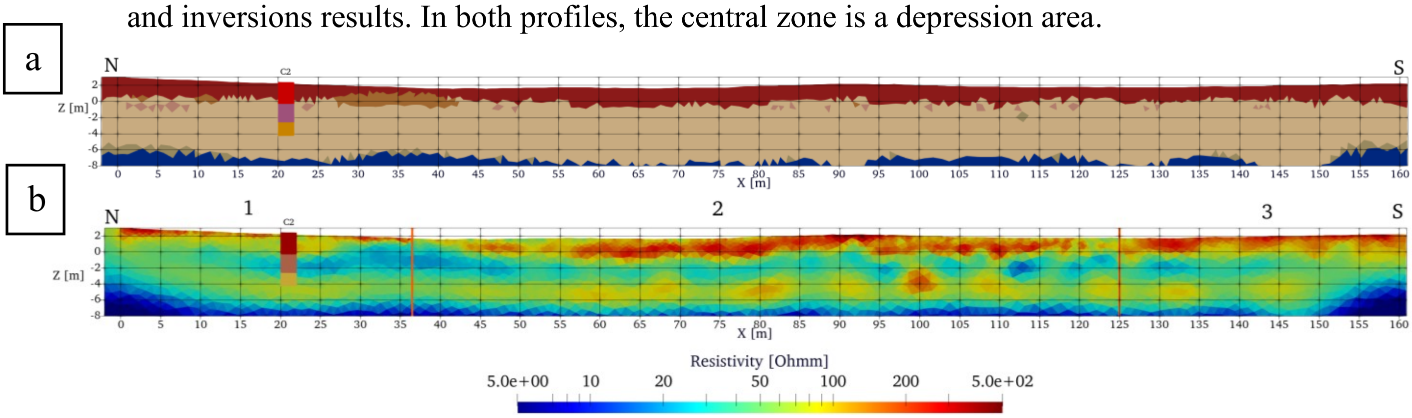

Figure 80: Profile R10: interpretation of the first 10 m. (a) Classification, (b) Inversion (RRMS = 3.68% – χ^2 = 0.70 – iterations = 2)

On this profile, the result of classification shows that the anthropogenic deposits extend approximately to the same depth as in profiles R4-5 and R6. The freshwater-saturated sands extend to 6 to 8 m below the sea level. (Figure 80a).

As on profile R8, the anthropogenic deposits identified in core C2 are characterised by lower resistivity values (Figure 80b). This may indicate either that there are fewer deposits at this depth or that the sediments are already water-content. The anthropized clay lens is clearly visible in the inversion results (Figure 80b) but is not well classified (Figure 80a).

Profile R10 is characterised by lower surface resistivity values compared to the other profiles as can be seen in the graph of Figure 81. The resistivity peak at 500 Ω·m identified in the graph for Zone 2 appears to correspond to the former city wall. This profile does not contain a significant number of archaeological deposits. For R10, the more resistive layer in Zone 2, just above sea level, is maybe some unsaturated sand as observed on R8.

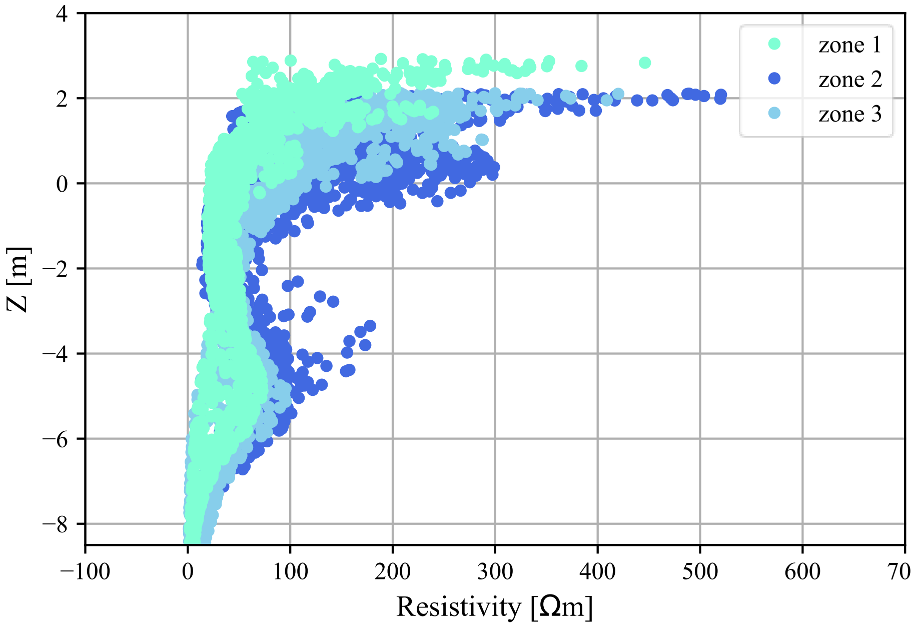

Figure 81: Resistivity [Ω.m] in function of elevation (Z) for the 3 zones (profile R10)

Between 4 and 6 m below sea level, higher resistivity values are observed. At this depth, the highest resistivity values are found in Zone 2 and correspond to the anomaly already observed in the isotropic inversion. However, with the anisotropy factor, this anomaly is smaller and no longer extends.

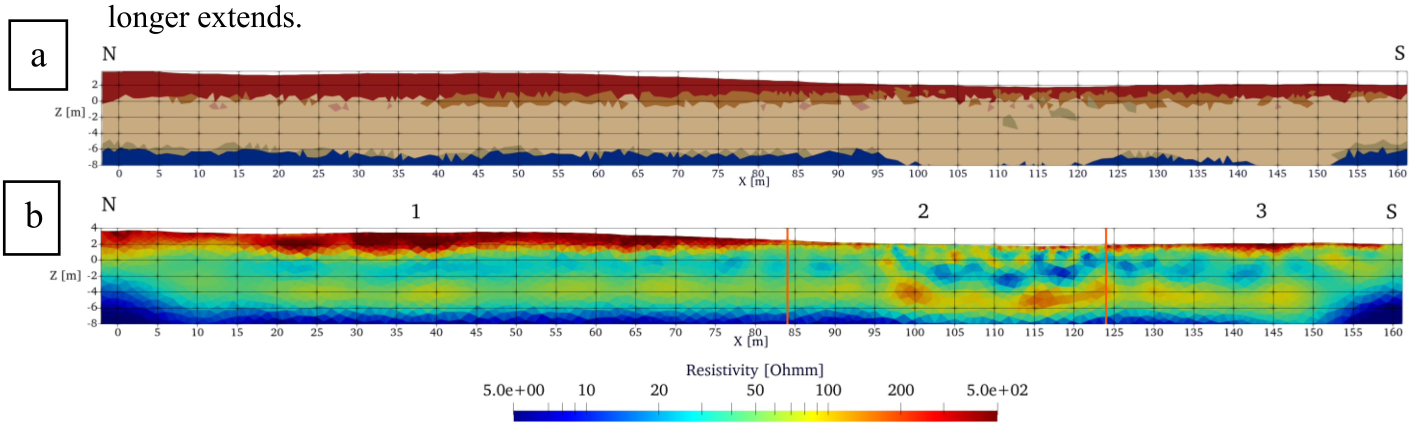

Figure 82: Profile R11: interpretation of the first 10 m. (a) Classification, (b) Inversion (RRMS = 4.99% – χ^2 = 1.26 – iterations = 4)

For profile R11 (Figure 82), a more resistive zone can be observed in the northern part (zone 1) as shown in the graph of Figure 83. A cluster of higher resistivity values can be distinguished between 2 and 3.5 m in elevation, with values ranging from 180 to 100 Ω·m.

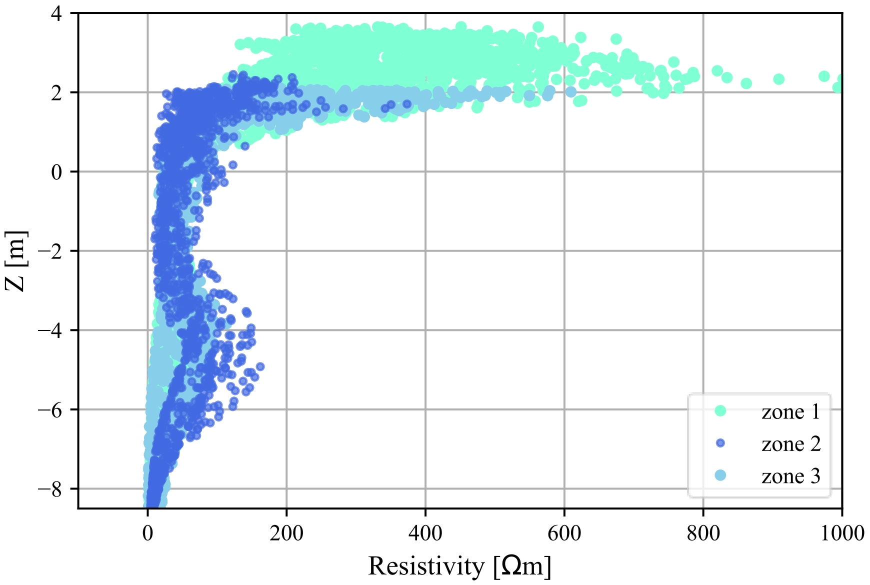

Figure 83: Resistivity [Ω.m] in function of elevation (Z) for the 4 zones (profile R11)

In Zone 2, which also corresponds to a depression area, the resistivity values are similarly low as for profile R10. In Zone 3, the surface deposits have resistivity values between those of Zones 1 and 2 (between 200 and 600 Ω·m). As for profile R10 and R8, higher resistivity values are observed between 4 and 6 meters below sea level and the anomalies are also visible but smaller.

In general, the values of resistivity for profile R10 and R11 are lower than those observed on the other profiles. It is also noteworthy that, in the graphs of these two profiles, the low resistivity values typical of the deeper layers are not observed near the surface.

5.7. 3D representation

The anomalies identified on profiles R10 and R11 appear to be confirmed. To better understand their presence at depth, a 3D visualisation will be carried out for the southern area of Ostia Antica (Figure 84).

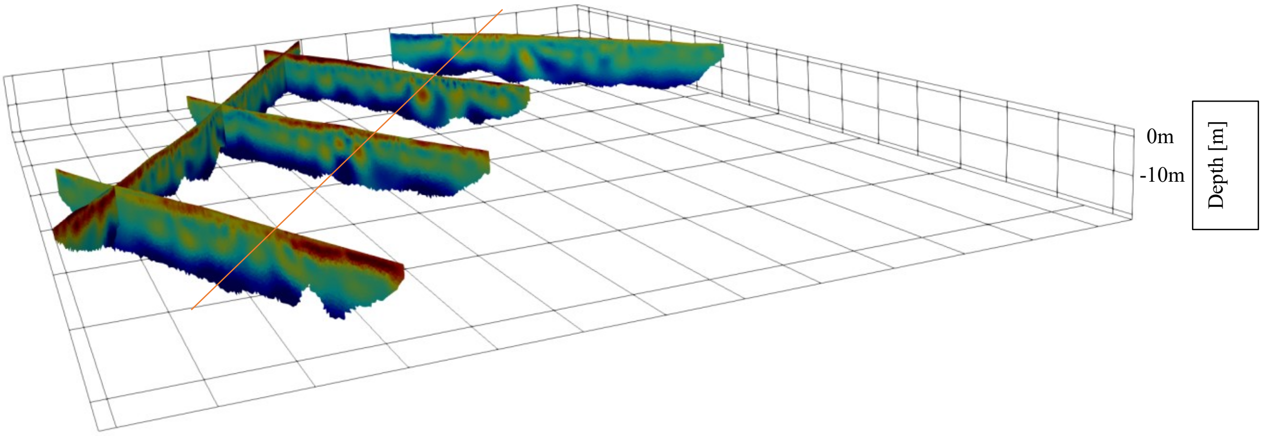

Figure 84: 3D representation of ERT profiles

The resistive anomalies observed on these profiles seem to be align. It should also be noted that profiles R8 and P7 were not acquired at the same time, which could account for the differences in resistivity observed in the top three m.

5.8. Discussion about results

According to the classification results, the archaeosphere appears to extend up to the current sea level, which seems consistent since the Roman sea level was about one meter below the present level. However, based solely on the inversion results and assuming that only very high resistivity values are associated with the archaeosphere, it would be located two meters above current sea level. In fact, it seems to exhibit high resistivity values near the surface, followed by lower resistivity values between 2 and 0 m. These lower resistivity values could be explained by an unsaturated soil containing fewer anthropogenic deposits than those near the surface. The introduction of an anisotropy coefficient made it possible to delineate the freshwater–saltwater interface more clearly around 6-8 m below sea level. Freshwater-saturated sands are characterised by resistivity values around 50 Ω·m. Saltwater-saturated sands are characterised by resistivity values below 5 Ω·m. This analysis is consistent with the ERT results discussed in the state of the art. However, with geophysical analysis alone, it is not possible to date the sands. To better characterise the archaeosphere, a smaller electrode spacing would be required.

By examining the different inversions, the origin of the anomalies observed in the isotropic inversions are difficult to explain. Furthermore, according to the anisotropic inversions over the first 10 meters, the anomalies are still present in profile R10 and R11 but are smaller, less resistive and do not extend horizontally and vertically. More surprisingly, the analysis of the graphs from all profiles reveals that the resistivities associated with the identified anomalies are in fact only slightly higher than those of other resistive lenses observed on different profiles. For profile R7 and R8, if the anomalies exist, they are located at greater depth.

6. Perspectives: methods to integrate into the probabilistic approach

As mentioned in Section 2, Electromagnetic Induction (EMI) and seismic wave analysis are also methods used in archaeological geophysics. To improve the results of the classification, it would be interesting to integrate the results of these two methods in a subsequent analysis. For now, a brief analysis of the data will be carried out for each method.

6.1. EMI data processing and results

The EMI data were taken with a ‘Geosensors R6’. The operating frequency is approximately 9 kHz (specifically 8.4, 8.7 and 9.3 kHz). These are equalised to deliver a uniform output but uncalibrated. Thus, interpreting the apparent conductivity data is challenging and only variations between different zones can be observed. It is also not possible to compare the scales of two different zones, as they may not have been measured under the same conditions. The device used consists of six coils and the HCP (High Co Planner) mode is used. An effective depth is associated to each coil as represented in Table 11.

Table 11: Effective depth for each coil

Coil	Effective depth [m]
0.5	0.8
0.7	1
0.9	1.35
1.1	1.7
1.5	2.3
1.95	2.9

ERT profiles are located within three of their study zones. Zones 2 and 3 are the most relevant for us, as they can be correlated with profile R7 for zone 2 and profiles R8, R9 and R10 for zone 3. These are the profiles for which interpreting the data is the most challenging.

By analysing the zones individually, the ancient city wall is visible in zone 3 (Figure 85). The anomaly in profile R10 and the southernmost anomaly in profile R8 both appear to be located beneath it. It is also possible to observe a more conductive zone extending from west to east, intersecting all three profiles (R10, R11 and R8). This zone seems to correspond to the depression area visible in the topography of the profiles. Interestingly, the two anomalies in profile R11 are situated on either side of this depression zone. The southernmost and northernmost zone is more resistive and corresponds to an area with archaeological deposits.

Regarding zone 2, it is possible to identify a more conductive area in the north-east, which corresponds to the highly conductive lens observed in profile R7. By focusing on the surroundings of profile R7, the boundary between the erosional zone (to the south) and the progradation zone (to the north) is also visible, as was observed in the inversion of profile R7. In the western part of the zone, archaeological remains are clearly visible, corresponding to the more resistive lines.

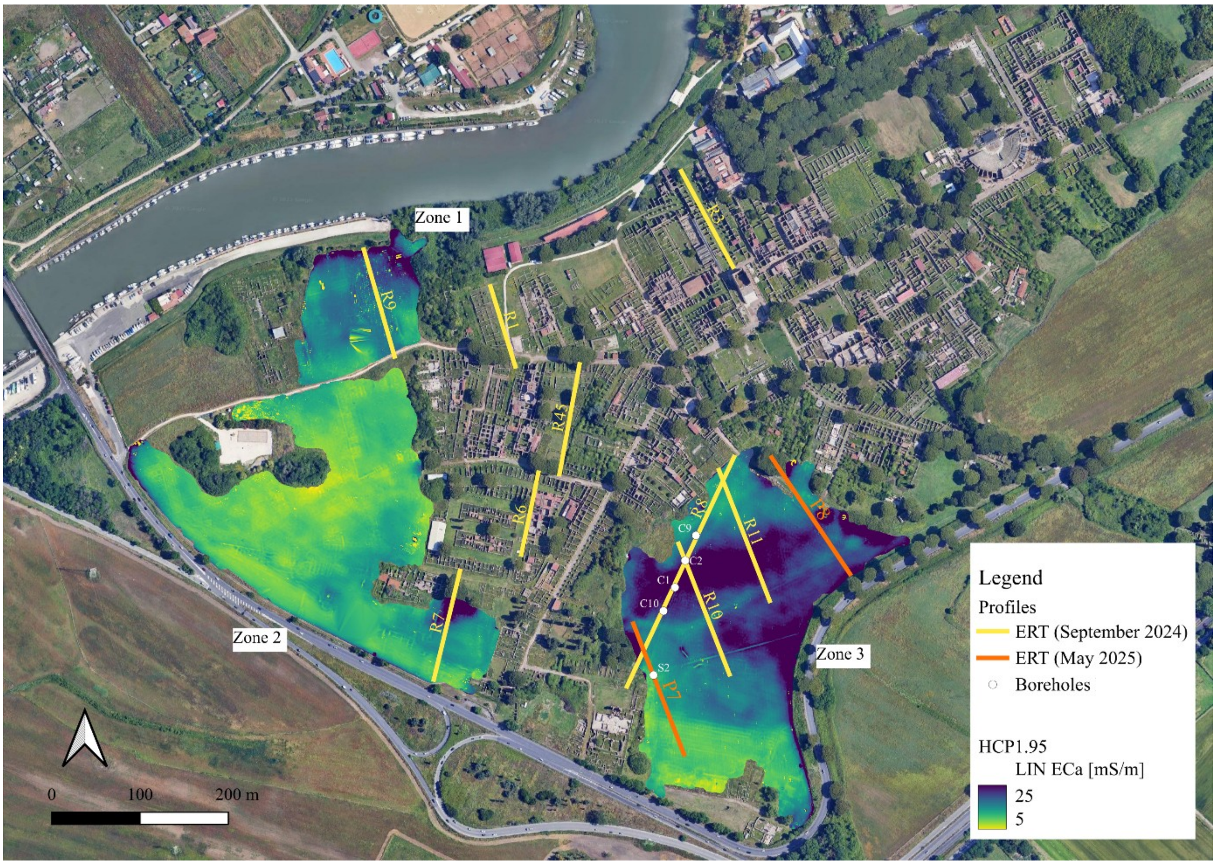

Figure 85: EMI mapping modified after Google satellite

Since the ERT profiles are positioned within the areas scanned by the EMI, they have been used in an attempt to calibrate the EMI data. To do this, the apparent resistivity values must be converted into apparent conductivity values for the depths investigated by the EMI. However, due to the electrode spacing of one metre and the minimum distance between the current electrodes (A and B) being nine metres, it is difficult to isolate apparent resistivity values at very shallow depths.

An alternative approach is to investigate whether a correlation exists between the resistivity values obtained through ERT and the apparent conductivities measured via EMI. Unfortunately, the correlation between these datasets is weak (Figure 86), making it difficult to adjust the EMI values using the ERT profiles. This discrepancy could be attributed to the fact that the ERT and EMI surveys were conducted during different periods, likely under varying weather conditions.

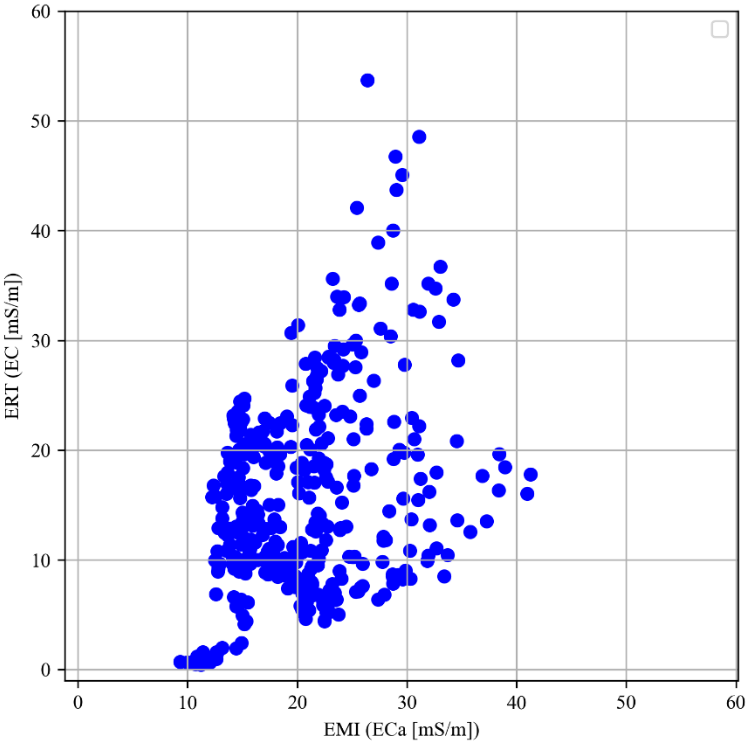

Figure 86: Scatterplot to compare ERT conductivity and EMI apparent conductivity (ECa)

Nevertheless, it has been possible to classify the EMI data for Zone 3, owing to the presence of boreholes C1, C2, C9, C10 and S2. The classification was performed using the deepest coil (HCP1.95). However, this classification is less robust than that based on ERT data, as only five data points were available to establish the prior. Furthermore, the prior was determined using apparent conductivity as the unique variable. Prior probabilities are represented in Table 12.

Table 12: Prior probabilities for the EMI data classification

Category	Description	Probability
1	Anthropogenic deposits + Silt	0.40
2	Anthropized clay	0.20
3	Sand	0.40

The result of classification is shown in Figure 87. The position of cores is also shown.

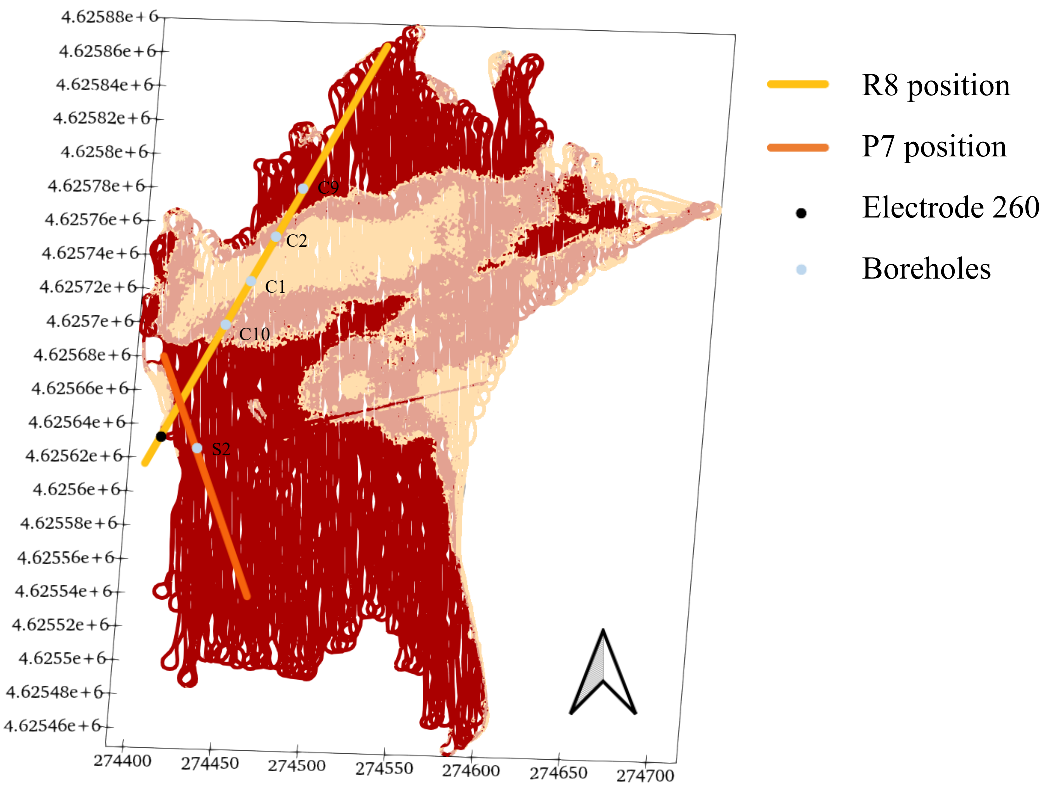

Figure 87: Results of classification with EMI data

To improve the robustness and reliability of the EMI classification, a greater number of reference data points would be necessary. Additionally, performing an inversion of the EMI data would help to obtain a depth-resolved conductivity model, improving the interpretation of subsurface features and enhancing the distinction between different material layers.

The inversion of EMI data would allow them to be integrated into a classification, which would then be more robust.

6.1.1. Comparison between ERT and EMI classifications

In Figure 88, the dotted line represents the approximate depth of the HCP 1.95 coil used for the classification. This allows for a comparison between the classification based on the inversion of electrical data and that based on the EMI data.

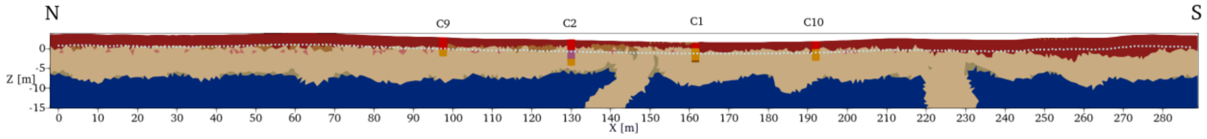

Figure 88: Representation of the intersection between the EMI data and ERT data (profile R8)

The cores collected along profile R8 have been mapped onto the classifications to provide some points of comparison and to better position us along the profile. The analysis of cores C9 and C1 aligns well with both classifications. The EMI-based classification accurately represented the anthropized clay deposits near core C2, unlike the classification derived from the ERT data.

The same analysis was conducted for profile P7 (Figure 89). For this profile, the analysis of core S2 matches both the ERT and EMI classifications.

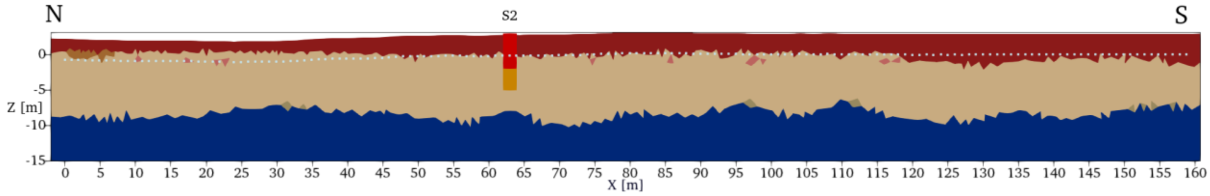

Figure 89: Representation of the intersection between the EMI data and the ERT data (profile P7)

Moreover, although the EMI classification does not perfectly match the ERT classification, major anthropogenic zones can still be identified. Anthropogenic clay, however, appears overrepresented in the EMI classification. This can be explained by the disproportion in class percentages: in the ERT dataset, it accounts for only 2.1%, whereas in the EMI classification it represents 20%.

It is important to remain cautious when comparing EMI and ERT classifications. The signal from an EMI coil is influenced by all the layers it penetrates, not just the one corresponding to its effective depth of investigation. Thus, although the deepest coil mainly reflects the properties of the deeper layers due to its higher sensitivity at depth, the overlying, particularly more resistive, layers also have a significant impact on the measurements.

6.2. Surface waves processing and results

It would also be possible to include seismic data, such as surface waves, in the classification. These waves are typically analysed using Multichannel Analysis of Surface Waves (MASW) which is a non-invasive and non-destructive method. It relies on the energy generated by Rayleigh waves, which are surface waves whose dispersion depends on the elastic properties of the subsurface and the offset. The calculation of the dispersion curve is one of the key steps. It represents the phase velocity as a function of frequency. Then, an iterative inversion process is performed to derive the shear-wave velocity (V_s) profile as a function of depth (Park et al., 1999).

The map shown in Figure 90 indicates the location of the two seismic profiles carried out along the alignment of profile R8, each profile measures 47 m. 5 shots are taken and then an average is done. For the analysis of surface waves, only the shots carried out at the ends of the profiles are considered. As already mentioned, these shots are performed 5 meters from the first (or last) geophone. For profile S_1 (see Figure 90), which intersects the old wall, both the forward and reverse shots could be analysed. However, for profile S_2 (see Figure 90), only the forward shot was usable, as the data from the reverse shot could not be processed.

Figure 90: Position of the studied seismic profiles modified after Google satellite

To be analysed, the field data must be inverted. The inversion process begins with the analysis of velocity spectra where multiple modes may be observed. Among these, the fundamental mode is generally considered, as it carries the most energy and is often the most clearly identifiable. The velocity spectra are realised with the Geopsy[5] software. The dispersion images were created using a wavefield transform method, specifically the frequency–wavenumber (f–k) transform. This method converts the recorded seismic signals from the time–space domain into the frequency–wavenumber domain, allowing the separation of different propagation modes and the identification of the fundamental mode by visualising how phase velocity varies with frequency.

Dispersion is the phenomenon where the phase velocity of a wave depends on its frequency. In the context of surface waves, different frequencies penetrate to different depths in the subsurface, so analysing dispersion provides information about the variation of shear-wave velocity with depth. To create a dispersion curve, values are picked from the velocity spectra. These picked points form the dispersion curve, which is then used as input for an inversion process to derive the subsurface shear-wave velocity profile.

The most energetic area is the purple one in Figure 91 and Figure 92, which is why the picking is denser in this area. The signal is also less noisy when, for a given frequency, the velocity interval associated with the highest energy is narrow. The profile with the best interference figure is the forward shot of profile S_1, as it is less dispersive per frequency interval and less energy above fundamental mode.

---

[5] Wathelet, M. (2008). *Geopsy: Software for geophysical analysis* [Computer software]. Université de Liège. http://www.geopsy.org

In general, each profile is characterised by lower velocities and does not exhibit a wide range of velocity values.

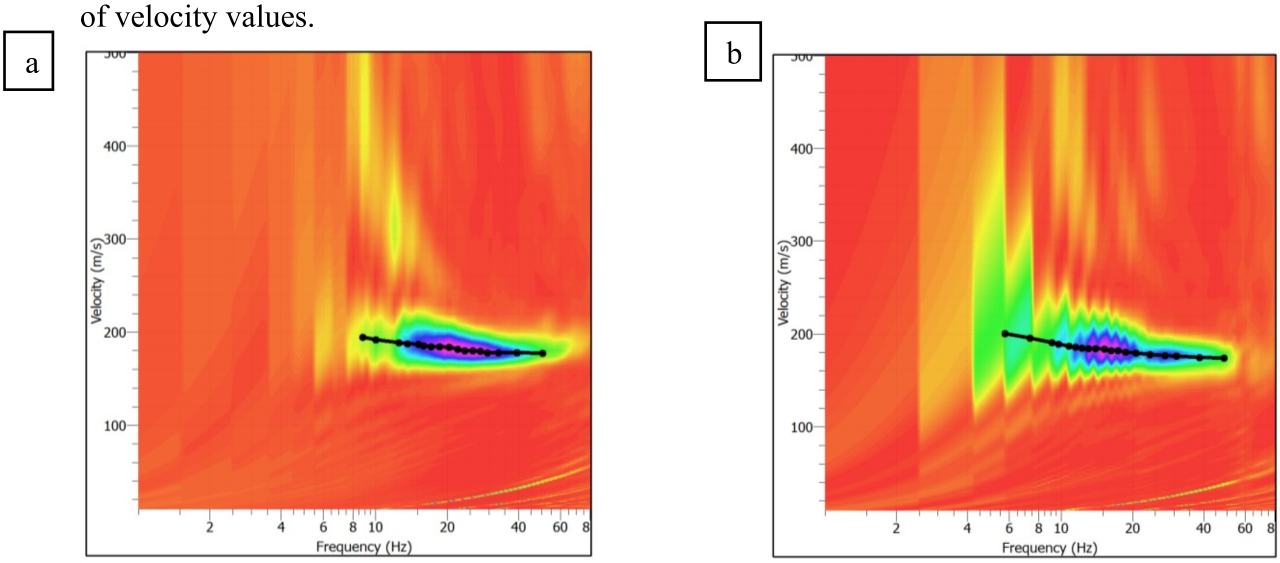

Figure 91: (a) Velocity spectrum of the forward shot, (b) Velocity spectrum of the reverse shot for profile S_1

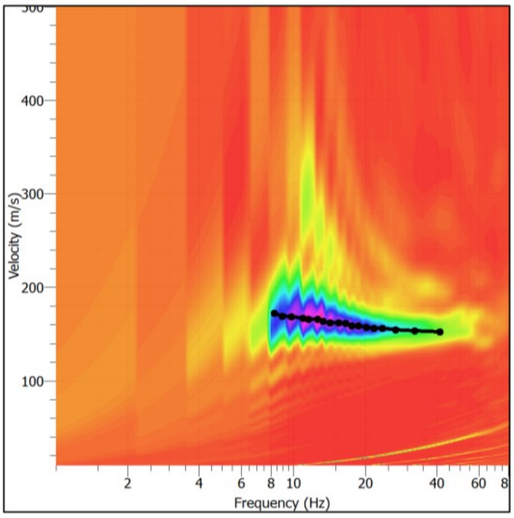

Figure 92: Velocity spectrum of the forward shot (Profile S_2)

It is then possible to invert the data using a deterministic approach using the Disba[6] packages in python. The objective of the data inversion is to determine the characteristics of the subsurface using defined parameters. In the case of the study of Rayleigh waves, the parameter to be determined is the shear wave velocity V_s over depth.

The purpose of the deterministic approach is to minimise the difference between the velocities picked and the phase velocities obtained after inversion. Before performing the inversion, the following parameters must be defined: the thickness, the compression wave velocity (V_P), the shear wave velocity (V_S) and the density of each layer. Thanks to the longest wavelength, it is possible to approximate the investigation depth. This depth is equal to one third or one half of

---

[6] Luu, K. (2021). *disba: Numba-accelerated computation of surface wave dispersion* [Logiciel]. Zenodo. https://doi.org/10.5281/zenodo.5733451.

the maximum wavelength λ_{max}, which here is equal to 22 m. The investigation depth is therefore between 7.33 and 11 m.

A theoretical model can then be defined, composed of four layers. These four layers were determined based on the core analysis (especially from core C2 located in the middle of seismic profile S8_2). The first layer is 2.5 meters thick and corresponds to anthropogenic deposits, the next one is 2.2 meters thick and represents the anthropized clay, the third layer is 5.8 meters thick because the investigation depth is 11 m. Finally, the fourth is considered as a half-infinite space. These thicknesses are fixed.

The inverse parameter is the shear wave velocity (V_S), firstly, for each layer, a plausible value is determined by trial and error.

The compression wave velocities (V_p) must also be fixed but they have little influence on the inversion result. However, they must always be higher than the shear wave velocities (V_s). It is therefore arbitrarily set that: $V_p = 2*V_s$.

The density of the layers must also be set. Although it has little influence on the result as well, realistic values were chosen for each layer. The parameters for each layer are shown in Table 13.

Table 13: Parameters of the inversion

	Thickness [m]	V_p [m/s]	V_s [m/s]	ρ [kg/m^3]
Layer 1	2.5	340	170	1800
Layer 2	2.2	440	220	1900
Layer 3	5.8	600	300	2000
Layer 4	∞	700	350	2100

The regularisation factor λ was set to 0.05 for all layers. The theoretical model was constructed to best fit the picked curves.

Using this model, the dispersion curves (Figure 93a) and the graph showing the evolution of velocity with depth (Figure 93b) can be plotted for the forward shot of profile S_1.

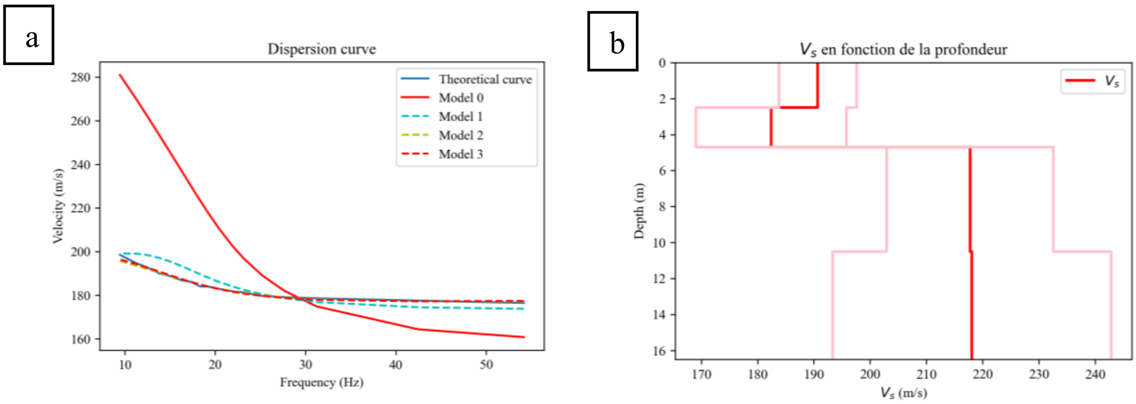

Figure 93: Results for the forward shot of profile S_1 (a) Dispersion curve (error = 2.9 m/s), (b) V_s in function of depth.

This first profile converges after 3 iterations. The results for the forward shot of the profile crossing the wall as shown in Figure 93. The shear wave velocities vary between 182.40 m/s and 218.08 m/s. A significant velocity jump occurs at a depth of 4.9 meters, which likely indicates the presence of a second medium, consisting of sands saturated with freshwater, according to the analysis of the ERT data.

Figure 94 shows the results for the reverse shot of profile S_1.

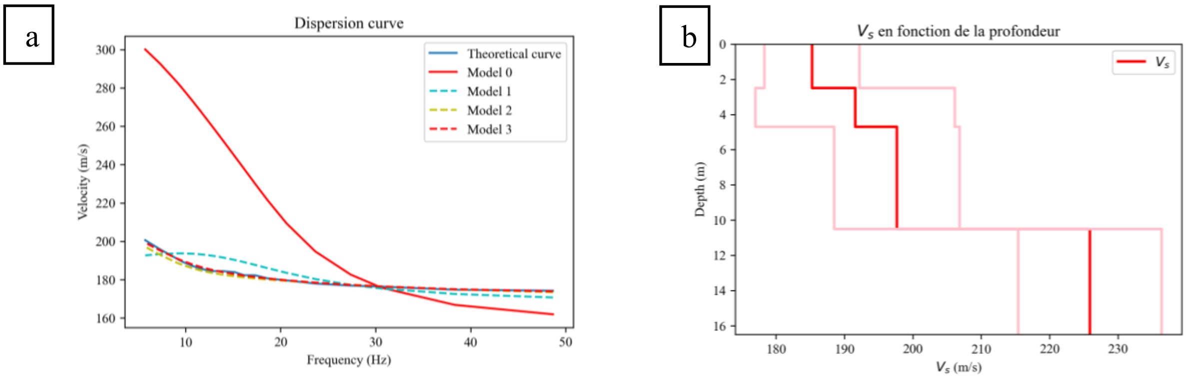

Figure 94: Results for the reverse shot of profile S_1 (a) Dispersion curve (error = 2.7 m/s), (b) V_s in function of depth.

The reverse shot also converges after 3 iterations. The V_s range from 185.86 m/s to 224.64 m/s and increase with depth, unlike the forward shot. At a depth of 4.9 meters, there is not jump, while a jump at 11 meters is visible. This may correspond to an environment that could not be determined using the forward.

The last profile is visible in Figure 95.

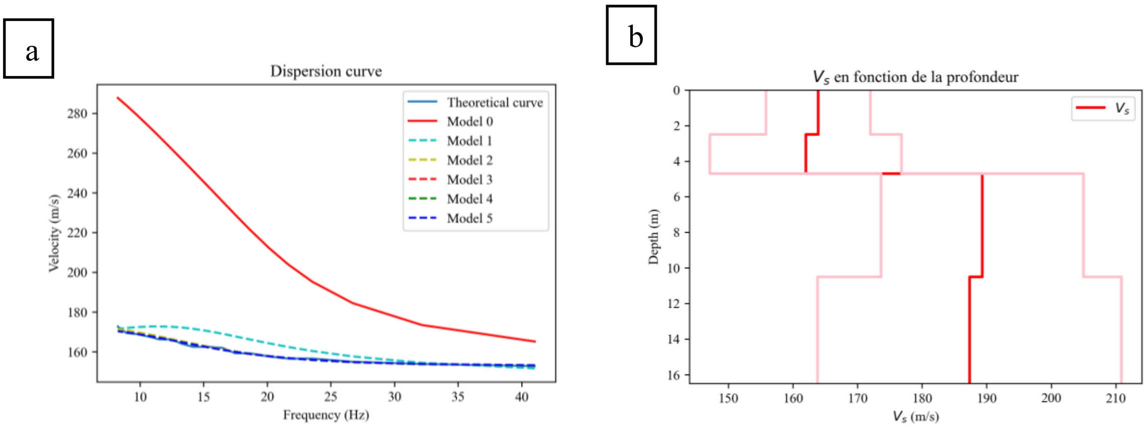

Figure 95: Results for profile S_2 (a) Dispersion curve (error = 3.3 m/s), (b) V_s in function of depth.

For this profile, only the forward shot could be analysed. Although the reverse shot was performed, the corresponding file contained no usable waveforms. For this profile, convergence was achieved after 5 iterations.

The shear wave velocities (V_S) range from 163.43 to 189.41 m/s. The velocities obtained through inversion are lower than those observed in profile S_1. This was expected, since the picked velocities are lower.

However, as with the forward shot of profile S1, a velocity jump is observed at 4.9 m, which supports the hypothesis that a second medium begins at this depth.

The two pink lines surrounding the red line represent the possible margin of error associated with the uncertainty in the picking process. Indeed, on the interference figures, a range of phase velocities is associated with each frequency, introducing an uncertainty in the picked phase velocities. This uncertainty propagates into the shear wave velocities derived from the inversion process, making it difficult to assign a precise V_s value to each layer.

6.2.1. Comparison between ERT and surface waves

To compare the electrical inversion with the inversion based on surface waves, the graphs showing the variation of V_s with depth (white lines, in x axis, 1 m corresponds to 1 m/s) were superimposed on the inversion obtained from the starting model defined through the classification, as shown in Figure 96.

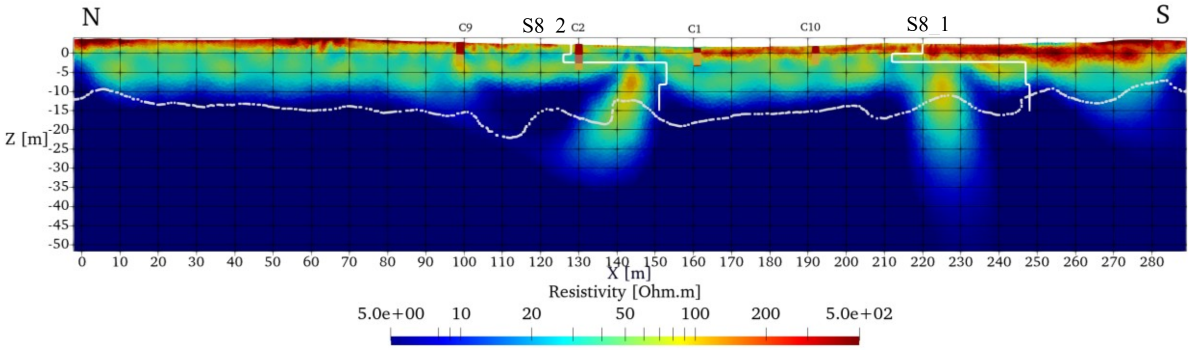

Figure 96: Synthesis of inversed data

When comparing the two seismic profiles based on the results of the electrical inversion, the velocity variations in profile S8_1 correspond more to the resistivity variations observed in the electrical inversion. According to the results, the surface-wave analyses do not allow the identification of the anthropized clay layer. This can be explained by the fact that it is not present across the entire profile.

With this analysis, the freshwater and saltwater-saturated layers do not appear to be distinguishable through surface-wave analysis. Caution must be exercised when interpreting this result, as the inversion strongly depends on the chosen starting model. The model used here is highly simplified and serves only as a preliminary approach. It would be useful to perform an inversion that also allows the depth to vary, to verify whether the imposed value is too restrictive. Furthermore, in the perspective of a future classification, it would be relevant to construct histograms representing the range of velocities associated with each layer.

7. Conclusions and perspectives

The main objective of this thesis was to integrate different data sources with the collected electrical resistivity data to reduce the ambiguity associated with the inversion process. To further improve the interpretation of the site, it was also useful to process additional methods.

Isotropic inversions were first carried out, providing an initial understanding of the palaeoenvironment of the Ostia site. However, some disturbing anomalies were observed on certain profiles, highlighting the need for additional constraints to refine the inversion. To address this, results of Dynamic-Penetrometer Electrical-Conductivity (DP-EC) and core samples were integrated into the inversion process. The DP-EC results were used to perform a constrained inversion using a geostatistical approach. With this method, anomalies do not extend deeply but are flattened. The inversion constrained by a fixed correlation length is, in this case, not very relevant because a fixed and small correlation length is too restrictive. It would be necessary to try imposing a variable correlation length depending on the different zones of the studied environment. To achieve this, the correlation length should be determined based on data collected on-site, rather than being set at 1 km as is currently the case. Information from the drilling cores was used to define structural boundaries. This method was also not very conclusive because the interface on the selected profile was short compared to the total length of the profile. However, it worked well in the investigated area of the profile, so it would be interesting to apply it further if additional drillings are conducted.

The main part of this master thesis was the probabilistic approach carried out by integrating ERT data along with the results from boreholes and DP-EC tests. The probabilistic approach used was effective in classifying inversion results and facilitating the attribution of zones to specific lithologies or types of deposits. The classification helps to delimitate the archaeosphere and the delimitation between freshwater and saltwater saturated zone. It has also made possible to rule out the hypothesis of an anthropogenic origin for the deep anomalies observed in profiles R7, R8, R10 and R11. However, the conductive zones observed near the surface, for example, on profiles R7, R6 or P8 are poorly classified. They are categorised as sand + silt, but this is simply because these zones are located beneath stone pines and are therefore in the shade.

The issue with the probabilistic approach is the overlap between PDFs in ERT classification. Indeed, the first five meters are characterised by highly variable resistivity values, therefore, the PDF of anthropogenic deposits is characterised by a huge standard deviation and overlap the other PDFs. Another overlap is particularly noticeable in the resistivity PDFs. In fact, the mean resistivity for the “sand” category and that for the “anthropized clay” category are almost identical, which makes it difficult to distinguish between them. Moreover, since sands are more probable, they tend to override the anthropized clays. For an optimal classification, the PDFs for each category should be significantly different. Additional drilling would be necessary to improve the reliability of the classification. In fact, some additional measurement points would be useful to improve the probability of the category assigned to each cell. Moreover, performing an inversion with a smaller electrode spacing would improve the near-surface resolution. This could then make it possible to distinguish certain deposits within the anthropogenic zone, as observed in the core samples.

The prior probabilities determined for the classification of ERT data are also slightly biased because the DP tests are deeper than the boreholes carried out in the study area. Furthermore, these DP tests were not conducted directly in the study area but rather in a former meander of the Tiber, where silts occur at greater depths, something not observed in the boreholes, except in borehole Cat-3.

The classification of EMI data produced results generally consistent with those from ERT data, except for an overestimation of the percentage of anthropized clay. This difference is explained using only five contact points for the EMI classification, making the prior probabilities less precise than those for ERT.

To perform a classification integrating both ERT and EMI data, it would have been necessary to calibrate the EMI data using the ERT data and then invert them. However, the one metre spacing between electrodes does not allow isolating the apparent resistivity values from the ERT profiles needed to calibrate the EMI.

Regarding the seismic data, to insert them to the classification, a histogram of shear wave velocities identified by zone or layer would be required.

For the interpretation, the cross-analysis of the data revealed that the thickness of the archaeosphere ranges between 3 and 4 m and thus appears to extend from the topographic surface down to the current sea level. The interface between the freshwater and saltwater aquifers is located at approximately 11 m below the topography. The results support previous research and provide new insights. For the profiles near the Tiber, the boundaries between the fluvial deposits and the littoral deposits could be observed on profile R3, the one closest to the Tiber. This boundary was located after the 60th electrode, thus at least 120 m from the Tiber.

As for the anomalies, they appear disproportionate. Indeed, isotropic inversions reveal anomalies extending significantly in depth for profiles R7 and R8. However, their vertical extent is reduced when classification is applied. Finally, when the inversion is restricted to the first ten meters and an anisotropy factor is introduced, these anomalies disappear, if they exist, they are located at greater depth.

To further the study, it would be relevant to carry out additional ERT profiles with higher vertical resolution and deeper boreholes to investigate more precisely the anomalies observed on profiles R7, R8, R10, R11, P7 and P8. Other drilling near the Tiber would also provide more information regarding the lateral boundaries of the different types of deposits. However, such investigations remain costly.

8. References

Argote-Espino, D. L., Juárez-Osnaya, A., & García-Serrano, A., 2022. Finding evidence of an ancient platform through magnetometry in Huexotla, Central Mexico. *Archaeological Prospection*, *29*(2), 305-315. https://doi.org/10.1002/arp.1853.

Binley, A. & Kemna, A., 2005. DC Resistivity and Induced Polarization Methods. In: Rubin, Y., Hubbard, S.S. (eds), *Hydrogeophysics. Water Science and Technology Library, vol 50*. Springer, Dordrecht. https://doi.org/10.1007/1-4020-3102-5_5.

Binley, A., & Slater, L., 2020. *Resistivity and Induced Polarization: Theory and Applications to the Near-Surface Earth*. Cambridge University Press. https://doi.org/10.1017/9781108685955.

Blanchy, G., McLachlan, P., Mary, B., Censini, M., Boaga, J., & Cassiani, G., 2024. Comparison of multi-coil and multi-frequency frequency domain electromagnetic induction instruments. *Frontiers in Soil Science*, *4*, 1239497. https://doi.org/10.3389/fsoil.2024.1239497.

Capozzoli, L., Giampaolo, V., De Martino, G., Perciante, F., Lapenna, V., & Rizzo, E., 2022. ERT and GPR Prospecting Applied to Unsaturated and Subwater Analogue Archaeological Site in a Full Scale Laboratory. *Applied Sciences*, *12*(3), 1126. https://doi.org/10.3390/app12031126.

Cardarelli, E., De Donno, G., Scatigno, C., Oliveti, I., Martinez, M. P., & Prieto-Taboada, N., 2016. Geophysical and geochemical techniques to assess the origin of rising damp of a Roman building (Ostia Antica archaeological site). *Microchemical Journal*, *129*, 49-57. https://doi.org/10.1016/j.microc.2016.06.006.

Caterina, D., 2014. *Towards a better understanding of time-lapse electrical resistivity properties associated to organic contaminants and bioremediation processes in the subsurface*. PhD Thesis, University of Liège, 311 p.

Caterina, D., Hermans, T., & Nguyen, F., 2014. Case studies of incorporation of prior information in electrical resistivity tomography: Comparison of different approaches. *Near Surface Geophysics*, *12*(4), 451-465. https://doi.org/10.3997/1873-0604.2013070.

Cong-Thi, D., Dieu, L. P., Thibaut, R., Paepen, M., Ho, H. H., Nguyen, F., & Hermans, T., 2021. Imaging the Structure and the Saltwater Intrusion Extent of the Luy River Coastal Aquifer (Binh Thuan, Vietnam) Using Electrical Resistivity Tomography. *Water*, *13*(13), 1743. https://doi.org/10.3390/w13131743.

Dabas, M., 2018. L'archéo-géophysique ou la détection et la cartographie des sites archéologiques. *Annales des Rencontres archéologiques de Saint-Céré*, *25*, 117-124. https://hal.science/hal-02188753v1/document. Consulted on April 12.

Dabas, M., 2024. *La prospection archéo-géophysique. Détection et cartographie non destructives du patrimoine enfoui*. Hermann. https://stm.cairn.info/numero/HERM_DABAS_2024_01.

Dahlin, T., & Zhou, B., 2004. A numerical comparison of 2D resistivity imaging with 10 electrode arrays. *Geophysical Prospecting*, *52*(5), 379-398. https://doi.org/10.1111/j.1365-2478.2004.00423.x.

De Smedt, P., Van Meirvenne, M., Herremans, D., De Reu, J., Saey, T., Meerschman, E., Crombé, P., & De Clercq, W., 2013. The 3-D reconstruction of medieval wetland reclamation through electromagnetic induction survey. *Scientific Reports*, *3*(1), 1517. https://doi.org/10.1038/srep01517.

De Smedt, P., Verdonck, L., Verhegge, J., & Vermeulen, F., 2024. *Interim report of the Ghent University geophysical surveys in 2023 at Ostia Antica (RM, Italy)*.

Delmetz, M., 2024. *Geoarchaeology of Ostia: Multi-indicators study of the urban deposits from the western district of the Roman city*. Master Thesis, University of Strasburg, 61 p.

Di Bella, L., Bellotti, P., & Milli, S., 2013. The role of foraminifera as indicators of the Late Pleistocene–Holocene palaeoclimatic fluctuations on the deltaic environment: The example of Tiber delta succession (Tyrrhenian margin, Italy). *Quaternary International*, *303*, 191-209. https://doi.org/10.1016/j.quaint.2013.04.015.

Eppelbaum, L. V., Khabarova, O., & Birkenfeld, M., 2024. Advancing archaeogeophysics through integrated informational-probabilistic techniques and remote sensing. *Journal of Applied Geophysics*, *227*, 105437. https://doi.org/10.1016/j.jappgeo.2024.105437.

Fassbinder, J. W. E., 2017. Magnetometry for Archaeology. In A. S. Gilbert (Éd.), *Encyclopedia of Geoarchaeology* (p. 499-514). Springer Netherlands. https://doi.org/10.1007/978-1-4020-4409-0_169.

Forte, E., Mocnik, A., Basso, P., Casagrande, G., Martinucci, D., Pillon, S., Possamai, M., & Zambrini, R., 2021. Optimised Extraction of Archaeological Features from Full 3-D GPR Data. *Applied Sciences*, *11*(18), 8517. https://doi.org/10.3390/app11188517.

Gaffney, C., 2008. Detecting Trends in the Prediction of the Buried Past: A Review of Geophysical Techniques in Archaeology. *Archaeometry*, *50*(2), 313-336. https://doi.org/10.1111/j.1475-4754.2008.00388.x.

Giraudi, C., Tata, C., & Paroli, L., 2009. Late Holocene evolution of Tiber River delta and geoarchaeology of Claudius and Trajan Harbor, Rome. *Geoarchaeology*, *24*(3), 371-382. https://doi.org/10.1002/gea.20270. Not consulted.

Guan, J., Li, Y., Ji, R., Liu, G., & Yan, Y., 2022. Love wave full-waveform inversion for archaeogeophysics: From synthesis tests to a field case. *Journal of Applied Geophysics*, *202*, 104653. https://doi.org/10.1016/j.jappgeo.2022.104653.

Hadler, H., Fischer, P., Obrocki, L., Heinzelmann, M., & Vött, A., 2020. River channel evolution and tsunami impacts recorded in local sedimentary archives – the ‘Fiume Morto’ at Ostia Antica (Tiber River, Italy). *Sedimentology*, *67*(3), 1309-1343. https://doi.org/10.1111/sed.12599.

Hellman, K., Ronczka, M., Günther, T., Wennermark, M., Rücker, C., & Dahlin, T., 2017. Structurally coupled inversion of ERT and refraction seismic data combined with cluster-based model integration. *Journal of Applied Geophysics*, *143*, 169-181. https://doi.org/10.1016/j.jappgeo.2017.06.008.

hkex., 2018. *ResIPy* [Computer software]. GitLab. https://gitlab.com/hkex/resipy.

Ibraheem, I. M., Bergers, R., & Tezkan, B., 2021. Archaeogeophysical exploration in Neuss-Norf, Germany using electrical resistivity tomography and magnetic data. *Near Surface Geophysics*, *19*(5), 603-623. https://doi.org/10.1002/nsg.12172.

Isunza Manrique, I., Caterina, D., Nguyen, F., & Hermans, T., 2023. Quantitative interpretation of geoelectric inverted data with a robust probabilistic approach. *GEOPHYSICS*, *88*(3), B73-B88. https://doi.org/10.1190/geo2022-0133.1.

Juncker, J., Salomon, F., Mainet, G., Morard, T., Turci, M., Delmetz, M., & Schmitt, L. (n.d.). *Beach-ridges and swales below urban fabric of Ostia*. Unpublished manuscript.

Rücker, J., Rücker F., & Günther T. Pygimli. https://www.pygimli.org.

Journel, A. G., 2002. Combining knowledge from diverse sources: An alternative to traditional data independence hypotheses: Mathematical Geology, 34, 573–596, https://doi.org/10.1023/A:101604701259. Not consulted.

LaBrecque, D. J., Miletto, M., Daily, W., Ramirez, A., & Owen, E., 1996. The effects of noise on Occam’s inversion of resistivity tomography data. *Geophysics*, *61*(2), 538-548. https://doi.org/10.1190/1.1443980.

Le Gall J., 1953. Le Tibre, fleuve de Rome dans l’antiquité, Paris. Not consulted.

Lee, K. S., & Cho, I. K., 2020. Negative apparent resistivities in surface resistivity measurements. *Journal of Applied Geophysics*, *176*, 104010. https://doi.org/10.1016/j.jappgeo.2020.104010.

Loke, M. H., Chambers, J. E., Rucker, D. F., Kuras, O., & Wilkinson, P. B., 2013. Recent developments in the direct-current geoelectrical imaging method. *Journal of Applied Geophysics*, *95*, 135-156. https://doi.org/10.1016/j.jappgeo.2013.02.017.

Mainet, G., & Graziano, M. S., 2022. *’Ad Ostium Tiberis’: Proceedings of the Conference Ricerche Archeologiche alla Foce del Tevere (Rome - Ostia, December 2018, 18-20th)*. Peeters Publishers. https://doi.org/10.2307/j.ctv2k057j8.

Mastrorillo, L., Mazza, R., Tuccimei, P., Rosa, C., & Matteucci, R., 2016. Groundwater monitoring in the archaeological site of Ostia Antica (Rome, Italy): First results. *Acque Sotterranee - Italian Journal of Groundwater*. https://doi.org/10.7343/as-2016-192.

McLachlan, P., Blanchy, G., & Binley, A., 2021. EMagPy: Open-source standalone software for processing, forward modeling and inversion of electromagnetic induction data. *Computers & Geosciences*, *146*, 104561. https://doi.org/10.1016/j.cageo.2020.104561.

Milli, S., D'Ambrogi, C., Bellotti, P., Calderoni, G., Carboni, M. G., Celant, A., Di Bella, L., Di Rita, F., Frezza, V., Magri, D., Pichezzi, R. M., & Ricci, V., 2013. The transition from wave-dominated estuary to wave-dominated delta: The Late Quaternary stratigraphic architecture of Tiber River deltaic succession (Italy). *Sedimentary Geology*, *284-285*, 159-180. https://doi.org/10.1016/j.sedgeo.2012.12.003. Not consulted.

Mohamed, A. K., Beshr, A. M., Xue, G., & El-Qady, G., 2023. Integration of EM techniques for mapping buried historical harbours: A case study from the archaeological site of Tell el-Rub'a, Egypt. *Journal of Geophysics and Engineering*, *20*(2), 343-360. https://doi.org/10.1093/jge/gxad016.

Park, C. B., Miller, R. D., & Xia, J., 1999. Multichannel analysis of surface waves. *Geophysics*, *64*(3), 800-808. https://doi.org/10.1190/1.1444590.

Pašteka, R., Pánisová, J., Zahorec, P., Papčo, J., Mrlina, J., Fraštia, M., Vargemezis, G., Kušnirák, D., & Zvara, I., 2020. Microgravity method in archaeological prospection: Methodical comments on selected case studies from crypt and tomb detection. *Archaeological Prospection*, *27*(4), 415-431. https://doi.org/10.1002/arp.1787.

Renard, P., & Straubhaar, J., 2024. *geone: Geostatistical Python package* [Python package]. GitHub. https://github.com/randlab/geone.

Salomon, F., Goiran, J.-P., Noirot, B., Pleuger, E., Bukowiecki, E., Mazzini, I., Carbonel, P., Gadhoum, A., Arnaud, P., Keay, S., Zampini, S., Kay, S., Raddi, M., Ghelli, A., Pellegrino, A., Morelli, C., & Germoni, P., 2018. Geoarchaeology of the Roman port-city of Ostia: Fluvio-coastal mobility, urban development and resilience. *Earth-Science Reviews*, *177*, 265-283. https://doi.org/10.1016/j.earscirev.2017.10.003.

Salomon, F., 2020. Les origines d'Ostie : Quelles interactions avec la dynamique d'embouchure ? (Delta du Tibre, Italie). *Archimède. Archéologie et histoire ancienne*, *7*, 129-140. https://doi.org/10.47245/archimede.0007.act.03.

Salomon, F., Vittori, C., Noirot, B., Pleuger, E., Rosa, C., Mazzini, I., Carbonel, P., Djerbi, H., Bellotti, P., & Goiran, J.-P. (2020). Reconstruction of the Tiber Deltaic stratigraphic successions near Ostia using the PADM chart and tracking of the bedload-derived facies (Rome, Italy). *Geomorphology*, *365*, 107227. https://doi.org/10.1016/j.geomorph.2020.107227.

Segre, A. G., 1986. *Considerazioni sul Tevere e sull'Aniene nel Quaternario*. Not consulted.

Turci, M., Uehara, M., & Mathe, P.-E., 2020. Per un'ipotesi di identificazione del Foro di Aureliano e del praetorium di Ostia. Prime osservazioni a partire dalle indagini geofisiche. *Scienze dell'antichità*, *26*(1), 15-40.

Wathelet, M., 2008. *Geopsy: Software for geophysical analysis* [Computer software]. Université de Liège. http://www.geopsy.org.

Wunderlich, T., Fischer, P., Wilken, D., Hadler, H., Erkul, E., Mecking, R., Günther, T., Heinzelmann, M., Vött, A., & Rabbel, W., 2018a. Constraining electric resistivity tomography by direct push electric conductivity logs and vibracores: An exemplary study of the Fiume Morto silted riverbed (Ostia Antica, western Italy). *GEOPHYSICS*, *83*(3), B87-B103. https://doi.org/10.1190/geo2016-0660.1.

Wunderlich, T., Wilken, D., Erkul, E., Rabbel, W., Vött, A., Fischer, P., Hadler, H., & Heinzelmann, M., 2018b. The river harbour of Ostia Antica—Stratigraphy, extent and harbour infrastructure from combined geophysical measurements and drillings. *Quaternary International*, *473*, 55-65. https://doi.org/10.1016/j.quaint.2017.07.017.

Zhou, B., Bouzidi, Y., Ullah, S., & Asim, M., 2020. A full-range gradient survey for 2D electrical resistivity tomography. *Near Surface Geophysics*, *18*(6), 609-626. https://doi.org/10.1002/nsg.12125.

9. Annexes

9.1. Drilling analysis

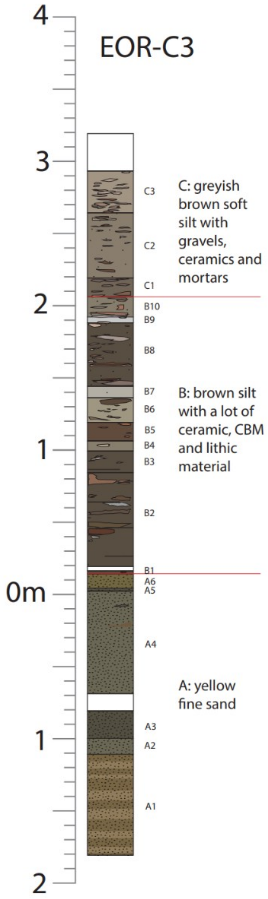

Figure 97: Drillings present on the R1 transect (Delmetz, 2024)

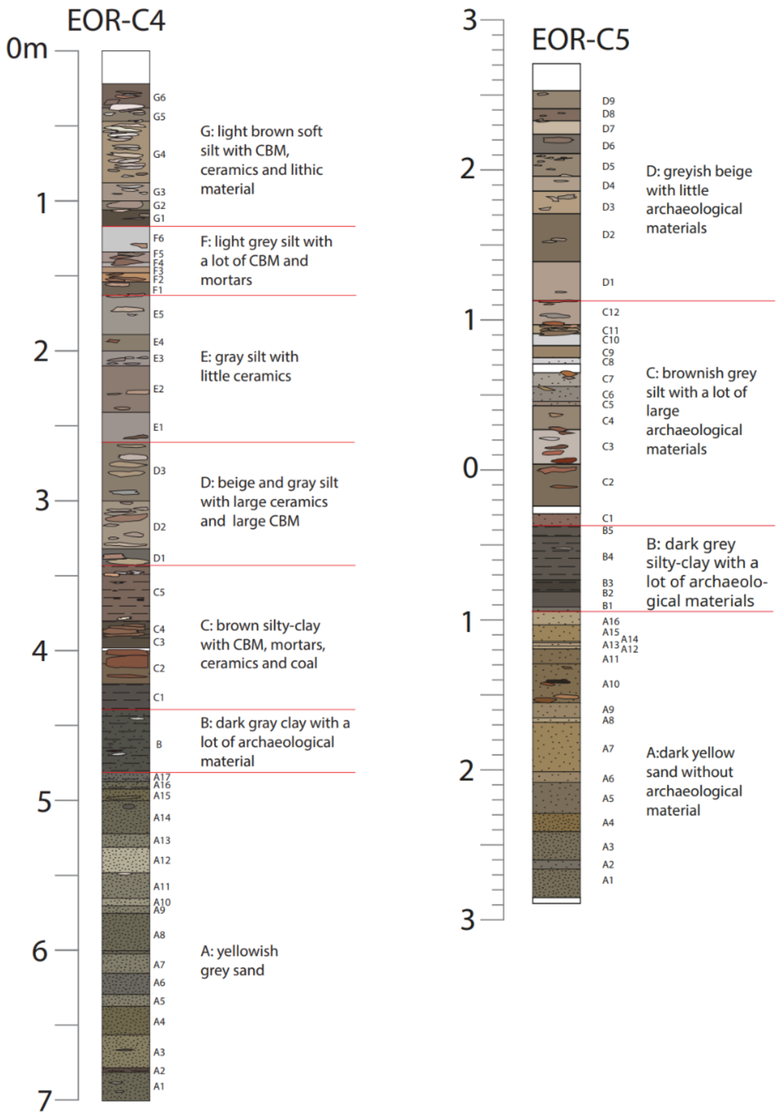

Figure 98: Drillings present on the R4-5 transect (Delmetz, 2024)

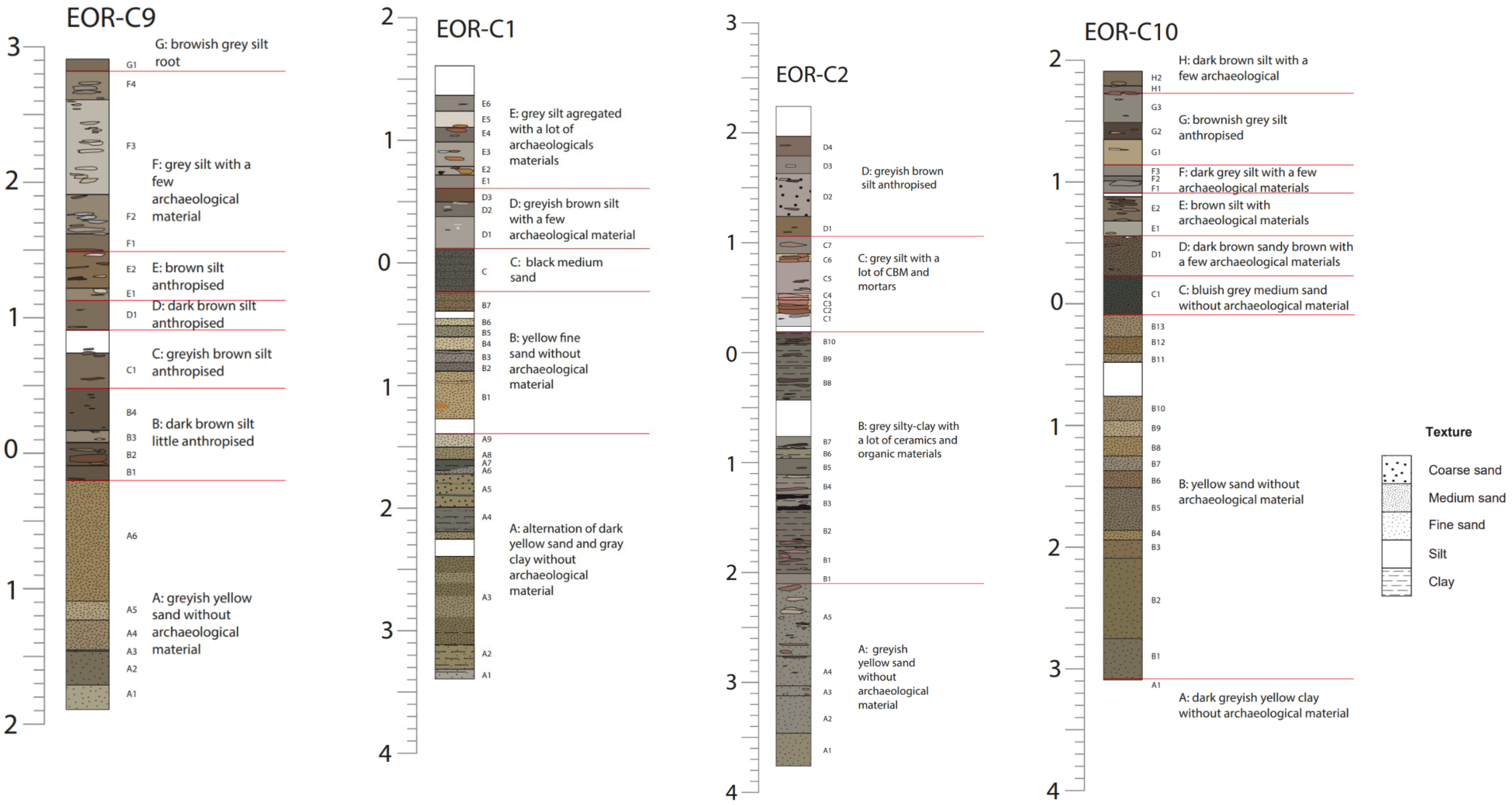

Figure 99: Drillings present on the R8 transect (Delmetz, 2024)

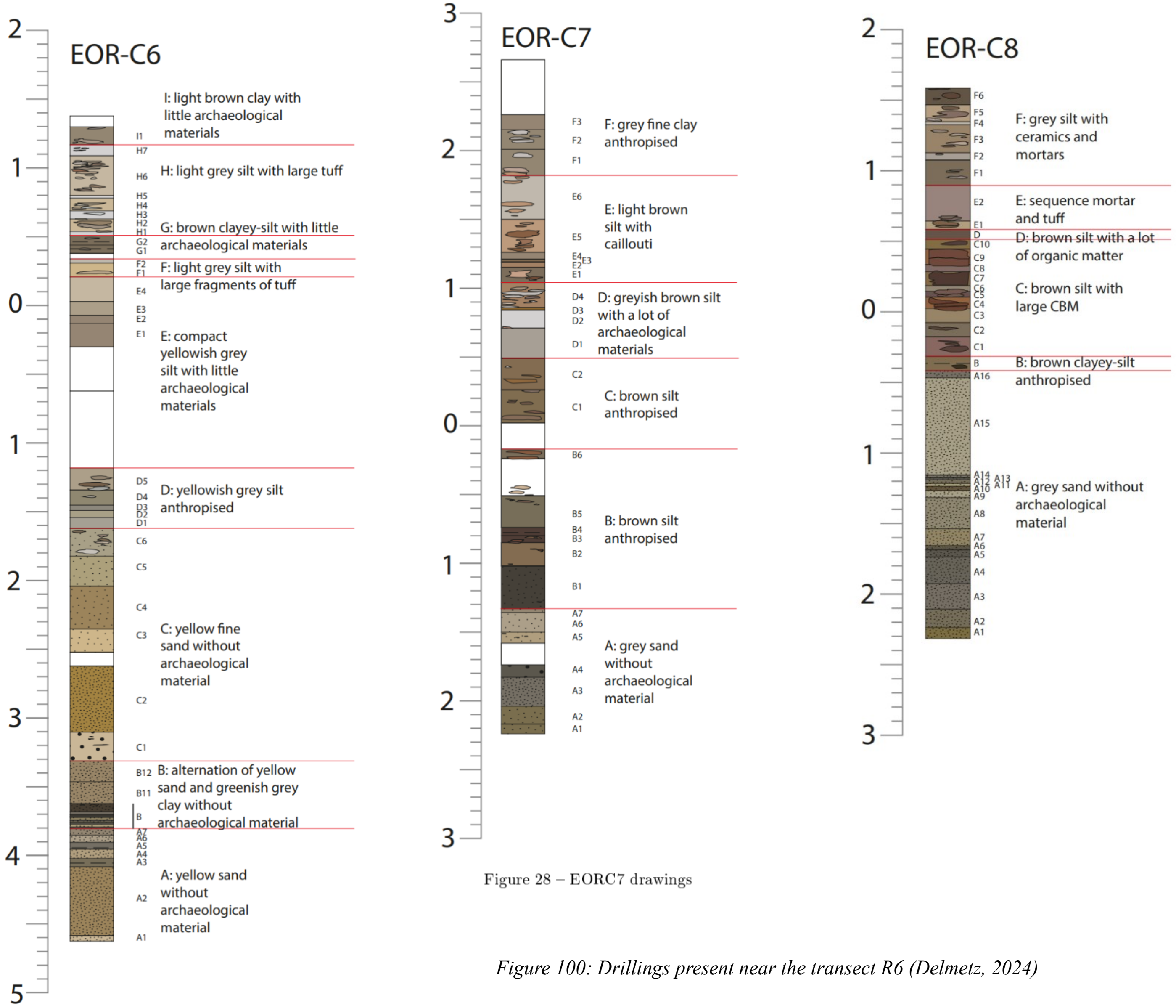

Figure 28 – EORC7 drawings

Figure 100: Drillings present near the transect R6 (Delmetz, 2024)

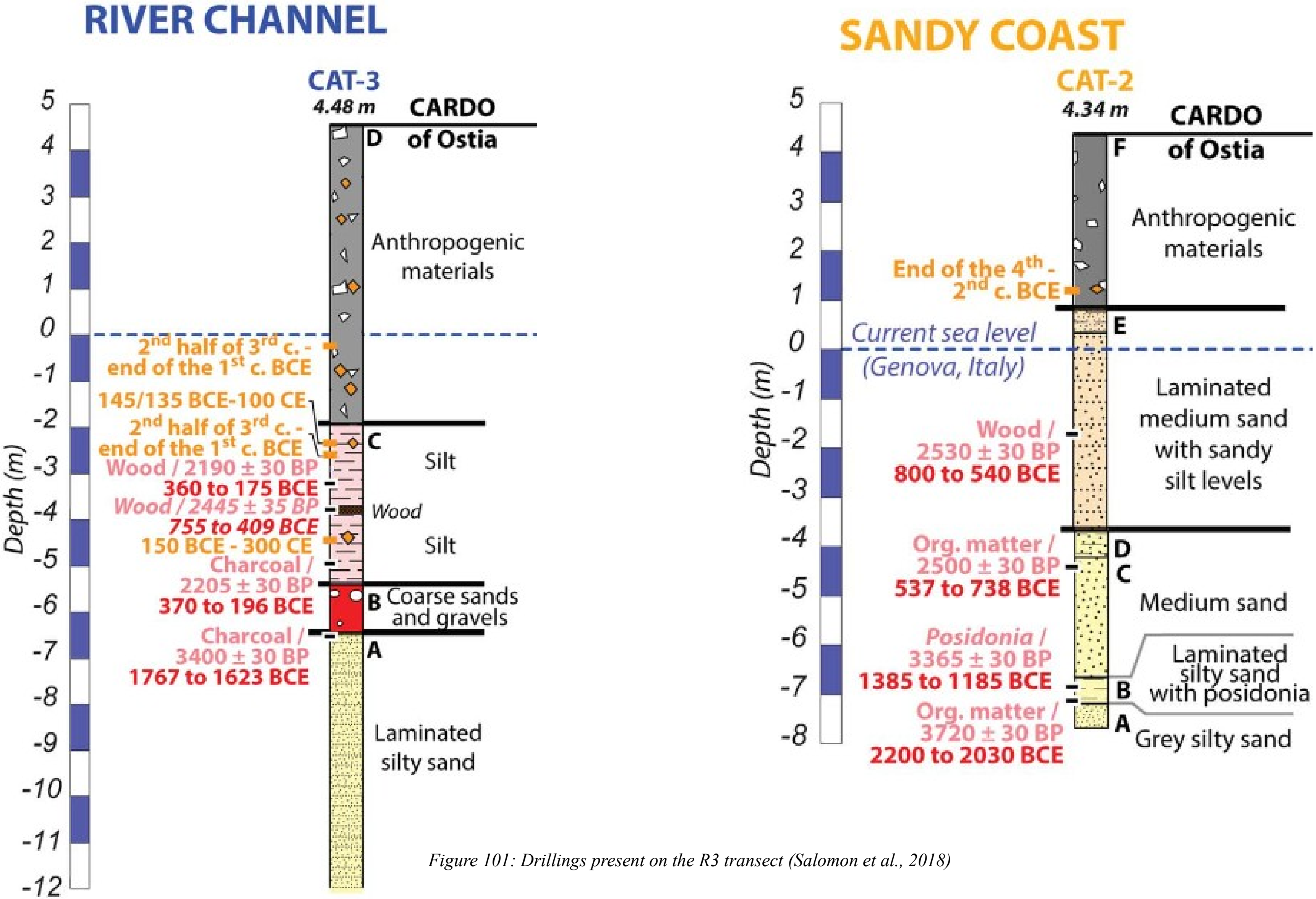

Figure 101: Drillings present on the R3 transect (Salomon et al., 2018)

9.2. Pseudo-sections

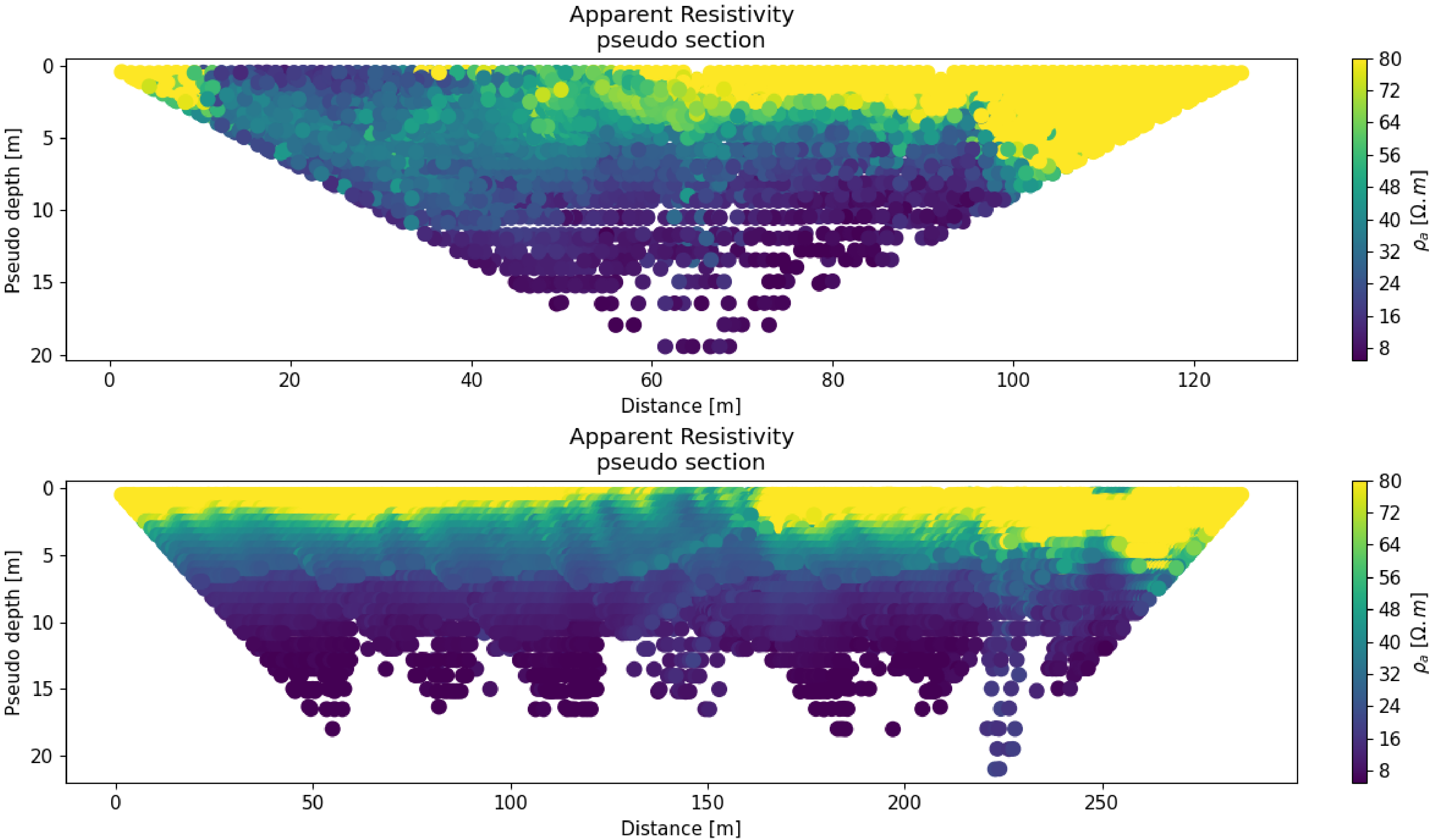

Figure 102: Pseudo-sections realised with ResIPy for (a) profile R7, (b) profile R8

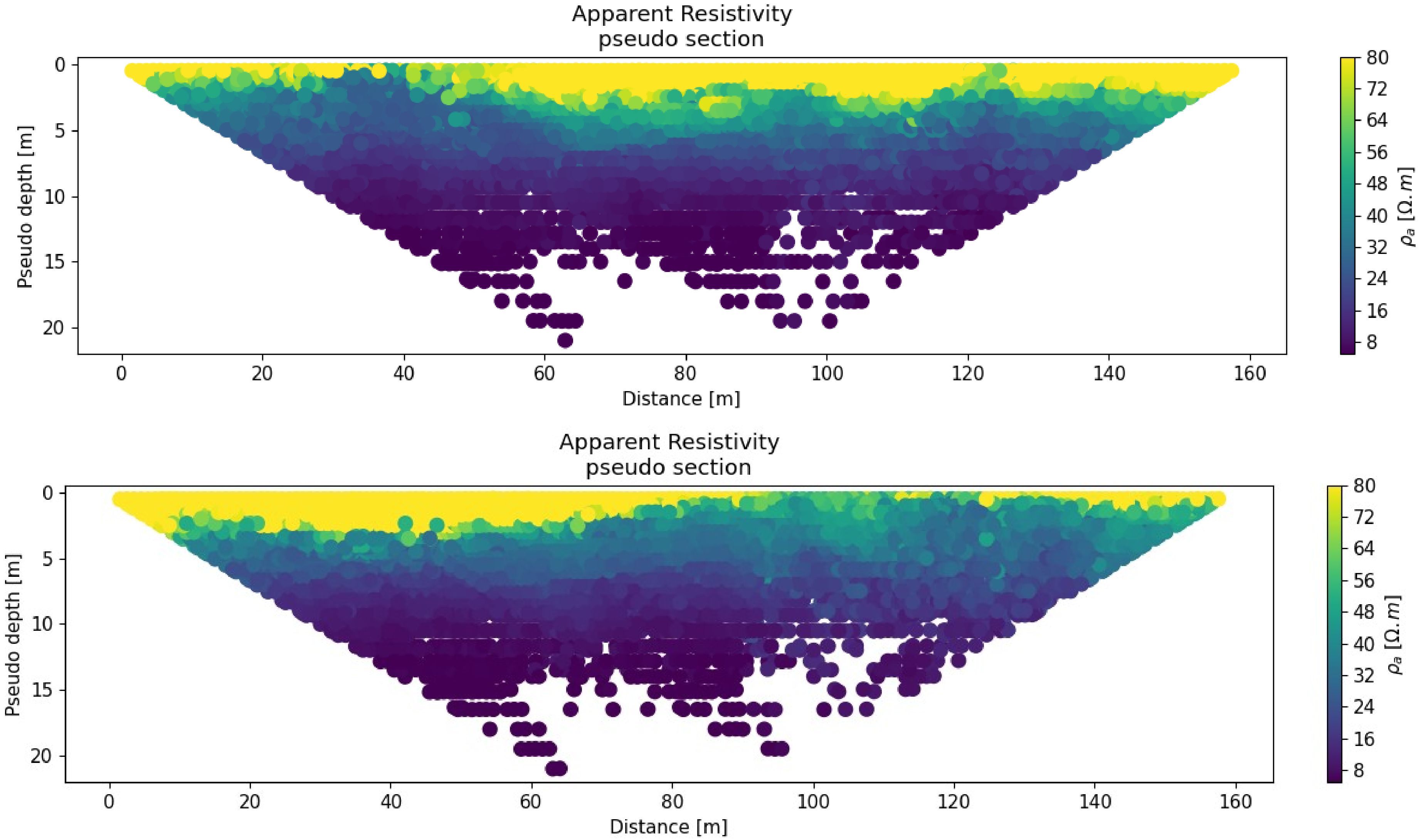

Figure 103: Pseudo-sections realised with ResIPy for (a) profile R10, (b) profile R11

9.3. Results of Classification 1

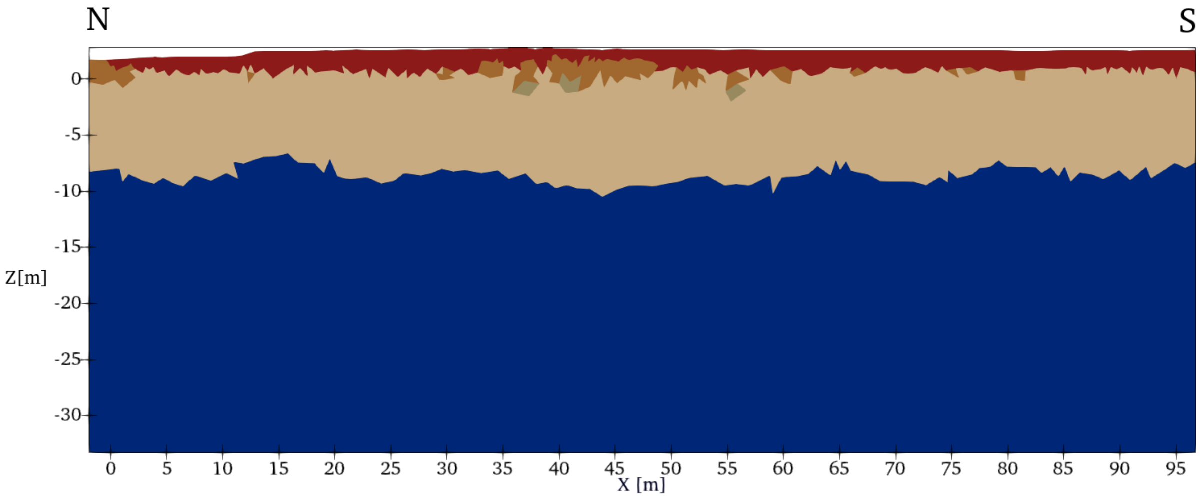

Figure 104: Results of Classification 1 for profile R6

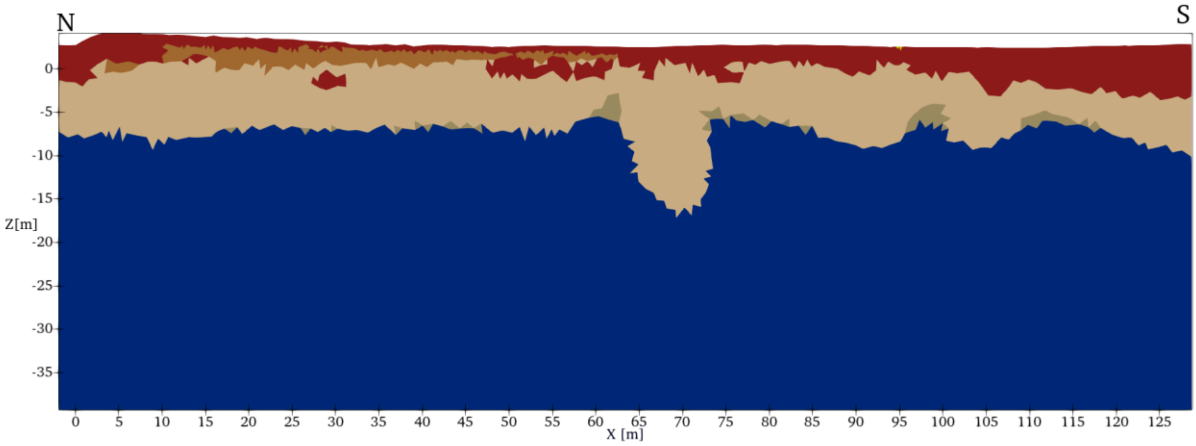

Figure 105: Results of Classification 1 for profile R7

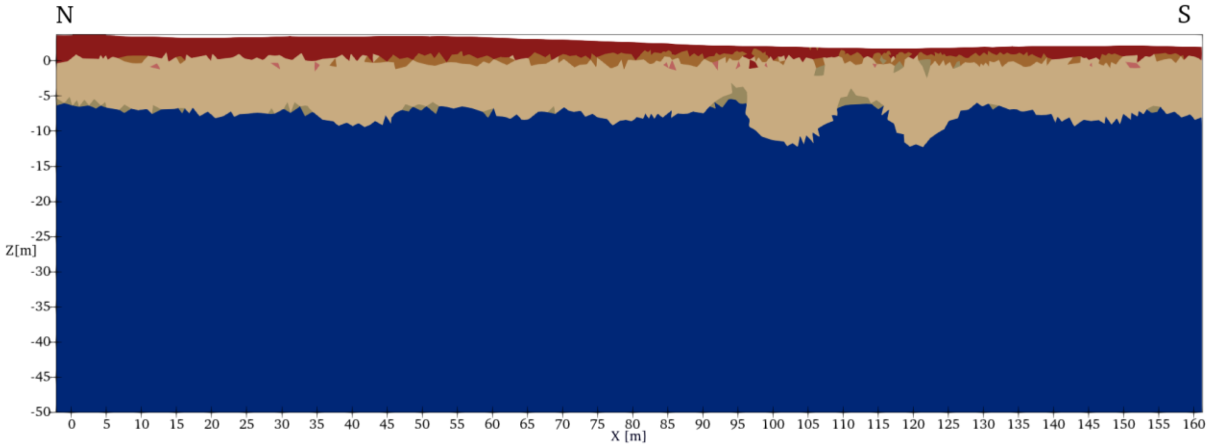

Figure 106: Results of Classification 1 for profile R11

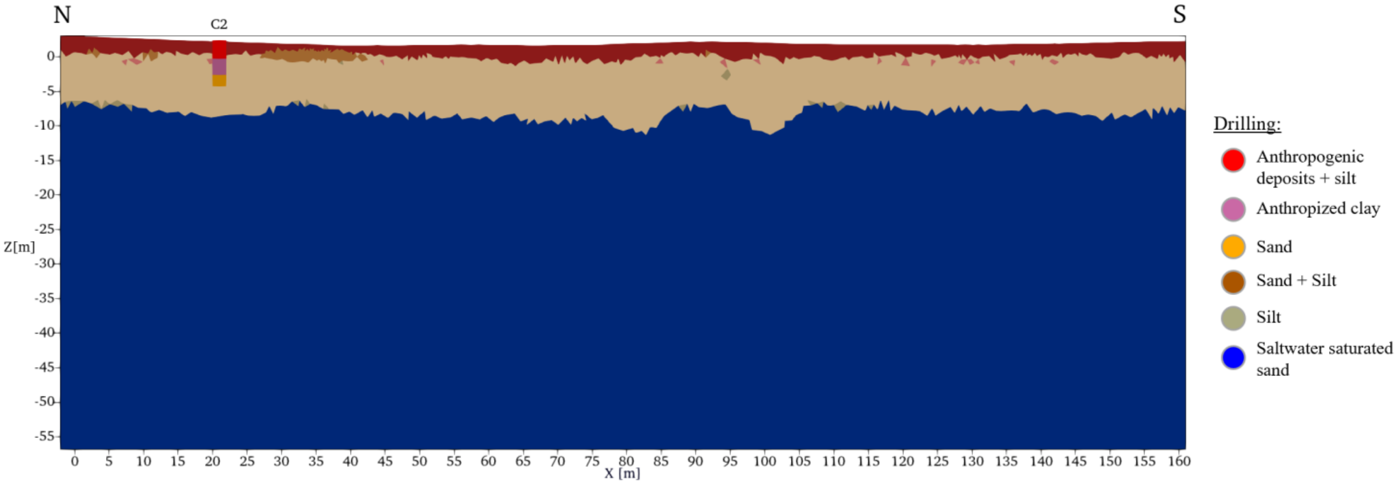

Figure 107: Results of Classification 1 for profile R10

Profile P7 and P8 are also classified.

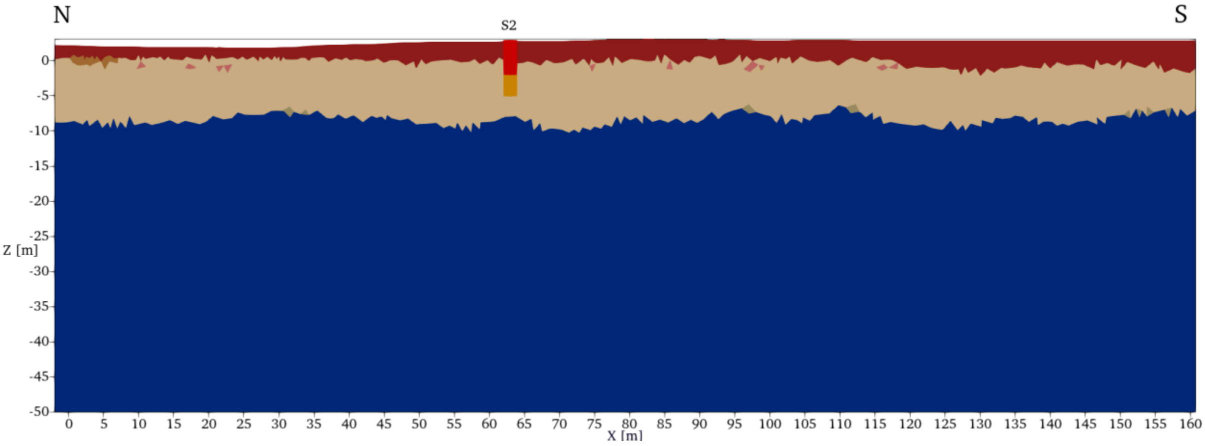

Figure 108: Results of Classification 1 for profile P7

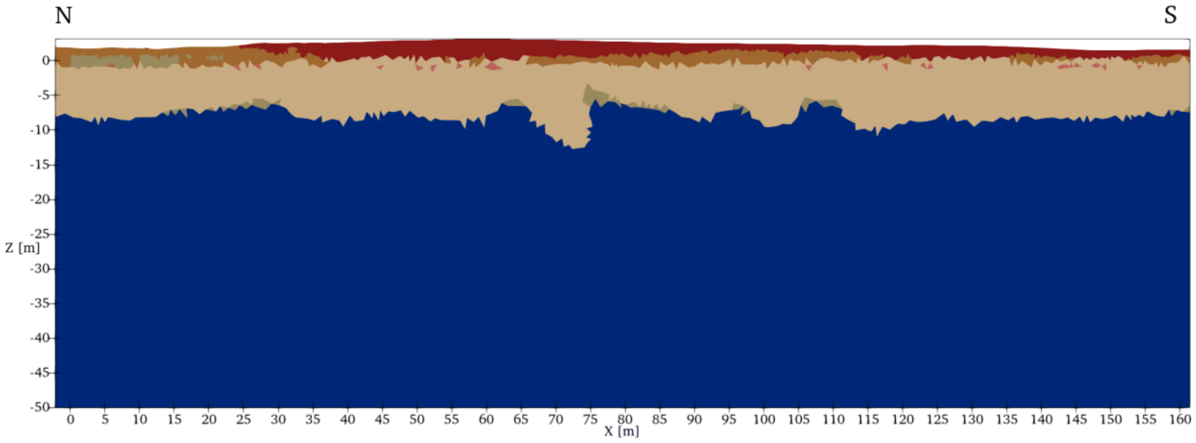

Figure 109: Results of Classification 1 for profile P8